Advances of full-field optical coherence tomography (FFOCT) for clinical applications and developmental biology

Adriano Burcheri-Curatolo

THÈSE

pour l'obtention du grade de

Docteur en Sciences

de l'Université Pierre et Marie Curie – Paris 6

Mention : Optique Biomédicale

présentée par

Adriano CURATOLO

Usage: BURCHERI-CURATOLO

AVANCÉES EN TOMOGRAPHIE OPTIQUE PLEIN CHAMP POUR APPLICATIONS CLINIQUES ET BIOLOGIE DU DÉVELOPPEMENT

École Doctorale : **La Physique de la Particule à la Matière Condensée (ED389)**

Laboratoire d'accueil : **Institut Langevin – ESPCI ParisTech**

Soutenance prévue le 9 Juillet 2012 devant le jury composé de :

Mme BOURG-HECKLY, Geneviève	*Examinateur*
Mme DEUMIÉ, Carole	*Rapporteur*
Mme LAPLACE-BUILHÉ, Corinne	*Examinateur*
M. BOCCARA, Claude	*Directeur de Thèse*
M. FORGET, Benoît	*Examinateur*
M. POULET, Patrick	*Rapporteur*

THÈSE

pour l'obtention du grade de

Docteur en Sciences

de l'Université Pierre et Marie Curie – Paris 6

Mention : Optique Biomédicale

présentée par

Adriano CURATOLO

Usage : BURCHERI-CURATOLO

ADVANCES OF FULL-FIELD OPTICAL COHERENCE TOMOGRAPHY (FFOCT) FOR CLINICAL APPLICATIONS AND DEVELOPMENTAL BIOLOGY

École Doctorale : **La Physique de la Particule à la Matière Condensée (ED389)**

Laboratoire d'accueil : **Institut Langevin – ESPCI ParisTech**

Soutenance prévue le 9 Juillet 2012 devant le jury composé de :

Mme BOURG-HECKLY, Geneviève	*Examinateur*
Mme DEUMIÉ, Carole	*Rapporteur*
Mme LAPLACE-BUILHÉ, Corinne	*Examinateur*
M. BOCCARA, Claude	*Directeur de Thèse*
M. Forget, Benoît	*Examinateur*
M. POULET, Patrick	*Rapporteur*

Acknowledgments

I would like to thank Pr. Claude Boccara, my thesis supervisor, for his patience and relentless energy as a researcher. It has been a great opportunity to work on this project and this thesis has greatly benefited from his continuous guidance and insight into full-field optical coherence tomography. I would also like to thank LLTech's director and founder, Bertrand De Poly, for his generosity and for making available resources during the clinical studies and collaborations of this work.

The contribution of several members of LLTech team must also be appropriately acknowledged. I am thankful to Sylvie Nadolny whose help and collaboration on the equipments made possible the imaging results of this work; to Charles Brossolet who has been instrumental in all the software related issues; and finally Eugénie Dalimier, Fabrice Harms and Franck Martins for their help and technical expertise, but also for their enthusiasm and sense of humour so much appreciated.

From ESPCI ParisTech, I would like to acknowledge the work of several people. In particular, Osnath Assayag, whose active collaboration in the clinical studies was critical; Anne Latrive, a PhD colleague, whose delicious cooking will be remembered; and Florian Poisson, a graduate student, who carried out performance measurements of the instrument.

Clinical work was performed with the precious help of two clinicians. Dr. Brigitte Sigal-Zafrani from Institut Curie and Dr. Martine Antoine from Tenon hospital in Paris who made possible the collection of specimens in the pathology laboratory and the diagnostic evaluation of both tomographic images and corresponding histology. Likewise, Dr. Vincent Servois, radiologist was instrumental in facilitating the needle biopsy study within the imaging unit at Institut Curie. In addition, I acknowledge the work of Eolia Flandre and Dr.Jeanine Quillard for histology slides scanning.

From the ESPCI Laboratory of Neurobiology, I wish to acknowledge the support of Serge Birman and the continuous efforts of Thomas Riemensperger for our collaboration on the challenging experiment with living fruit flies.

I was fortunate to work within the Institut Langevin, which has provided an enriching environment with outstanding scientists. I would like to thank Gianmarco Pinton for his help with phantoms and programming, Mathieu Pernot for his contacts in pathology laboratories; Corinne, Olivier, Rémy and many others for thoughtful discussions; and Julie Delahaye for the opportunity of teaching laboratory classes at *Ecole Centrale, Paris*.

Amongst the many others who contributed to the success of this thesis, I wish to particularly thank my parents for providing the grounds and support for my education.

Abstract

Optical coherence tomography (OCT) is now an established technique for visualizing the internal morphology of the eye. In the last decade, the aim has been to achieve similar results in highly scattering tissues. One limitation of previous studies with OCT has been the low resolution compared to the gold standard of histology. Full-field optical coherence tomography (FFOCT), a variant of OCT also based on low-coherence interferometry, generates micron-scale images over a large field of view by simply using a camera as an array detector and a tungsten-halogen light source.

In this work, a compact FFOCT system has been tested under clinical conditions for imaging breast lesions up to 1 cm² as well as core-needle biopsies. A set of diagnostic criteria have been identified to differentiate benign from malignant tissues with encouraging preliminary results, nonetheless endogenous contrast enhancements are necessary. Attenuation maps were shown to be limited by the high heterogeneity of tissues within only a few micron depth. An alternative approach, based on the elastic properties of tissues, has been demonstrated to be feasible and could hold greater prospects. In addition, the penetration depth of the instrument has been improved by a minimum of a factor two with an InGaAs camera system operating in the infrared region and using silicone oil as immersion medium.

Finally, three-dimensional imaging in-vivo was demonstrated during the 4 days of metamorphosis of a *Drosophila melanogaster*. The FFOCT system was able to record each organ growth at a depth of 80 µm with an isotropic micron resolution. This marks progress toward potential applications in developmental biology.

Keywords: *FFOCT, Tomography, Breast Cancer, Attenuation, Elasticity, Developmental Biology*.

Résumé

La tomographie optique cohérente (OCT) est maintenant une technique établie permettant de visualiser la morphologie interne de l'œil. Au cours de la dernière décennie, l'objectif a été d'atteindre des résultats similaires dans des tissus fortement diffusants. Une limite des études précédentes en OCT s'avère être la faible résolution en comparaison des techniques d'histologie traditionnelle. La tomographie optique cohérente plein-champ (FFOCT), une variante de l'OCT également basée sur l'interférométrie en lumière faiblement cohérente, produit des images à l'échelle du micron sur un large champ de vue en utilisant une simple camera et une lampe à incandescence halogène pour l'illumination.

Dans ce manuscrit, un système FFOCT compact a été testé en conditions cliniques afin d'examiner de larges lésions mammaires, jusqu'à 1 cm², ainsi que des microbiopsies. Un ensemble de critères diagnostics ont pu être identifiés pour différencier tissus bénins de malins, avec des premiers résultats encourageants; toutefois des méthodes d'améliorations du contraste endogène s'avèrent nécessaires. Une méthodologie basée sur les coefficients d'atténuation du flux lumineux s'est montré limitée du fait de la forte hétérogénéité des tissus sur une profondeur de quelques microns. La faisabilité d'une approche alternative, exploitant les propriétés élastiques des lésions cancéreuses, a été réalisée et offre de meilleures perspectives. En outre, la profondeur de pénétration de la technique a pu être améliorée au moyen d'un système utilisant une caméra InGaAs opérant dans l'infrarouge et d'une huile de silicone en tant que liquide d'immersion.

Finalement, l'imagerie tridimensionnelle in-vivo a été démontrée pendant les 4 jours de la métamorphose de *Drosophila melanogaster*. Le dispositif d'OCT plein champ a ainsi pu suivre la croissance de chaque organe à une profondeur de près de 80 µm avec une résolution isotrope à l'échelle du micron, ouvrant ainsi des perspectives d'applications en biologie du développement.

Mots-clés : *FFOCT, Tomographie, Cancer du Sein, Atténuation, Élasticité, Biologie du Développement.*

Table of Contents

Introduction

One of the core purpose of the art and science of medicine can be formulated in simple terms: "*first, do not harm*". A whole new branch of medicine has been set up around the central idea of avoiding invasive surgical procedures. At first, with the broader use of X-rays, medical imaging has long been focused on obtaining a visual result and less concerned with its hazardous consequences over the long term[1]. Gradually, with the development of novel techniques such as magnetic resonance imaging (MRI) and miniaturized components, less invasive approaches were made possible.

In that context, light-based imaging appears as the natural continuity of this process; towards limited side effects and higher resolution. In the last three decades, it has led to an increasing number of optical methods in clinical medicine including, for example, fluorescence techniques, non-linear optical imaging (e.g. multiphoton microscopy,...) or ultra-high resolution techniques (4pi or structured illumination microscopy,...). Within the setting of this larger revolution in optical imaging, optical coherence tomography (OCT) has emerged since the early 90's as a versatile but powerful method. Several variants have been proposed, all based on the core principle of interferometric microscopy. FFOCT for Full-field Optical Coherence Tomography is one of these variants, with the difference of producing "en-face" images without the need for scanning a beam over the field of view by using a camera as an array detector and a simple tungsten-halogen light source.

The underlying idea is to emulate the time-tested gold standard methods of histopathology and to provide a valid diagnostic complement. Compared to other high-resolution microscopy techniques, FFOCT's main benefit is to be able to image subsurface biological specimen over a large area of up to 1 cm^2 with an isotropic micron-scale resolution; and without the need for staining or external contrast agents. The instrument initially conceived and developed at the ESPCI[2] laboratory has been further expanded by the laboratory spin-up LLTech in the past 3 years. This work has been performed in close collaboration with the engineering team of LLTech, researchers from Institut Langevin, ESPCI and clinicians.

[1] *It is more a demographic issue than an individual one – as far as adult patients are concerned [1].*
[2] *ESPCI stands for Ecole Supérieure de Physique et Chimie Industrielles de la ville de Paris.*

Statement of work

The aims of this thesis were to fully explore the clinical and research applications of the technique and to demonstrate the validity or non-validity of its technological improvements under the constraint of a realistic implementation in clinic and to propose innovative approaches towards that direction.

The written thesis in composed of six individual chapters. Chapter 1 introduces the biomedical context of this work in relation to other imaging techniques, and in particular the parent technique of conventional OCT. The second part of the chapter frames the basic theoretical tools to understand the interaction of light with biological tissues. Chapter 2 presents the compact setup used in this work with a focus on the new fine adjustments implemented to obtain the most resolved and contrasted images for a potential use in clinical routine.

However, a medical image is only as good as its ability to be interpreted by a clinician. An important focus of this thesis has been to initiate the long process of novel images interpretation. In particular, breast lesions for the medical aspects of this work (Chapter 3), and in biology, the in-vivo organogenesis of Drosophila melanogaster (Chapter 5).

Novel contrast techniques have been examined in an attempt to quantitatively assess these novel images. Chapter 4 investigates a method based on attenuation maps and its major limitation; the second part demonstrates the feasibility of a new full-field optical elastography method and identifies several pitfalls for further investigation.

Finally, the last chapter compares and demonstrates the performance of a novel FFOCT instrument in the near-infrared region aimed at increasing the penetration depth achieved with a particular interest on the nature of photons in highly scattering biological tissues.

The general conclusion provides a brief summary of results and an overall discussion on the methodology as well as perspectives for future studies.

Chapter I. Principles and context of OCT imaging in biological tissues.

This chapter briefly presents the basic principles of Optical Coherence Tomography (OCT) and compares the two major OCT techniques: Time-domain OCT (TD-OCT) and Fourier-Domain OCT (FD-OCT). A review of the current literature and perspectives in OCT are also discussed. In a second section, the theoretical tools used to analyse the interaction of light with biological tissues is detailed.

I.1 Conventional OCT and biomedical imaging context

I.1.1 OCT versus other imaging modalities

There are several ways to differentiate optical imaging techniques. One is based on the source of contrast as the determining criteria. OCT and FFOCT or Full-field Optical Coherence Tomography can be qualified as an endogenous anatomical imaging method in contrast to exogenous approaches. By exogenous, one implies a method that requires the addition of molecular agents to characterize a particular tissue or a cellular mechanism (e.g. fluorescence microscopy or immunohistology techniques). In contrast, the endogenous approach solely relies on the optical properties of the tissue under investigation, such as differences in refractive indexes or scattering variations and, to a lower extent, differences in absorption.

Other non-invasive endogenous anatomical imaging techniques rely on radically different principles, such as magnetic resonance imaging (MRI) or computed tomography (CT). Their extensive use in clinical settings is essentially due to the penetration depth achieved when the need for a micron-scale resolution is not deemed necessary. In comparison, microscopic techniques

(FFOCT included) can achieve resolutions 10 to 100 times greater than these methods. Figure I.1 presents an overview of the most common biomedical imaging techniques with corresponding resolution and penetration depth.

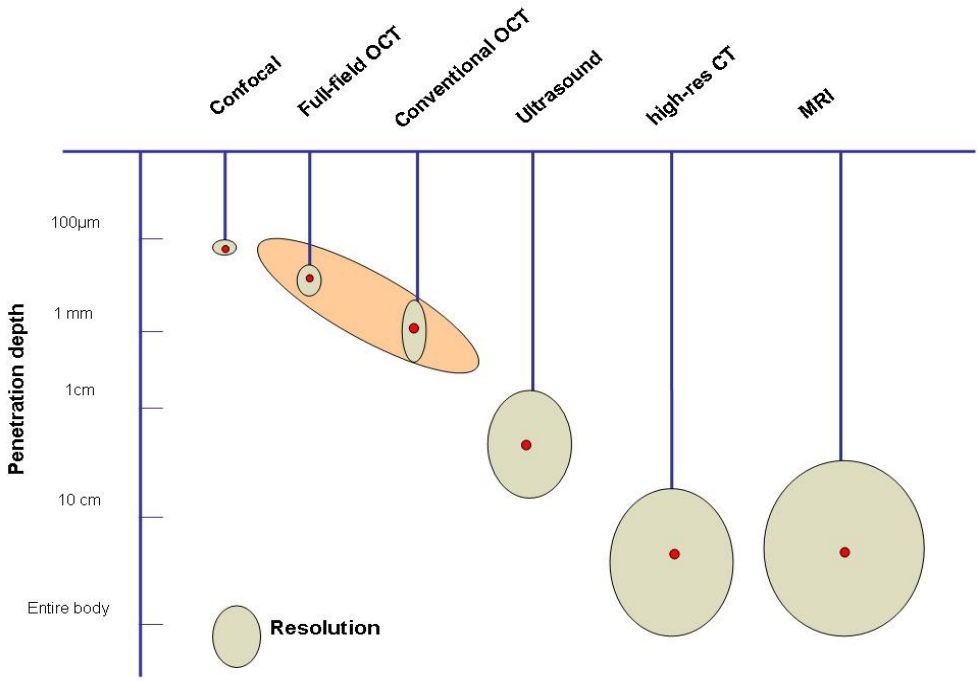

Figure I.1: Schematic representation of the resolution and penetration depth in common imaging modalities.

As shown, optical coherence tomography (OCT and FFOCT) fills a gap in medical imaging techniques. Ultrasound can achieve a penetration depth of several centimetres with the restriction of low resolution (high frequency ultrasound still limited to a 50 µm resolution); and on the other end confocal microscopy with high resolution but shallow imaging depth (~100 µm). OCT and confocal microscopy are however different in many respects as detailed further in this chapter.

Confocal fluorescence microscopy is now a well-established method in research and is extensively used for ex-vivo cellular imaging, living cells, and even 3-D study of cell dynamics [3–6]. Its use in clinical settings has nonetheless been limited for several reasons. The need for intravenous and topically applied stains with potential toxicity have thus not yet been widely accepted. Other limitations include photo-bleaching of fluorescent probes and limited penetration depth. Image contrast is significantly reduced after 100 µm in depth. Since low numerical aperture objectives are commonly used, the limited field of view makes difficult to image large clinical samples (< 1 cm²). Photodamage remains a critical issue in most applications when fluorescent staining is required.

Alternative microscopic techniques address to some extent those limitations. Multiphoton microscopy has been shown to perform imaging on unstained tissues. Although to date most multiphoton microscopy has used with conventional fluorescent proteins or other fluorophores, a

few studies have successfully tested intrinsic molecule contrast. For example NAD(P)H and flavins with two-photon excitation [7–9], or second-harmonic generation (SGH) of retina pigment epithelial cells (mostly collagen) or muscle fibres [10–12].

Reflectance confocal microscopy is another technique that can be performed without the need for molecular staining agents. It uses the endogenous contrast provided by tissue heterogeneity. This technique has been developed by Dr. Rajadhyaksha's group at Memorial Sloan-Kettering, NYC, with a particular focus on skin lesions. They performed nuclear and cellular morphology images in large areas of surgically excised tissues [13], [14]. Confocal reflectance microscopy has also been applied to ex-vivo breast lesions and small-animal models [15], [16]. Although contrast enhancers such as acetic acid or aluminium chloride ($AlCl_3$) are routinely used, those results are promising to establish correlation tests with gold standard histology. This technique allows the imaging of large field of views with the implementation of rapid mosaicing or stitching of individual tiles. This approach can thus be performed in-vivo but remains limited to more accessible body areas (e.g. forearms or the abdomen).

I.1.2 Principles of traditional OCT

Overview

Optical Coherence Tomography can be compared to an optical analogue of B-mode ultrasound[3]. As for sound waves, light is echoed back with a time delay depending on the tissue structure being probed [17]. For ultrasound, the velocity of sound is well within the limits of electronic detectors, for light however, it requires a temporal resolution of the order of femtoseconds. Presently, no detector is able to directly measure such ultra-fast oscillations. In OCT, the echo delay is measured via an interferometric technique whereby the slight difference between the light coming from the specimen and light back-reflected from a reference mirror generates an interference at each pixel on the detector.

OCT principle is thus based on low-coherence interferometry and its most common configuration is a Michelson interferometer [18–20]. Typically, the incident light beam is split into two identical beams by a reference mirror. One beam is directed to the tissue sample and the other focused onto a reference arm. Each of these beams will travel an “approximately” similar distance within the coherence length before recombining at the beam splitter.

Therefore, interferences only occur when the distance travelled in both arms is lower than the coherence length of the light source. The aim is to use sources with spectrum as large as possible in order to obtain the shortest coherence length. Polychromatic light sources are particularly well suited and have a sectioning ability of a few microns. Typical broadband light sources used in OCT

[3] *For brightness-mode and commonly used for prenatal diagnosis.*

are superluminescent diodes, superbright LEDs, or a simple white light source. Alternatively, laser with extremely short pulses can also achieve a broad bandwidth (e.g. femtosecond lasers). A particularity and advantage of OCT is the decoupling of axial and lateral resolution. The z-axis resolution is directly correlated to the coherence length of the light source and along the x-,y- axis it is imposed by the optics. In this work, any reference to traditional or conventional OCT imaging refers to the following imaging techniques.

Time-domain OCT

This is the method used in this work whereby the mechanism of OCT interferometry relies upon the displacement of the reference arm. This mechanical translation fulfils two purposes: to probe the sample in depth and to generate a Doppler shift. To obtain a 2-D or 3-D image (sum of A-scans), the sample is still raster-scanned laterally (x-,y- axis) to display series of cross sections over time as shown on figure I.2. This approach is now commonly referred to time domain OCT in the literature [19], [21–24].

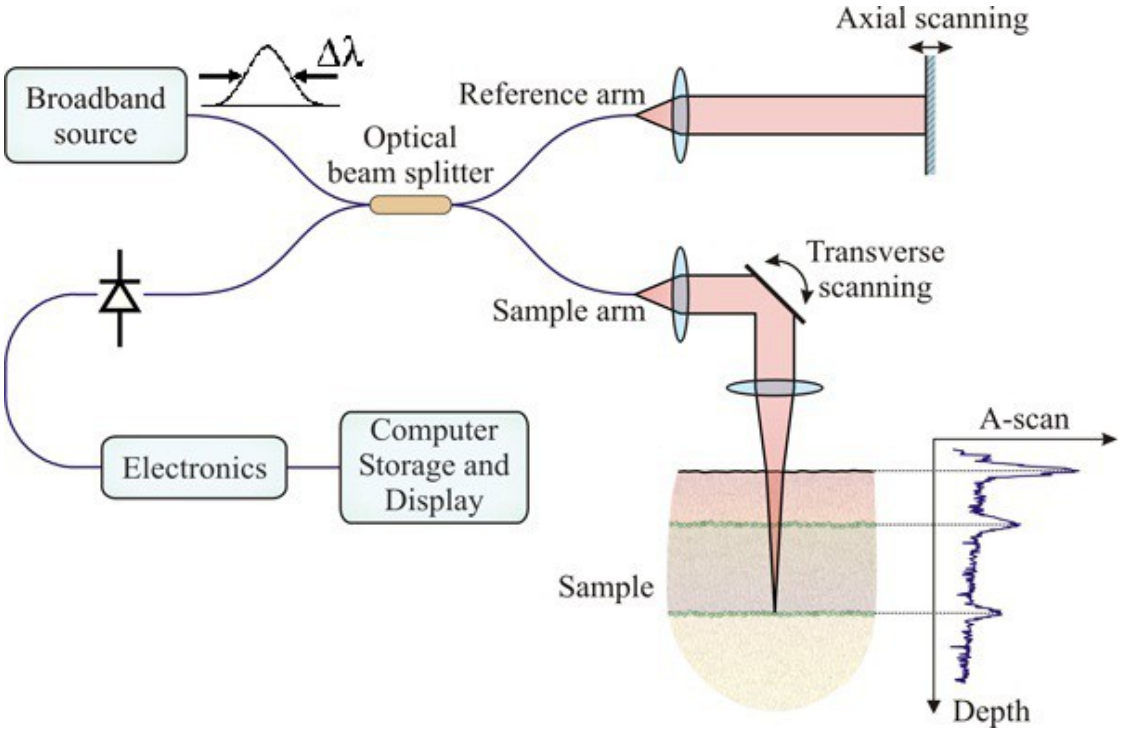

Figure I.2: Schematic of conventional OCT – Time-Domain acquisition mode. A-scan or Axial-scan obtained is directly related to the tissue internal optical variations. Adapted from [82]

This method of acquisition was first applied to retinal imaging by a group at MIT led by Pr. Fujimoto and published in the landmark paper of OCT in 1991[25]. However, the first biological application of time-domain low-coherence interferometry was demonstrated by Fercher et al. three years earlier in 1988 in a publication entitled "Eye-length measurement by interferometry with

partially coherent light". Time-domain OCT has initially known a fast commercial development in ophthalmology before being replaced by a Fourier-domain approach.

Fourier or Frequency-domain OCT

It was then shown that solely extracting the individual frequency components could be sufficient. The initial image could be directly reconstructed by Fourier transform from the spectrum of the interference signal without any mechanical displacement. For a fixed reference arm, a specific frequency is generated in the interference spectrum. Put simply, the single interference signal is analysed by wavelength and results in a spectral interferogram as shown in the diagram of figure I.3.

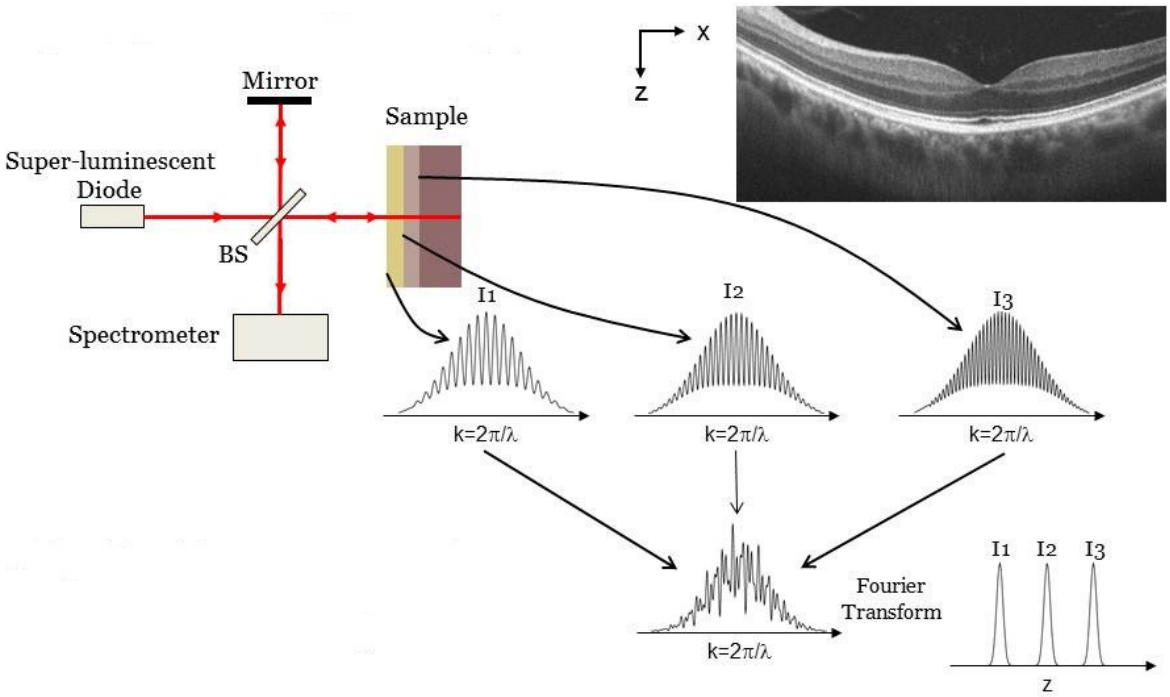

Figure I.3: Schematic of Fourier or Frequency Domain OCT image acquisition (FDOCT). BS: beam splitter. Specimen: human retina. Adapted from [81].

From the resulting frequency map, the position of each extracted intensity maxima informs about the depth of the different back-scattering structures and the amplitude about their respective coefficient of reflection.

Recent developments in Frequency or Fourier Domain OCT have demonstrated novel variants with spectrometer-based detections or wavelength-swept laser sources [26–29]. For the latter, a range of different wavelengths are emitted over time and a frequency difference will depend on the position of the structures and thus producing distinct modulation periods. While this process achieves gain in signal-to-noise ratio, nonlinearities in the wavelength and aliasing artefacts are still present as in Time-Domain OCT.

Comparative advantages of OCT systems

The major advantage of the frequency approach is the gain in time (or signal-to-noise ratio for a fixed time) since the acquisition of each layer is made simultaneously and no mechanical displacement is required (i.e. reference arm and mirror are fixed). The acquisition time gain is significant and of the order of 20–30 times faster than Time-Domain OCT (e.g 10,000 vs >200,000 depth scans/sec). In addition, FDOCT has also demonstrated larger sensitivity advantage of the order of 20–30 dB over TDOCT for a similar acquisition time [30], [31]

For those reasons, Fourier-Domain OCT has become the commercial method of choice for clinical applications. For example, Zeiss® Cirrus OCT for ophtalmology, Volcano® for cardiology or Michelsons Diagnostics® in dermatology. Nonetheless, time-domain commercial equipments claim some advantages in contrast to noise ratio in comparison to Fourier-domain and FDA-approved systems are now been used on patients (e.g. Lightlab Imaging/ St Jude Medical®).

I.1.3 Performances of conventional OCT

In contrast to other optical techniques (e.g. confocal microscopy), the axial resolution achieved is independent of the numerical aperture (NA). Resolution in depth is directly determined by the source coherence length which determines the full-width half maximum of the interferogram (i.e. signal envelope). Standard axial resolution achieved are now around 7-10 µm, and by using novel generation femtosecond lasers, ultra-high axial resolutions of 2-3 µm have been demonstrated [32], [33].

Penetration depth is, with axial resolution decorrelation, a major difference and advantage of OCT imaging in comparison to traditional microscopic or confocal techniques. Principal wavelength ranges used are centred around 800 nm and 1300 nm (*see chapter on the near-infrared setup and next section on light-tissue interaction for more details*). Typical penetration depth at 1300 nm wavelength with small numerical aperture is around 1–2 mm before loss of useful single backscattered signal. In practice, the valuable penetration depth is rather 0.5–1 mm due to a rapid increase of incoherent light collected (i.e. multi-scattered photons overshooting ballistic ones).

Transverse resolution, as with conventional microscopy, is mainly dictated by the objective numerical aperture. For deep cross-sectional imaging, a large depth of field is required and thus low numerical aperture objectives are used. This highly limits the transverse or lateral resolution to the order of 10 µm. Unless a dynamic focusing is applied, but slows down the acquisition process, the depth of field must be approximately equal to the axial depth scan (e.g. 15 µm lateral resolution corresponds to about 0.8 mm depth of field).

I.1.4 Selected applications

Optical coherence tomography is now an established medical imaging technique. Its initial and most extensive use is in ophthalmology, in particular to image the back of the eye or the retina. It allows for example, the assessment of axonal integrity in multiple sclerosis or to measure changes in retinal nerve fibre layer as indication of treatment outcomes [34–38].

Another major application is in-vivo endoscopic OCT, in particular for coronary arteries defects or lesions of the upper-aerodigestive tract. For vascular diseases, OCT has been investigated to detect vulnerable lipid-rich plaques since OCT can achieve high penetration depth underneath the epithelial layer [39–43]. Likewise, suspicious lesions of the oral cavity could be potentially detected early or follow-up progress more precisely monitored in conditions such as Barrett's oesophagus [44–50].

Cancer detection and tumour margin assessment are also a major focus of research, and techniques are now entering the stage of sensitivity and specificity measurements in comparison to the gold standard of histology. Organs mostly tested ex-vivo include skin, breast and breast lymph nodes [51–57].

The addition of new contrasts, endogenous or exogenous (e.g. nanoparticles, optical elastography), multi-modality combinations (e.g. OCT and multiphoton microscopy or fluorescence) and functional imaging are progressively appearing as the most active areas of research in OCT [58–63]. A variety of non-medical applications can be found in the literature. However, the most predominant fields of study are in art restoration and archaeology [64–72].

I.1.5 Conclusion

This brief overview of OCT, the parent technique of FFOCT highlights its potential forfilling in a gap between ultrasound and confocal microscopy in terms of resolution and penetration depth. The principles of the two main approaches have been described and it is important to note that FFOCT is based on a time-domain approach.

I.2 Optical properties of biological tissues

Improving light's penetration through turbid media with minimum loss of resolution is an essential goal in biomedical optics. Several limiting factors due to the nature of a biological tissue and its interaction with light are presented along with notations used.

I.2.1 Light – tissue interaction.

Tissue heterogeneity constitutes a major challenge in the tomographic imaging of a biological tissue. This heterogeneity also provides a characteristic information that can be optically extracted. Such properties are as much related to the specific absorption and scattering at a macroscopic level (tissue refractive index inhomogeneities) than the individual cell's constituents at a microscopic level. In addition, visible and near-infrared wavelengths regions provide the advantage of being non-ionizing and potentially extremely fast.

However, those properties and heterogeneities are also major limitations for achieving sufficiently resolved images at a given optical plane underneath the surface. The difficulty of several microscopic techniques is therefore to extract the signal from the optically sliced plane and filtering out unwanted information from surrounding layers. In this process, photons undergo several interactions that alter and attenuate the signal detection from a particular plane. When an incident light wave interacts with a single particle, part of its energy is absorbed and another part scattered.

Both phenomenon follow a similar mechanism, in that sense that energy is removed from a beam of light traversing a medium: here the beam is attenuated by the biological tissue. As commonly used, the attenuation μ_t is defined as the sum of scattering and absorption ($\mu_t = \mu_s + \mu_a$). Nonetheless, for biological tissues, scattering has been extensively shown to constitute the major limiting factor [73], [74].

Absorption, therapeutic window and wavelength dependence.

This work explores two different wavelength regions with significant differences in terms of light absorption and consequently penetration depth. The first FFOCT system is centred around 715 nm in the visible wavelength portion of the spectrum and a full width half maximum (FWHM) of approximately 125 nm. The second setup operates in the near infra-red with a central peak around 1225 nm and FWHM of 600 nm.

The absorption phenomenon is due to the fact that part of the incident energy emitted by a source of illumination is not scattered but transferred into an other form of energy such as thermal

energy. An absorption coefficient, μ_a can be defined as the probability of incident light absorbed by tissue per unit length [cm^{-1} or mm^{-1}]. This macroscopic coefficient is due to the vibration and change of electron states in response to light. When a collimated plane wave propagates in a homogeneous medium with only absorption without any scattering, with a length, L, the intensity variation as function of the pathlength is given by the Beer-Lambert's law (valid in a homogeneous medium):

$$I_t = I_0 e^{-\mu_a . L} \quad (1)$$

with I_0 the incident light's intensity and I the signal intensity collected at the detector and μ_a the absorption factor.

In biological tissues, three main molecules are responsible for the absorption of light: haemoglobin, water and melanin. Their respective absorption spectra define a window of low absorption of light and it is known as the *optical therapeutic window*. As shown on figure I.4, this window extends from 0.6 µm to 1.3 µm. Below 0.6 µm, blood is the principal absorber and water from 1.3 µm onwards towards higher wavelengths.

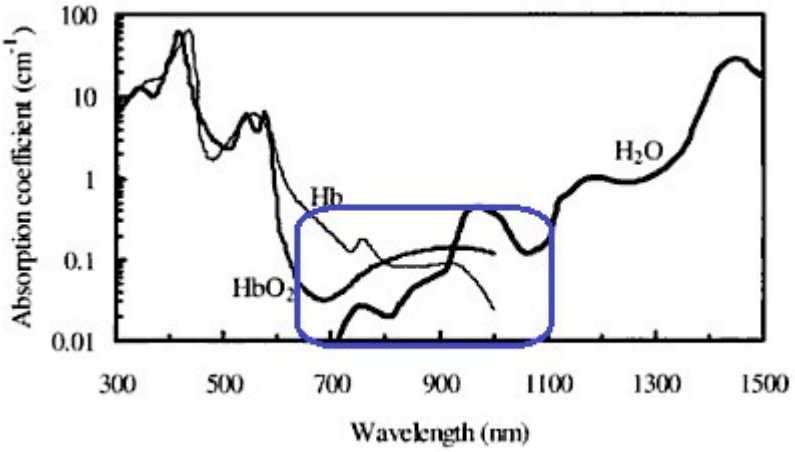

Figure I.4: Absorption spectra of the main constituent of tissues in the visible and near-infrared, namely oxy-haemoglobin (HbO2), deoxy-haemoglobin (Hb), and water (H2O). The spectra are obtained from compiled absorption data for water and haemoglobin.

Absorption only contributes to a fraction of photons loss at the detector but increases with higher wavelength. For deep red or near-infrared light, it only constitutes a negligible factor compared to scattering effects in a biological tissue. The other light attenuation phenomenon, scattering, being therefore predominant.

Scattering mechanisms in tissues.

For biological tissues, and breast tissues in particular, scattering accounts for 10 to 100 times more than absorption to the attenuation of incident light [73]. As for absorption, the scattering properties of a medium can be described by $\mu_{s.}$, the scattering coefficient. It can also be shown that

the reciprocal of the scattering coefficient $1/\mu_s$ or the mean free path which defines the mean distance between scattering events. This mean distance is of the order of 10 to 100 μm in biological tissues.

Light scattering is simply another description for the *propagation of an electromagnetic wave in matter*. When a wave is propagating in a medium, its electric field excite electron clouds from its constituent atoms and molecules. In tissues, it can be postulated that when an electromagnetic wave interacts with tissue constituents (e.g. a cell's nuclei, mitochondria or haemoglobin molecules), particles induced dipoles or multipoles oscillate with the frequency of the incident light wave. Electromagnetic energy is therefore re-emitted and its resulting intensity is therefore the coherent superposition of each individual sources and therefore its angular distribution depends upon the size, shape and gradient index of those tiny scatterers. When a collimated plane wave propagates in a non-absorbing homogeneous medium of length, L and filled with scattering particles, the exponential decrease of the collimated light's intensity that is traversing the medium is also given by the Beer-Lambert law, such that:

$$I_\tau = I_0 \, \mathrm{e}^{-\mu_s . L} \tag{2}$$

where μ_a is the scattering coefficient in [cm^{-1} or mm^{-1}], where I_t is the incident light or non-scattererd component of light after traversing a non-absorbing medium of thickness L.

In a tissue, light interacts with structures with a large variety of size and shapes, therefore a macroscopic scattering coefficient is generally defined by:

$$\mu_a = \sum_j N_j \sigma_{a.j} \tag{3}$$

where Nj is the number of particles j per unit volume and $\sigma_{a.j}$ the corresponding scattering cross section[4]. Frequently, a dimensionless phase function f(p,q) is used instead of the cross section, σ as represented in figure I.5. It represents the fraction of incident energy from the direction p and scattered in the direction q.

[4] *Scattering cross section is defined as the probability that the incident beam will be scattered per unit time (normalized to one particle per unit time crossing a unit area perpendicular to the direction of incidence) [2]*

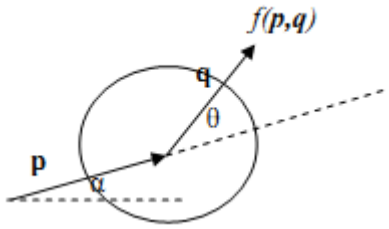

Figure I.5: Phase function f(p.q) schematic representation.

The flux increase in the second direction is due to scattering between the two events. In a random and isotropic media, it is assumed that the phase function is only dependent upon the angle between the incident and scattered light and therefore independent of the orientation of the scatterer (i.e. independent of p). The phase function can therefore be expressed as a scalar product f(p,q) = f(p.q), which is equal to the cosine of the scattering angle cos (θ). The anisotropy factor g, is then defined as the amount of forward direction retained after a single scattering event or the mean cosine of the deflection angle θ. For a g factor of 1, the scatter is entirely in the forward direction, and for g = 0, scattering is isotropic.

Light scattering in most biological tissues is generally forward concentrated (i.e. anisotropic) with g factors usually found in the literature varying from about 0.69 to 0.99 [73]. It is more generally centred around an average scattering angle of 25° (i.e. a scattered photon deviates from its initial direction of flight by only 25° or a g factor of 0.9)[75]. The anisotropy factor is therefore dependent on the size, shape and the microscopic refractive index mismatch of the scattering particles. Several approximation models attempt to describe those interactions of biological tissues with light.

Geometrical optics approximation:

Geometrical optics provide sufficient tools to describe the interaction of large particles with light and each particle can be envisioned as a thick lens. The light beam is therefore focused in a forward direction. However, geometrical optics concepts do not adequately describe the interaction of particles with light when the particle size is comparable to the wavelength of the light source.

The Mie solution to Maxwell's equations:

In that case, Mie theory (developed in 1908 by Gustav Mie) provides rigorous solutions to Maxwell equations for light scattering by an isotropic sphere in a homogenous medium. Mie theory takes into consideration the phase difference between dipoles, which receive a different incident field at a given instant. The resulting scattering is therefore predominantly forward directed in the same direction as the incident beam of light.

The Rayleigh solution to Maxwell's equations:

When the particle size is much smaller than the wavelength (typically the upper limit is taken to be about 1/10 the wavelength diameter), and then Mie theory turns into Rayleigh scattering theory. For a fixed, unpolarised incident wavelength, the intensity of the scattered wave is proportional to $(1+\cos^2\theta)$, as a function of the scattering angle θ, or more simply put, equally distributed in all directions (see figure I.6).

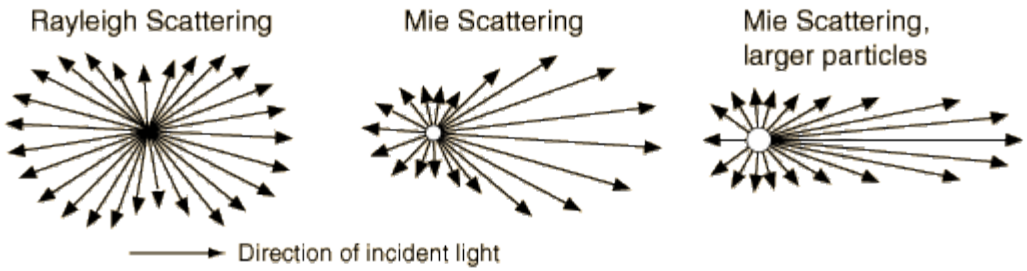

Figure I.6: schematic representation of scattering possibilities as a function of particle's size.

Wavelength dependence is another fundamental result of both Rayleigh and Mie theories and it has been shown that the intensity of the scattered wave is proportional to $1/\lambda^k$, where k depends upon the size of the scatterers as shown on figure I.7.

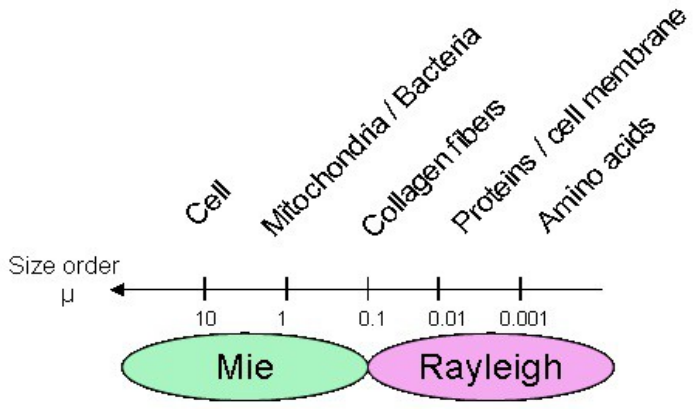

Figure I.7: Scattering regime relative to the size of the particle in biological specimens.

For small particles (Rayleigh scattering regime), the intensity of the scattered wave is approximately proportional to $1/\lambda^4$. Therefore, when the wavelength of the illumination source increases, scattering decreases faster than for Mie scattering. Isotropic scattering is mainly due to

smaller organelles, such as mitochondria, while scattering at small angles are largely due to the cell membrane whereas nuclei have been found to be responsible for scattering at larger angles or Mie scattering regime [76–78].

I.2.2 Conclusion

Only inhomogeneities affect light scattering. If a light beam traverses a perfectly homogeneous medium it is not scattered. Both refraction at tissue interface and at a microscopic level are affecting light's propagation in tissues. Refraction effects are usually small in biological tissues, as tissue refractive indexes are generally similar. A common index range varies between, n=[1.35:1.45] in the visible wavelengths, 1.35 for high water content tissues and up to 1.45 for adipose tissues [79], [80]. At 633 nm wavelength, the typical decrease trend relative to the wavelength is 1% in average per 100 nm decrease in wavelength in the visible range.

However, divergence in refractive index measurements have been reported in the literature as cited by Bolin et al. [79]. In practice, light scattering models often omit the refractive index approximation. For this thesis, all measurements performed in biological samples have been adjusted with an average refractive index of 1.40 for defocus correction as a function of depth. For small animal imaging, specific refractive index have been applied (e.g n=1.55 for Drosophila melanogaster due to its high content in chitin).

In summary, spatially coherent optical imaging in biological tissues faces the exponential loss of useful photons due to scattering events taking place as light travels through a particular tissue. Absorption has only a limited effect compared to scattering. Since scattering events redirect photons randomly, the amount of useful light or ballistic photons collected by the camera is significantly reduced causing blurring and reduced contrast. In addition, an appropriate wavelength selection allows to manipulate two critical criteria which are penetration depth and resolution.

References

[1] M. S. Linet et al., “Cancer risks associated with external radiation from diagnostic imaging procedures.,” *CA: a cancer journal for clinicians*, Feb. 2012.

[2] Kiyosi Ito, *Encyclopedic dictionary of mathematics*. MIT Press, 1993. *pp.1397*

[3] J. Pawley, “Handbook of biological confocal microscopy,” *Journal of Biomedical Optics*, 2008.

[4] H. Ra and W. Piyawattanametha, “Three-dimensional in vivo imaging by a handheld dual-axes confocal microscope,” *Optics …*, 2008.

[5] A. French, S. Mills, and R. Swarup, “Colocalization of fluorescent markers in confocal microscope images of plant cells,” *Nature protocols*, 2008.

[6] M. Egeblad and A. Ewald, “Visualizing stromal cell dynamics in different tumor microenvironments by spinning disk confocal microscopy,” *Disease models & …*, 2008.

[7] B. D. Bennett, T. L. Jetton, G. Ying, M. A. Magnuson, and D. W. Piston, “Quantitative subcellular imaging of glucose metabolism within intact pancreatic islets.,” *The Journal of biological chemistry*, vol. 271, no. 7, pp. 3647-51, Feb. 1996.

[8] S. Huang, A. A. Heikal, and W. W. Webb, “Two-photon fluorescence spectroscopy and microscopy of NAD(P)H and flavoprotein.,” *Biophysical journal*, vol. 82, no. 5, pp. 2811-25, May 2002.

[9] G. H. Patterson, S. M. Knobel, P. Arkhammar, O. Thastrup, and D. W. Piston, “Separation of the glucose-stimulated cytoplasmic and mitochondrial NAD(P)H responses in pancreatic islet beta cells.,” *Proceedings of the National Academy of Sciences of the United States of America*, vol. 97, no. 10, pp. 5203-7, May 2000.

[10] M. Han, G. Giese, and J. Bille, “Second harmonic generation imaging of collagen fibrils in cornea and sclera.,” *Optics express*, vol. 13, no. 15, pp. 5791-7, Jul. 2005.

[11] K. König, K. Schenke-Layland, I. Riemann, and U. A. Stock, “Multiphoton autofluorescence imaging of intratissue elastic fibers.,” *Biomaterials*, vol. 26, no. 5, pp. 495-500, Feb. 2005.

[12] S.-W. Teng et al., “Multiphoton autofluorescence and second-harmonic generation imaging of the ex vivo porcine eye.,” *Investigative ophthalmology & visual science*, vol. 47, no. 3, pp. 1216-24, Mar. 2006.

[13] J. K. Karen, D. S. Gareau, S. W. Dusza, M. Tudisco, M. Rajadhyaksha, and K. S. Nehal, “Detection of basal cell carcinomas in Mohs excisions with fluorescence confocal mosaicing microscopy,” *British Journal of Dermatology*, vol. 160, no. 6, pp. 1242-1250, 2009.

[14] K. S. Nehal, D. Gareau, and M. Rajadhyaksha, “Skin Imaging With Reflectance Confocal Microscopy,” *Seminars in Cutaneous Medicine and Surgery*, vol. 27, no. 1, pp. 37-43, Mar. 2008.

[15] V. Campo-Ruiz, E. R. Ochoa, G. Y. Lauwers, and others, “Evaluation of hepatic histology by near-infrared confocal microscopy: A pilot study,” *Human pathology*, vol. 33, no. 10, pp. 975–982, 2002.

[16] A. Parrish, E. Halama, M. T. Tilli, M. Freedman, and P. A. Furth, “Reflectance confocal microscopy for characterization of mammary ductal structures and development of neoplasia in genetically engineered mouse models of breast cancer,” *Journal of biomedical optics*, vol. 10, p. 051602, 2005.

[17] A. F. Fercher, W. Drexler, C. K. Hitzenberger, and T. Lasser, “OCT principles and applications,” *Reports on Progress in Physics*, vol. 66, no. 2, pp. 239-303, 2003.

[18] P. H. Tomlins and R. K. Wang, “Theory, developments and applications of optical coherence tomography,” *Journal of Physics D: Applied Physics*, vol. 38, no. 15, pp. 2519-2535, 2005.

[19] R. Leitgeb, C. Hitzenberger, and A. Fercher, “Performance of fourier domain vs. time domain optical coherence tomography,” *Optics Express*, vol. 11, no. 8, pp. 889-894, Apr. 2003.

[20] A. M. Zysk, F. T. Nguyen, A. L. Oldenburg, D. L. Marks, and S. A. Boppart, “Optical coherence tomography: A review of clinical development from bench to bedside,” *Journal of Biomedical Optics*, vol. 12, no. 5, pp. 051403-21, 2007.

[21] B. Karamata, “Multiple Scattering in Wide-field Optical Coherence Tomography,” ÉCOLE POLYTECHNIQUE FÉDÉRALE DE LAUSANNE, 2004.

[22] B. Liu and M. E. Brezinski, “Theoretical and practical considerations on detection performance of time domain, Fourier domain, and swept source optical coherence tomography,” *Journal of Biomedical Optics*, vol. 12, no. 4, pp. 044007-12, Jul. 2007.

[23] J. F. de Boer, B. Cense, B. H. Park, M. C. Pierce, G. J. Tearney, and B. E. Bouma, “Improved signal-to-noise ratio in spectral-domain compared with time-domain optical coherence tomography,” *Optics Letters*, vol. 28, no. 21, pp. 2067-2069, Nov. 2003.

[24] M. Szkulmowski, A. Szkulmowska, T. Bajraszewski, A. Kowalczyk, and M. Wojtkowski, “Flow velocity estimation using joint Spectral and Time domain Optical Coherence Tomography,” *Optics Express*, vol. 16, no. 9, pp. 6008-6025, Apr. 2008.

[25] D. Huang et al., “Optical coherence tomography,” *Science*, vol. 254, no. 5035, pp. 1178-1181, Nov. 1991.

[26] C. M. Eigenwillig, T. Klein, W. Wieser, B. R. Biedermann, and R. Huber, “Wavelength swept amplified spontaneous emission source for high speed retinal optical coherence tomography at 1060 nm,” *Journal of biophotonics*, 2011.

[27] J. M. Schmitt, “Methods and Apparatus for Swept-Source Optical Coherence Tomography,” *US Patent App. 13/030,886*. Google Patents, 18-Feb-2011.

[28] M. V. Sarunic, M. A. Choma, C. Yang, and J. A. Izatt, “Instantaneous complex conjugate resolved spectral domain and swept-source OCT using 3x3 fiber couplers,” *Optics Express*, vol. 13, no. 3, p. 957, Feb. 2005.

[29] M. A. Choma, M. V. Sarunic, C. Yang, and J. A. Izatt, “Sensitivity advantage of swept source and Fourier domain optical coherence tomography,” *Optics Express*. 08-Sep-2003.

[30] R. Leitgeb, C. Hitzenberger, and A. Fercher, “Performance of fourier domain vs time domain optical coherence tomography,” *Optics Express*, vol. 11, no. 8, p. 889, Apr. 2003.

[31] M. Choma, M. Sarunic, C. Yang, and J. Izatt, “Sensitivity advantage of swept source and Fourier domain optical coherence tomography,” *Optics Express*, vol. 11, no. 18, p. 2183, Sep. 2003.

[32] B. Potsaid et al., “Ultrahigh speed spectral / Fourier domain OCT ophthalmic imaging at 70,000 to 312,500 axial scans per second,” *Optics Express*, vol. 16, no. 19, pp. 15149-15169, 2008.

[33] R. A. Leitgeb et al., “Ultrahigh resolution Fourier domain optical coherence tomography,” *Optics Express*, vol. 12, no. 10, pp. 2156-2165, 2004.

[34] E. A. Swanson et al., “In vivo retinal imaging by optical coherence tomography,” *Optics Letters*, vol. 18, no. 21, p. 1864, Nov. 1993.

[35] R. B. Rosen et al., “Multidimensional en-Face OCT imaging of the retina,” *Optics Express*, vol. 17, no. 5, pp. 4112-4133, Mar. 2009.

[36] N. Nassif et al., “In vivo high-resolution video-rate spectral-domain optical coherence tomography of the human retina and optic nerve,” *Optics Express*, vol. 12, no. 3, pp. 367-376, Feb. 2004.

[37] Y. Wang, A. Fawzi, O. Tan, J. Gil-Flamer, and D. Huang, “Retinal blood flow detection in diabetic patients by Doppler Fourier domain optical coherence tomography,” *Optics Express*, vol. 17, no. 5, pp. 4061-4073, Mar. 2009.

[38] B. Cense et al., “Volumetric retinal imaging with ultrahigh-resolution spectral-domain optical coherence tomography and adaptive optics using two broadband light sources,” *Optics Express*, vol. 17, no. 5, pp. 4095-4111, Mar. 2009.

[39] T. P. M. Goderie et al., “Combined optical coherence tomography and intravascular ultrasound radio frequency data analysis for plaque characterization. Classification accuracy of human coronary plaques in vitro.,” *The international journal of cardiovascular imaging*, Apr. 2010.

[40] I.-K. Jang et al., “In Vivo Characterization of Coronary Atherosclerotic Plaque by Use of Optical Coherence Tomography,” *Circulation*, vol. 111, no. 12, pp. 1551-1555, Mar. 2005.

[41] D. Levitz et al., “Determination of optical scattering properties of highly-scattering media in optical coherence tomography images,” *Optics Express*, vol. 12, no. 2, p. 249, Jan. 2004.

[42] A. S. Paranjape et al., “Depth resolved photothermal OCT detection of macrophages in tissue using nanorose,” *Biomedical Optics Express*, vol. 1, no. 1, p. 2, 2010.

[43] I.-K. Jang et al., "Visualization of coronary atherosclerotic plaques in patients using optical coherence tomography: comparison with intravascular ultrasound," *Journal of the American College of Cardiology*, vol. 39, no. 4, pp. 604-609, Feb. 2002.

[44] G. Isenberg et al., "Accuracy of endoscopic optical coherence tomography in the detection of dysplasia in Barrett's esophagus: a prospective, double-blinded study," *Gastrointestinal Endoscopy*, vol. 62, no. 6, pp. 825-831, Dec. 2005.

[45] A. P. Weston, A. S. Badr, and R. S. Hassanein, "Prospective multivariate analysis of factors predictive of complete regression of Barrett's esophagus," *The American Journal of Gastroenterology*, vol. 94, no. 12, pp. 3420-3426, Dec. 1999.

[46] X. D. Li et al., "Optical coherence tomography: Advanced technology for the endoscopic imaging of Barrett's esophagus," *Endoscopy*, vol. 32, no. 12, pp. 921-930, 2000.

[47] John A. Evans et al., "Optical Coherence Tomography to Identify Intramucosal Carcinoma and High-Grade Dysplasia in Barrett's Esophagus," *Clinical gastroenterology and hepatology : the official clinical practice journal of the American Gastroenterological Association*, vol. 4, no. 1, pp. 38-43, Jan. 2006.

[48] G. Zuccaro et al., "Optical coherence tomography of the esophagus and proximal stomach in health and disease," *Am J Gastroenterol*, vol. 96, no. 9, pp. 2633-2639, 2001.

[49] J. M. Poneros and N. S. Nishioka, "Diagnosis of Barrett's esophagus using optical coherence tomography," *Gastrointestinal Endoscopy Clinics of North America*, vol. 13, no. 2, pp. 309-323, Apr. 2003.

[50] Y. Chen et al., "Ultrahigh resolution optical coherence tomography of Barrett's esophagus: preliminary descriptive clinical study correlating images with histology.," *Endoscopy*, vol. 39, no. 7, pp. 599-605, Jul. 2007.

[51] T. M. Bydlon et al., "Performance metrics of an optical spectral imaging system for intra-operative assessment of breast tumor margins," *Optics Express*, vol. 18, no. 8, p. 8058, Apr. 2010.

[52] F. T. Nguyen et al., "Intraoperative Evaluation of Breast Tumor Margins with Optical Coherence Tomography," *Cancer Res*, vol. 69, no. 22, pp. 8790-8796, Nov. 2009.

[53] A. M. Zysk and S. A. Boppart, "Computational methods for analysis of human breast tumor tissue in optical coherence tomography images.," *Journal of biomedical optics*, vol. 11, no. 5, p. 054015.

[54] R. a McLaughlin, L. Scolaro, P. Robbins, S. Hamza, C. Saunders, and D. D. Sampson, "Imaging of human lymph nodes using optical coherence tomography: potential for staging cancer.," *Cancer research*, vol. 70, no. 7, pp. 2579-84, Apr. 2010.

[55] N. V. Iftimia, M. Mujat, T. Ustun, R. D. Ferguson, V. Danthu, and D. X. Hammer, "Spectral-domain low coherence interferometry/optical coherence tomography system for fine needle breast biopsy guidance.," *The Review of scientific instruments*, vol. 80, no. 2, p. 024302, Mar. 2009.

[56] W. Luo et al., “Optical biopsy of lymph node morphology using optical coherence tomography,” *Technology in Cancer Research & Treatment*, vol. 4, no. 5, pp. 539-548, Oct. 2005.

[57] A. M. Zysk, E. J. Chaney, and S. A. Boppart, “Refractive index of carcinogen-induced rat mammary tumours,” *Physics in Medicine and Biology*, vol. 51, no. 9, pp. 2165-2177, 2006.

[58] B. J. Vakoc et al., “Three-dimensional microscopy of the tumor microenvironment in vivo using optical frequency domain imaging.,” *Nature medicine*, vol. 15, no. 10, pp. 1219-23, Oct. 2009.

[59] Y. Zhao et al., “Integrated multimodal optical microscopy for structural and functional imaging of engineered and natural skin.,” *Journal of biophotonics*, Feb. 2012.

[60] C. Li, G. Guan, X. Cheng, Z. Huang, and R. K. Wang, “Quantitative elastography provided by surface acoustic waves measured by phase-sensitive optical coherence tomography,” *Optics Letters*, vol. 37, no. 4, p. 722, Feb. 2012.

[61] B. F. Kennedy et al., “In vivo three-dimensional optical coherence elastography,” *Optics Express*, vol. 19, no. 7, p. 6623, Mar. 2011.

[62] E. Auksorius et al., “Dual-modality fluorescence and full-field optical coherence microscopy for biomedical imaging applications.,” *Biomedical optics express*, vol. 3, no. 3, pp. 661-6, Mar. 2012.

[63] M. Hagen-Eggert, D. Hillmann, P. Koch, and G. Hüttmann, “Diffusion-sensitive Fourier-domain optical coherence tomography,” in *Proceedings of SPIE*, 2011, vol. 7889, no. 1, p. 78892B-78892B-6.

[64] D. C. Adler et al., “Comparison of three-dimensional optical coherence tomography and high resolution photography for art conservation studies,” *Optics Express*, vol. 15, no. 24, p. 15972, Nov. 2007.

[65] T. Arecchi et al., “A new tool for painting diagnostics: Optical coherence tomography,” *Optics and Spectroscopy*, vol. 101, no. 1, pp. 23-26, Jul. 2006.

[66] M. Hughes, M. Spring, and A. Podoleanu, “Speckle noise reduction in optical coherence tomography of paint layers,” *Applied Optics*, vol. 49, no. 1, pp. 99-107, Jan. 2010.

[67] G. Latour, J.-P. Echard, B. Soulier, I. Emond, S. Vaiedelich, and M. Elias, “Structural and optical properties of wood and wood finishes studied using optical coherence tomography: application to an 18th century Italian violin.,” *Applied Optics*, vol. 48, no. 33, pp. 6485-6491, 2009.

[68] H. Liang et al., “En-face optical coherence tomography : a novel application of non-invasive imaging to art conservation,” *Optics Express*, vol. 13, no. 16, pp. 6133-6144, 2005.

[69] H. Liang, B. Peric, M. Hughes, A. Podoleanu, M. Spring, and D. Saunders, *Optical coherence tomography for art conservation and archaeology*, vol. 6618, no. 1. SPIE, 2007, pp. 661805-661805-12.

[70] J. Nimmrichter et al., *Lasers in the Conservation of Artworks*, vol. 116. Berlin, Heidelberg: Springer Berlin Heidelberg, 2008, pp. 487-492-492.

[71] M. Targowski, P., Iwanicka, L. Tymińska-Widmer, M. Sylwestrzak, and E. A. Kwiatkowska, "Structural examination of easel paintings with optical coherence tomography.," *Accounts of chemical research*, vol. 43, no. 6, pp. 826-36, Jun. 2010.

[72] P. Targowski, B. Rouba, M. Góra, L. Tymińska-Widmer, J. Marczak, and A. Kowalczyk, "Optical coherence tomography in art diagnostics and restoration," *Applied Physics A*, vol. 92, no. 1, pp. 1-9, Mar. 2008.

[73] W. F. Cheong, S. A. Prahl, and A. J. Welch, "A review of the optical properties of biological tissues," *IEEE Journal of Quantum Electronics*, vol. 26, no. 12, pp. 2166-2185, 1990.

[74] V G Peters et al, "Optical properties of normal and diseased human breast tissues in the visible and near infrared," *Physics in Medicine and Biology*, vol. 35, no. 9. p. 1317, 1990.

[75] F. Kiessling, *Small Animal Imaging*. Springer, 2010, p. 597.

[76] M. Bartlett, G. Huang, L. Larcom, and H. Jiang, "Measurement of Particle Size Distribution in Mammalian Cells In Vitro by Use of Polarized Light Spectroscopy," *Applied Optics*, vol. 43, no. 6, p. 1296, Feb. 2004.

[77] J. R. Mourant et al., "Light scattering from cells: the contribution of the nucleus and the effects of proliferative status.," *Journal of biomedical optics*, vol. 5, no. 2, pp. 131-7, Apr. 2000.

[78] A. M. K. Nilsson, C. Sturesson, D. L. Liu, and S. Andersson-Engels, "Changes in Spectral Shape of Tissue Optical Properties in Conjunction with Laser-Induced Thermotherapy," *Applied Optics*, vol. 37, no. 7, p. 1256, Mar. 1998.

[79] F. P. Bolin, L. E. Preuss, R. C. Taylor, and R. J. Ference, "Refractive index of some mammalian tissues using a fiber optic cladding method," *Applied Optics*, vol. 28, no. 12, p. 2297, Jun. 1989.

[80] G. J. Tearney, M. E. Brezinski, J. F. Southern, B. E. Bouma, M. R. Hee, and J. G. Fujimoto, "Determination of the refractive index of highly scattering human tissue by optical coherence tomography," *Optics Letters*, vol. 20, no. 21, p. 2258, Nov. 1995.

[81] N.Graf, "Optical Coherence Tomography," *Vanderbiilt University*, 2010. [Online]. Available: http://research.vuse.vanderbilt.edu/skalalab/optical-coherence-tomography.html. [Accessed: 30-Dec-2011].

[82] D. et al. Sampson, "OBEL: Introduction to optical coherence tomography (OCT)," 2004. [Online]. Available: http://obel.ee.uwa.edu.au/research/oct/intro/. [Accessed: 01-Jan-2012].

Chapter II. Full-Field OCT system: design principles and performance

As presented in the introductory chapter, previous work in OCT have been performed with beam scanning techniques over the volume of interest. Full-field OCT (FFOCT) is based on a Time-Domain approach and acquires an entire field of view by using a Linnik configuration coupled with an image detector such as a CCD camera. This parallel approach is usually referred to “en-face” OCT as opposed to a cross-sectional view in traditional OCT imaging. While conventional OCT is often compared to the optical analogue of B-mode ultrasound, FFOCT would be conceptually closer to a depth resolved microscopy technique. The transverse resolution achieved is indeed similar to a low or medium power microscope with the ability to image inside a biological sample without any staining or specimen fixation. Potential end-users would therefore be predominantly in histopathology and biology laboratories in comparison to traditional OCT which is more aimed at surgical settings or for screening purposes.

After a presentation of the principles of full-field OCT, its design and performance are described. Then the clinical setup developed by the laboratory spin-off (LLTech) will be briefly presented. Finally, the main advantages and drawbacks of the technique are discussed. Throughout the chapter technical considerations of the system and image acquisition methods are also analysed.

The contribution of several members of the laboratory and LLTech team must be appropriately acknowledged in advance. This presentation involves the previous work of Laurent Vabre, Gael Moneron and Arnaud Dubois under the direction of Claude Boccara at ESPCI laboratory; and the more recent contribution of Fabrice Harms, Eugénie Dalimier and Franck Martins from LLTech. Charles Brossolet has been instrumental in all the software related issues of this work. The basic principles of the technique have been previously detailed [1–2], while recent results and developments in relation to this chapter were reported in two publications [3–4].

II.1 Full-field OCT: basic principles

II.1.1 Description of the FF-OCT setup

The full-field OCT experimental setup is based on a Michelson interferometer with identical water-immersion objectives in both arms. It is commonly referred to a Linnik configuration [5], [6] as shown on figure II.1.

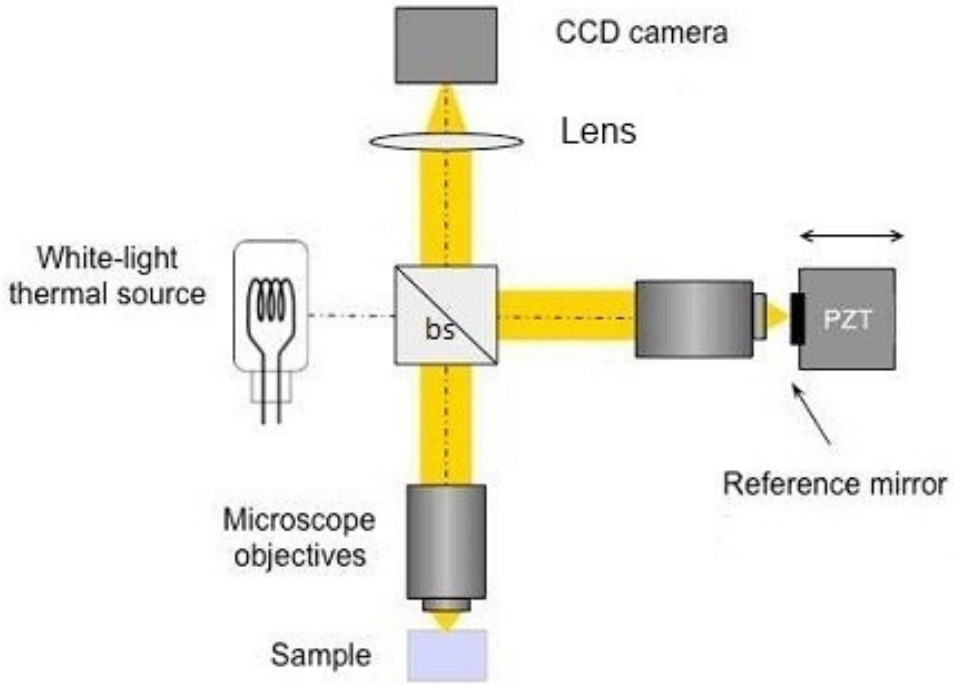

Figure II.1: Experimental set-up of the full-field OCT developed at ESPCI/Institut Langevin. Pair of microscope objectives (water or oil immersion – 10X, 0.3 NA, Olympus), bs: beam-splitter (broadband, non polarizing), Lens: achromatic doublet, Reference mirror: 1-10% reflectivity, PZT: oscillating piezoelectric stage actuator , CCD: charged coupled device camera or CMOS camera complementary metal-oxide semiconductor. Glass plates can be added within the path of both objectives for dispersion balance.

FFOCT is based on low-coherence interferometry as conventional OCT. However, here a white-light halogen lamp is used as a spatially incoherent source and the entire field of view of each microscope objectives is illuminated after passing through a beam splitter. The tungsten filament lamp is incorporated in a classical Köhler configuration to achieve the most homogeneous illumination.

A broadband beam splitter separates the light beam onto a mirror (reference arm) and onto the specimen imaged (sample arm). A silicone-based wafer mirror is placed in the reference arm at the focus of the microscope objective. The initial silicon-based wafer used for the experimental setup and providing a reflectivity of 17.5% in silicone oil for the wavelength region of interest (600-

800 nm) was later adjusted in the clinical setup developed by LLTech to match the reflectivity of biological tissues (around 2-3%). A YAG crystal rod (Yttrium Aluminium Garnet) can also be used due to its low reflectivity in the visible and in water immersion (reflectivity close to 2-3%). The major downside of a water-based medium (e.g. echographic gel) is its instability and low resistance to evaporation. Despite having both arms sealed, gel dehydration can still occur and cause irreversible blurring on the objectives. For the clinical setup, silicone oil was therefore determined more adapted as immersion liquid for both arms with similar optical properties if not improved (see chapter VI).

II.1.2 Temporal low-coherence and slice sectioning in FFOCT

Axial scanning is performed via a motorized translation stage allowing sequential image acquisition with slices as thin as 1 micron. The setup sectioning ability is directly related to the low temporal coherence of the light source. Interferences occur only when the light from both arms has travelled a nearly identical “optical distance” as shown on figure II.2.

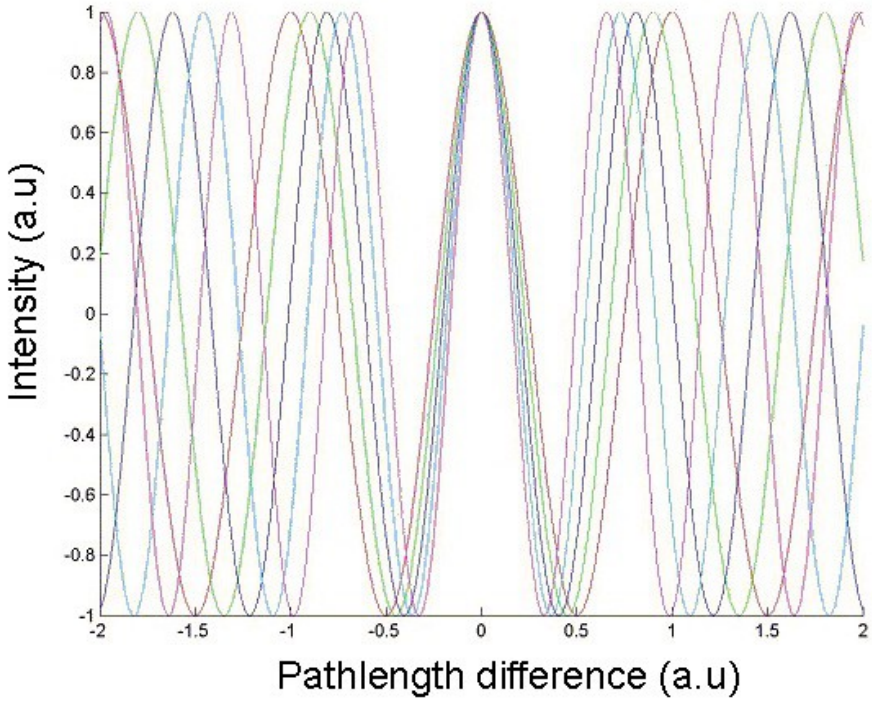

figure II.2: interferogram example of a low-coherence illumination source; hence its micron-scale sectioning ability .

The low temporal coherence gate therefore allows only interferences within half of the coherence length. Consequently, only a slight difference in pathlength travelled causes the interferometric image to be blurred by background noise. When light reflected by the reference mirror interferes with the light reflected or backscattered by the sample, micro-structures contained within the volume are filtered out from the specimen. This virtual zone is a slice orthogonal to the objective axis, located at a depth inside the object defined by an optical path length difference of zero. If the

object arm is moved forward or backward, a different sectioning volume is imaged. The sectioning thickness is determined by the width of the fringe envelope amplitude. This is commonly measured by the full-width at half maximum (FWHM) of the signal amplitude and is equivalent to the axial resolution as detailed further in this chapter. The tomographic image is finally obtained by combining interferometric images with a phase shift accomplished by displacement of the reference mirror with a piezoelectric translation stage.

II.1.3 Image acquisition method

The full-field “en-face” tomographic image is obtained via a phase-shift method in order to extract the coherent interferometric signal from the specimen. The backscattered light intensity received by each pixel (x,y) of the CCD camera over time can be expressed by the following equation (interference signal of two waves):

$$I(x,y,t)=\frac{I_0}{4}[R_{inc}(x,y)R_{ref}(x,y)+2\sqrt{R_{obj}(x,y)\times R_{ref}(x,y)}\cos(\Phi(x,y)+\Psi) \quad (4)$$

where I_0 is the photon flux at the entrance of the interferometer, $R_{inc}(x, y)$ is the proportion of light reflected by the object that does not interfere, due to other reflectors in the sample arm path combined with external signal noise from the instrument; R_{ref} represents the homogeneous reference mirror reflectivity, since the system is illuminated via a Khöler illuminator providing a quasi uniform beam of light. Within the interference term, $R_{obj}(x, y)$ represents the proportion of light reflected by the object that interferes with the reference mirror and more precisely, $R_{obj}(x, y)$ is the reflectivity distribution from structures contained in the sample's coherence volume and thus the “en face” tomographic image that actually needs to be extracted. As the result of the interference pattern, the cosine term is composed of the unknown phase difference, Φ between the reference mirror and the object signal; and the additional term Ψ accounts for the phase-shift induced by the displacement of the reference mirror.

A phase-shift method is used to reduce the amount of incoherent signal and to extract the amplitude of the interference (the fringe envelope) from the sample (i.e. $R_{obj}(x, y)$). Practically, only two to four images are sufficient to reduce the incoherent signal. For example, by acquiring four successive values of Ψ: 0, π/2, π, 3π/2, and by computing the squared difference of shifted frame, it becomes possible to isolate the term: $\sqrt{R_{obj}(x,y)\times R_{ref}(x,y)}$, proportional to $R_{obj}(x,y)\times R_{ref}(x,y)$ or $\sqrt{R_{obj}(x,y)}$, the amplitude of the backscattered signal intensity.

Alternative phase-shifting methods have been suggested with steps and sinusoidal phase modulations from 2 to 7 successive phase-shifts [1], [7–9]. However, if only two images are

acquired (with an incrementation of π between the two phases), the squared difference of these two images do not completely eliminate the phase difference term.

Nonetheless, the acquisition of two rather than four or more frames should not alter the signal collected. FFOCT and OCT images in general always display a speckle pattern due to the interference of light backscattered by the distribution of micro-structures located inside the coherence volume. Thus, it suggests that the backscattered signal amplitude and phase are both random. Ultimately, it is mostly dependent upon the acquisition speed desired. This time is simply doubled with four successive phase-shifts.

After the extensive number of images analysed and a large number with diagnostic intent, it appeared that the additional incoherent signal collected with a two-phase acquisition mode did not prevent the image interpretation by histopathologists or researchers.

As previously detailed, the computing processes involves basic image subtraction and can therefore be rapidly computed. Data were acquired via a software developed in LabVIEW™ (National Instruments Corporation, Austin, Texas), and the resulting tomographic image could be visualized in quasi real-time with the home-made interface (see figure II.3).

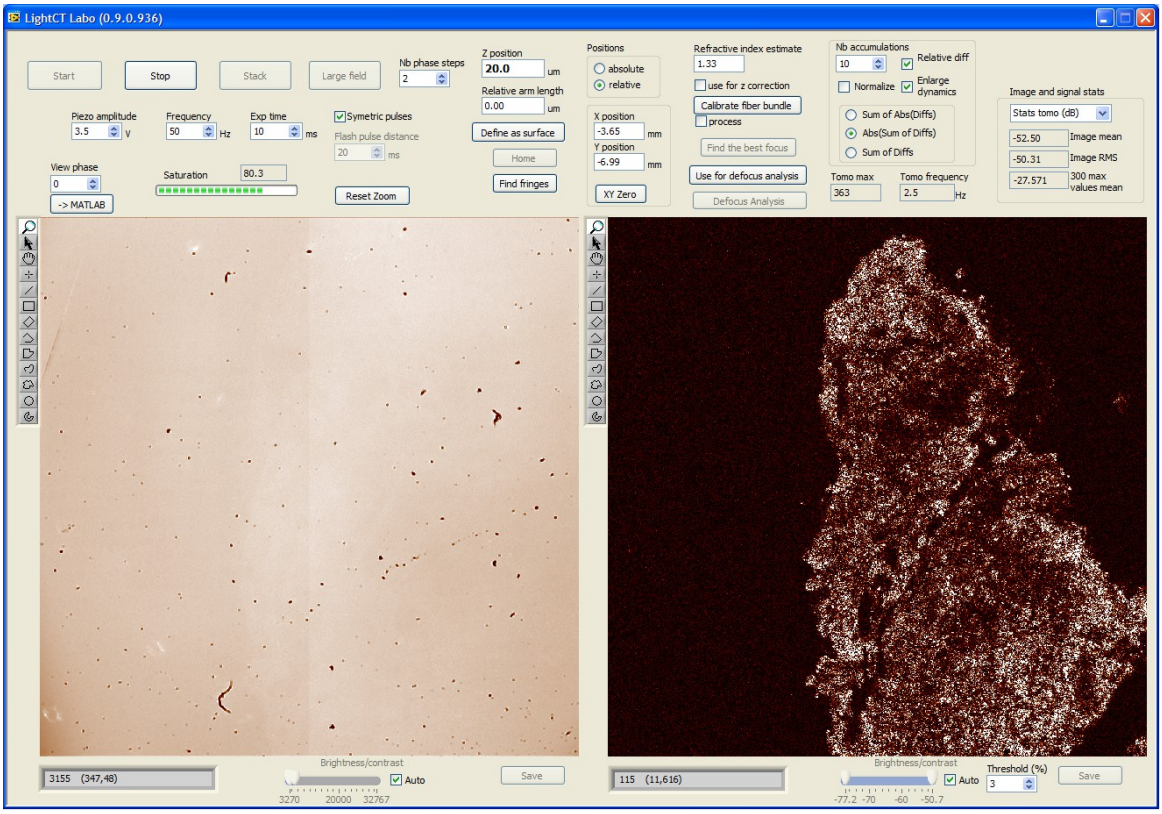

figure II.3: image acquisition graphical interface showing the tomographic image (on the right) and the direct image (on the left). Imaging depth is already 20µm underneath the surface, which explains the blurring and low signal from the direct image. Software developed in LabVIEW by Ch.Brossolet.

The presence of signal (in white) shows that an element in the specimen is backscattering light to the camera whereas absence of signal or a weak signal (in “black”) does not necessarily imply that photons are not being backscattered at this particular pixel within the coherence plane. Several aspects are to be considered: the absence of signal does not equate absence of structure but absence of backscattering structures within the coherence plane and it is directly related to the light source spectrum. It generally means that the structure is either fluid-filled or out of the coherence depth of field (owing that defocus has been corrected), due to micro riddles or cavities on the sample surface; and more rarely due to high absorption of the emitted light.

Although scattering effects from small-size refractive index heterogeneities are limited with FFOCT approach (below the size of a micron), larger refractive index heterogeneities are however present in biological tissues (e.g collagen fibres, organelles,...) and also concur to the loss of contrast as imaging goes deeper into the sample. It has been shown that adaptive optics corrections are not necessary for the penetration depth (up to 200 µm) since defocus effects are dominant as detailed in the following section.

II.1.4 Tomography and coherence plane dynamic adjustment

A 3-D tomographic image is acquired by displacement of the focal plane at different depths below the surface and a stack of “en-face” images is thus collected. As the objective is displaced along the z-axis, the focus is shifted forward whereas the coherence plane is moved backward as shown on figure II.4.

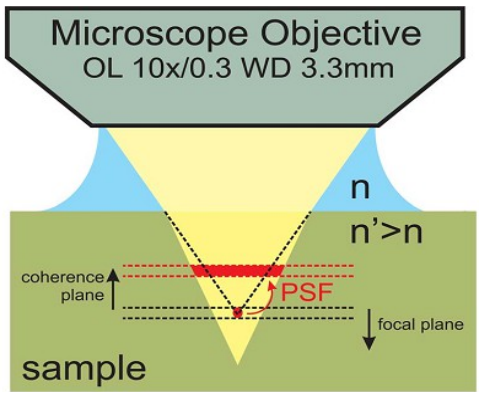

figure II.4: focal and coherence plane mismatch with depth penetration inside a sample. From [11]

This characteristic can benefit refractive index measurements –and has been used for that purpose in highly scattering tissues [10]. For the purpose of imaging deep within a specimen, a dynamic adjustment is necessary to compensate for the loss in resolution in relation to depth. In this setup, it is done by aligning the coherence plane with the objective focal plane during the scanning process. The following compensation factor is applied to the reference arm as detailed in [11] :

$$\delta_{(z)} = 2z\,\frac{(n'^2 - n^2)}{n} \qquad (5)$$

where $\delta_{(z)}$ is the optical path difference or phase shift between the object and the reference arm, a difference induced by the mismatch of refractive index between the biological sample n', and the immersion medium n (water or silicone oil) and dependent upon the depth being probed. The plane of zero path difference or coherence plane is therefore aligned with the focal plane by displacing the reference arm -the objective and reference mirror are then kept in focus. The cut-off depth at which the adjustment is necessary is highly dependent upon the biological sample being imaged. This limit can be approximated by comparing the ratio $\delta_{(z)}/2n'$ relative to the depth of field. For the microscope objectives used during this work, mainly 10X 0.3 NA water immersion, the depth of field is typically around 8.5 µm (wavelength centred at 700 nm and Δλ=125 nm). According to the refractive index of the specimen studied, the following table provide a summary of the threshold depth at which defocus correction is deemed necessary:

Specimen refractive index, n'	**1.37**	**1.4**	**1.45**	**1.5**	**1.55**
Depth threshold (in µm) Water immersion (n=1.33)	*145*	*85*	*50*	*36*	*28*
Depth threshold (in µm) Oil immersion (n=1.40)			*115*	*60*	*40*

The average refractive index in biological tissues is around 1.377 and does not require a specific adjustment up to 145 µm in depth. However, for small animal studies (see chapter on in-vivo imaging of drosophila growth), the main constituent of insects' external coating is characterized by a refractive index around 1.55 (e.g. chitin component of the cuticle or pupal case). Thus, a dynamic focus adjustment is relevant and ought to be applied from the imaging onset.

II.1.5 Image post-processing

Post-processing filters are particularly mild and limited to basic smoothing operations. Images always contain some form of speckle due probably to backscattered photons interference following the interaction with different tissue micro-structures located inside the coherence volume. Yet, speckle is both a source of noise and a carrier of information. Numerous methods have been proposed for reducing speckle noise in coherent imaging systems. Among the most popular post-processing methods are median and Wiener filtering, smoothing, and wavelet analysis [12–15]. In

the current configuration, experimental data did not require any of those post-processing methods. For the clinical work performed the aforementioned filters were seldom used, except for a Gaussian smoothing whereby each pixel it replaced with the average of its 3×3 neighbourhood pixels. Otherwise, a Gaussian blur convolution for smoothing was applied with the image viewing software imageJ. The Gaussian function applied was generally between 1 to 3 standard deviation (i.e. radius of 1.0 to 3.0).

II.2 System performance: spatial resolution

As previously seen, the transverse and axial resolution in FFOCT are uncorrelated. The sectioning ability along the z-axis is solely dependent upon the light source temporal coherence: a low-coherence or a large spectrum allows a highly resolved sectioning. In contrast to the spectrum of ultra-short femtosecond lasers, a thermal light source provides a particularly smooth and stable spectrum. It avoids emission lines spikes, bumps or ripples that could potentially cause side lobes in the coherence function and creates artefacts.

Nonetheless, the effective spectrum is actually limited by the spectral response of the camera (CCD or CMOS[5]). With a CMOS image sensor camera (Photonfocus®), the effective spectrum is centred at λ=700 nm and provides a bandwidth of $\Delta\lambda$=125 nm at full width half maximum (FWHM), following the usual formula (valid for a Gaussian spectral profile):

$$d_z = \frac{2\ln 2}{n\pi}\left(\frac{\lambda^2}{\Delta\lambda}\right) \quad (6)$$

Thus, the theoretical axial resolution achieved in a medium is below 1 µm with (d_z = 0.8 µm) with a refractive index n= 1.377 for a typical biological sample. Experimental results show rather an axial resolution in the range of 1.1–1.4 µm depending on the camera and setup configuration. This loss in resolution is certainly due to dispersion occurring in one of both arms; a slight mismatch from the ideal zero path difference can also easily deteriorate the point spread function along the z-axis. As detailed in the previous section, several compensation methods can be implemented. Since water is the main constituent of biological tissues, the use of water-immersion microscope objectives help to minimize dispersion mismatch. In addition, for the experimental setup, thin glass plates, placed in both arms of the interferometer, can be tilted to compensate for residual dispersion.

In the x-y axis, the transverse or lateral resolution is in fact similar to traditional microscopy with the objective numerical aperture (NA) as determining factor. For a focused beam, the transverse spot can therefore be determined by the Airy function:

[5] *CMOS stands for Complementary Metal–Oxide–Semiconductor and CCD for Charge-Coupled Device.*

$$d_x = \frac{1.22\lambda}{2\,NA} \qquad (7)$$

For a central wavelength around 700 nm and a numerical aperture of 0.3 [NA], the theoretical transverse resolution achieved is approaching 1.4 µm.

In comparison, traditional cross-sectional OCT systems are highly limited in transverse resolution since probing the entire depth of field in the axial plan is required. To generate an image, the focus is fixed at a specific depth in the sample and then the coherence gate is scanned along the z-axis. A larger depth of field is therefore required to avoid dynamic focusing as the coherence gate is being scanned. Only low NA lenses are then used to obtain a large depth of field, which consequently limits the transverse resolution. Obviously it is a trade-off between resolution and depth penetration if one compares to traditional OCT systems.

II.3 Compact clinical setup

In 2008, a spin-up from the ESPCI laboratory has been set-up to develop the potential clinical applications of FFOCT. A photograph of the prototype and a "pre-commercial" setup is shown on figure II.5 and II.6.

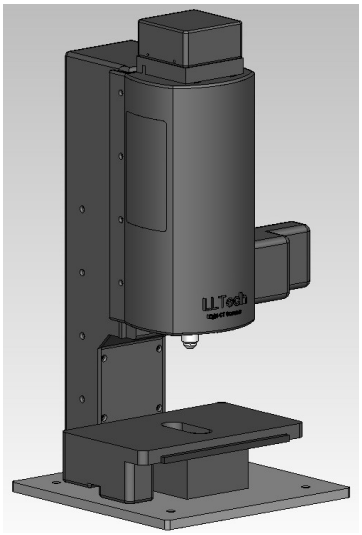

Figure II.5: FFOCT prototype – Light-CT– developed by LLTech®.

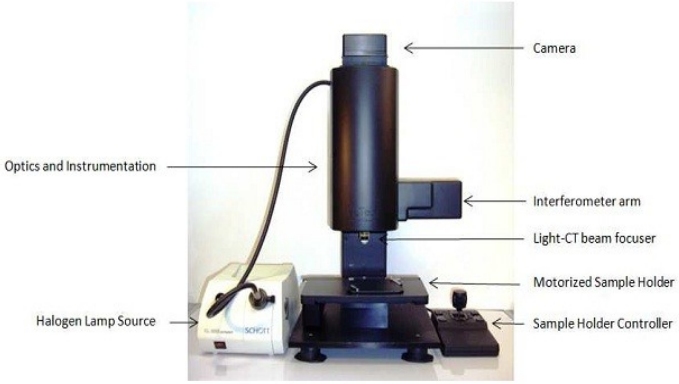

Figure II.6: fully operational clinical setup with description of the assembled components.

The design of a clinical setup has involved a number of fine adjustments from the experimental configuration. For instance, the replacement of the reference arm immersion medium by silicone oil. Initially, the immersion medium for both arms was a water-based gel (similar to those used for ultrasound echography) frequently turning opaque and highly scattering if exposed to air or

high temperatures. Silicone oil provides a stable alternative as immersion medium and minimizes the dispersion mismatch due to a refractive index closer to the average index for biological samples (i.e. n'=1.40).

For convenience, the thermal light source is powered by a compact halogen fibre-bundle filtered in the red and near-infrared providing an intensity of 1–2 mW/mm^2. Another example of fine-tuning is the addition of a synchronized snapshot camera which enables a co-localization of the direct sample image with the tomographic area as illustrated on figure II.7.

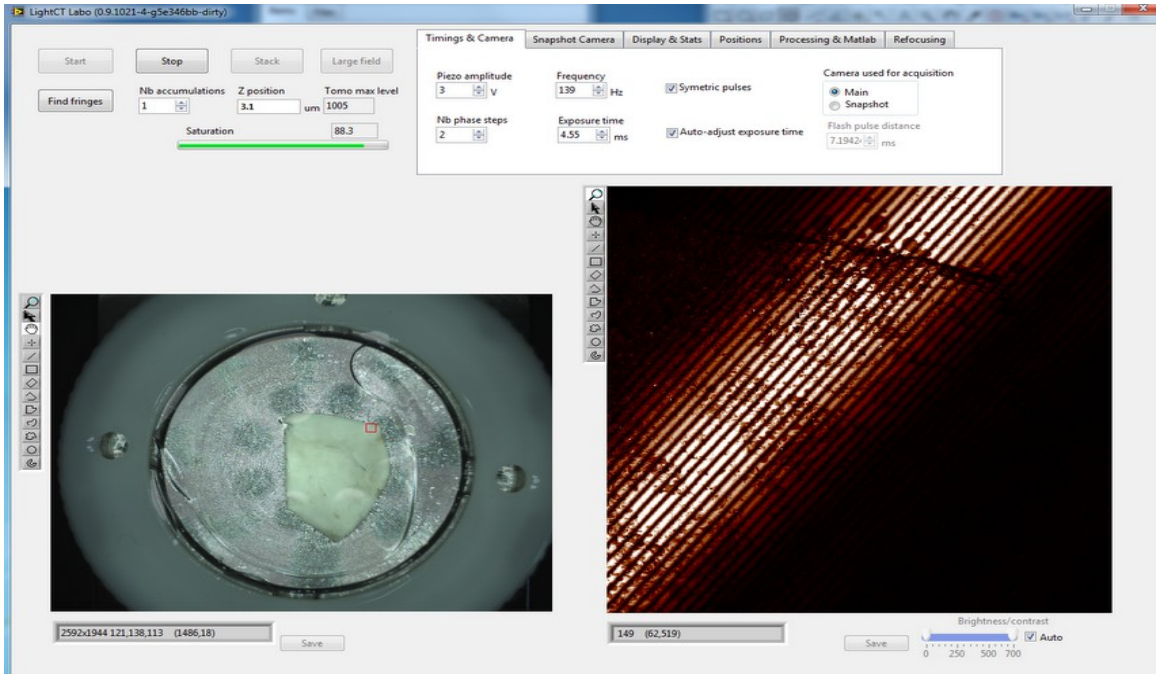

figure II.7: field of view of 1x1 mm² and corresponding tomographic image at glass slide-specimen interface.

Software developments are also crucial for end-user usage. The implementation of the dynamic adjustment has been added to automatically adapt to the tissue refractive index. Likewise, large field of views are constantly required since clinical specimen often measure several millimetres.

Fast stitching of individual images is therefore crucial and for an approximate field of view of 1 cm^2, the LightCT stitching algorithm enables for example 144 individual tiles of 1 mm² each to be cross-correlated in less than 3 minutes for a total surface of 1cm^2 (with an overlap of 20% between individual tiles).

In addition to the two clinical studies performed at Institut Curie during this work, an additional collaboration was initiated at Tenon Hospital, Paris with a grant from the French institute for Cancer (INCa). More recently, several hospitals and medical centre in the United-Stated have launched research projects with the pre-commercial version of the equipment. In particular, a study

on small-animal imaging was recently performed on organs and tissues of rat models at Weill Cornell Medical College, New-York, USA [3].

II.4 Conclusion

The Full-Field OCT system presented in this chapter offers the advantage of simplicity and high-resolution with parallel image acquisition of a large field of view compared to traditional cross-sectional OCT techniques. In addition, FFOCT produces three-dimensional “en-face” images with unmatched isotropic resolution of approximately 1.5 µm. This chapter also detailed the algorithm used for the dynamic adjustment of the reference arm as a function of depth and tissue refractive index. The adaptation of the system for a clinical application required a number of fine adjustments implemented by the team from LLTech, including among others, thermostability of the immersion medium and selection of compact components.

FFOCT is inherently a versatile technique since transverse and axial resolution are independent from each other. This provides a crucial advantage compared to other tomographic methods such as confocal microscopy. For example, the light source can successfully be replaced by a multi-LED fibre bundle instead of a tungsten-halogen lamp [16]. Likewise, objectives can be replaced by higher numerical aperture or magnification objectives although some adjustments would be necessary. One can also envision coupling fluorescence detection with FFOCT high sectioning ability. A research project in collaboration with LLTech is currently investigating its feasibility. Nonetheless, FFOCT in its current configuration, is limited for an adaptation to higher axial scanning speed because of its inherent sensitivity to motion. The number of accumulated images required scale inversely with the minimum contrast necessary to extract a valuable diagnostic information. Innovative approaches have been recently proposed to overcome those limitations and to incorporate a similar configuration into miniaturized or endoscopic probes [17–19].

References

[1] A. Dubois, G. Moneron, K. Grieve, and A. C. Boccara, “Three-dimensional cellular-level imaging using full-field optical coherence tomography,” *Physics in Medicine and Biology*, vol. 49, no. 7, pp. 1227-1234, Apr. 2004.

[2] L. Vabre, A. Dubois, and A. C. Boccara, “Thermal-light full-field optical coherence tomography.,” *Optics Letters*, vol. 27, no. 7, pp. 530-532, 2002.

[3] M. Jain, N. Shukla, M. Manzoor, S. Nadolny, and S. Mukherjee, “Modified full-field optical coherence tomography: A novel tool for rapid histology of tissues.,” *Journal of pathology informatics*, vol. 2, no. 1, p. 28, Jan. 2011.

[4] E.Dalimier and D.Salomon, “Full-Field Optical Coherence Tomography: A New Technology for 3D High-Resolution Skin Imaging,” *Dermatology*, 2012.

[5] A. Dubois, L. Vabre, A.-C. Boccara, and E. Beaurepaire, “High-resolution full-field optical coherence tomography with a Linnik microscope.,” *Applied optics*, vol. 41, no. 4, pp. 805-12, Feb. 2002.

[6] G. S. Kino and S. S. C. Chim, “Mirau correlation microscope,” *Applied Optics*, vol. 29, no. 26, p. 3775, Sep. 1990.

[7] A. Dubois, G. Moneron, and A. C. Boccara, “Thermal-light full-field optical coherence tomography in the 1.2 mu m wavelength region,” *Optics Communications*, vol. 266, no. 2, pp. 738-743, 2006.

[8] J. Na, W. J. Choi, E. S. Choi, S. Y. Ryu, and B. H. Lee, “Image restoration method based on Hilbert transform for full-field optical coherence tomography,” *Applied Optics*, vol. 47, no. 3, p. 459, Jan. 2008.

[9] E. Bordenave et al., “Wide-field optical coherence tomography: imaging of biological tissues,” *Applied Optics*, vol. 41, no. 10, p. 2059, Apr. 2002.

[10] G. J. Tearney, M. E. Brezinski, J. F. Southern, B. E. Bouma, M. R. Hee, and J. G. Fujimoto, “Determination of the refractive index of highly scattering human tissue by optical coherence tomography,” *Optics Letters*, vol. 20, no. 21, p. 2258, Nov. 1995.

[11] S. Labiau, G. David, S. Gigan, and A. C. Boccara, “Defocus test and defocus correction in full-field optical coherence tomography,” *Optics Letters*, vol. 34, no. 10, pp. 1576-1578, May 2009.

[12] J. Schmitt, “Speckle in optical coherence tomography,” *Journal of Biomedical Optics*, 1999.

[13] R. Bernstein, “Adaptive nonlinear filters for simultaneous removal of different kinds of noise in images,” *IEEE Transactions on Circuits and Systems*, vol. 34, no. 11, pp. 1275-1291, Nov. 1987.

[14] J. M. Schmitt, “Array detection for speckle reduction in optical coherence microscopy,” *Physics in Medicine and Biology*, vol. 42, no. 7, pp. 1427-1439, 1997.

[15] G. Franceschetti, V. Pascazio, and G. Schirinzi, “Iterative homomorphic technique for speckle reduction in synthetic-aperture radar imaging,” *Journal of the Optical Society of America A*, vol. 12, no. 4, p. 686, Apr. 1995.

[16] D. Sacchet, “Tomographie par cohérence optique plein champ linéaire et non linéaire,” 2010.

[17] A. Latrive and A. C. Boccara, “In vivo and in situ cellular imaging full-field optical coherence tomography with a rigid endoscopic probe.,” *Biomedical optics express*, vol. 2, no. 10, pp. 2897-904, Oct. 2011.

[18] H. D. Ford and R. P. Tatam, “Fibre imaging bundles for full-field optical coherence tomography,” *Measurement Science and Technology*, vol. 18, no. 9, pp. 2949-2957, Sep. 2007.

[19] W.-Y. Oh, B. E. Bouma, N. Iftimia, R. Yelin, and G. J. Tearney, “Spectrally-modulated full-field optical coherence microscopy for ultrahigh-resolution endoscopic imaging.,” *Optics express*, vol. 14, no. 19, pp. 8675-84, Sep. 2006.

Chapter III. Breast ex-vivo imaging: from laboratory to clinical setting

This chapter describes ex-vivo studies performed with a compact FFOCT system. The objective of this work was to assess the ability of the technique to visualize morphological and cellular features of normal, benign and malignant lesions of breast tissue. The two studies presented here provide a broad assessment of characteristic features of malignancy as identified by FFOCT. Large field specimen and core-needle biopsies are being systematically compared to gold standard histology. In addition, this work expands previous ex-vivo work with Full-Field OCT and provides insight into the relative advantage and disadvantage of this approach.

Clinical work was performed with the help of clinicians from two institutions in Paris. Dr. Brigitte Sigal from Institut Curie and Dr. Martine Antoine from Tenon hospital made possible the collection of specimens in the pathology laboratory and the diagnostic evaluation of both tomographic images and corresponding histology. Likewise, Dr. Vincent Servois, radiologist was instrumental in facilitating the needle biopsy study within the imaging unit at Institut Curie, Paris.

III.1 Large field imaging of ex-vivo breast tissues.

III.1.1 Background

To date, only a few studies have been reported about the capability of high-resolution OCT to aid in the visualization of normal and pathologic breast structures at the micron scale [1]. An isotropic resolution up to 3 µm is commonly referred to high-resolution or ultra high-resolution in optical coherence tomography literature[2–4]. As a comparison, a similar level of resolution is provided by low or medium power microscopy (4X magnification). According to histopathologists consulted, a majority of common pathologies could potentially be detected and assessed with low

power magnification on stained histological slides. A morphological assessment could therefore in theory be sufficient for most pathologies. This work attempts to address this hypothesis by methodically comparing tomographic information with gold standard histology.

Despite advances in early detection of breast cancers through breast imaging techniques such as ultrasound, mammography or CT scans, breast cancer remains among women the most prevalent cancer worldwide [5]. In addition, the increase of more sensitive screening techniques for breast cancer has lead to a rise in surgical procedures. However, 14–40% of patients still require a second surgical procedure due to positive or close margins [6], [7]. Positive margins are defined as tumour cells appearing directly at the cut edge of the excised specimen. Residual tumour left bear the risk of local recurrence and require additional surgery for the patient [8-11].

Among the intra-operative margin assessment techniques, frozen section analysis has been shown to reduce the rate of second operations to about 20% [12], however its rationale in clinical routine is being questioned in the literature [13], [14]. Although the accuracy of frozen-section is very high [13], [15–18], it has been suggested inappropriate with very small tumours (<1 cm) [19] and may also compromise final diagnosis by leaving insufficient material for permanent paraffin embedding or for tumour markers in molecular analysis.

A second issue with frozen-section analysis is the cost benefit rationale. Initially, it was used during surgery with a diagnostic purpose and dictated further tumour removal if repetitive positive margins were found during surgery. Cost-benefit was evident as immediate diagnosis could avoid a potential second operation for the patient. As E.Singletary pointed out: "i*n theory, a patient scheduled for lumpectomy who is found to have repeatedly positive margins after multiple re-excisions would be a candidate for an immediate mastectomy*[6]*. However, many institutions are reluctant to perform the mastectomy in the same surgery under these circumstances"[20] .*

The main reasons are the psychological effects for the patient of not expecting major surgery such as a mastectomy and the lack of preparation regarding a breast-conserving surgery. Patients scheduled for a mastectomy are now widely offered immediate reconstruction. Likewise such procedure also requires extensive time and coordination among specialists and cannot be immediately scheduled without a minimum notice. Therefore, the cost-benefit of frozen-section with treatment intend has altered.

In addition, with the development of less invasive biopsy and imaging techniques, primary intent of surgical procedures have shifted from diagnosis to treatment. As diagnostic has already been confirmed, surgery is now primarily intended to remove a tumour (lumpectomy) or the entire breast (mastectomy). Consequently, intraoperative frozen-section analysis has become largely restricted to margin assessment whereby the edges of the lesion are inspected to determine if the excised lesion is free from residual tumour. While studies have shown a fewer number of second operations to about 20% [20], several drawbacks have been reported such as a high rate of false negatives (around 20% of patients required additional operation). It must be noted that the vast majority of

[6] *Surgical removal of one of both breasts.*

hospitals in the United States do not rely on intraoperative margin assessment by pathologists [22]. According to pathologists interviewed, a similar trend is observed in France, with some exceptions.

Therefore, an imaging technique that could reliably and rapidly assess surgical margins would be of a great aid to limit the number of re-operations. Optical coherence tomography (OCT) and full-field optical coherence tomography (FFOCT) offer high-resolution and relatively fast assessment of pathologies. OCT has been previously investigated in a variety of tissues, such as the upper aero-digestive tract [23–26], gastrointestinal tract [27–29], and breast tissue as well as lymph nodes invasion [1], [3], [30–35]. Conventional OCT systems are not able to reliably image cellular features due to limitations in transverse imaging resolution as described previously. Full-field optical coherence tomography overcomes those limitations by acquiring images in an «en-face» plane.

The present study is designed to evaluate whether full-field OCT images can be accurately read for presence or absence of relevant features of malignancy compared to the gold standard of histology. It consists of a broad imaging survey of fixed ex-vivo breast tissues whereby images are precisely correlated with histology to provide a basis for future interpretation and in-vivo studies.

III.1.2 Material and method

Study design and imaging protocol

Tests performed were designed as pilot study to evaluate the capacity of FFOCT to perform images of fresh and fixed samples of breast tissues. Throughout the imaging process, tissues were immersed in isotonic phosphate-buffered saline to prevent dehydration. Fixed tissues were kept either in a formaldehyde solution or in a mixture of acetic acid, formaldehyde and alcohol (AFA). Imaging was performed on fixed tissues of discarded portions not needed for diagnosis. In addition, the light-CT technique of imaging has been demonstrated not to interfere with any subsequent histological or immunhistological assessment [36].

Specimen selection and preparation

Tissues were selected based on the potential presence of different diagnostic features for presentation. As previously detailed, fresh tissues show similar contrast and morphological features of malignancy and could therefore be readily compared and applied to the results presented here. A lower contrast has been seen in some cases if fresh tissues were imaged.

Tissue excisions from surgery are of irregular shape and geometry. To enable imaging of a surface comparable to histology slides (~1cm²) a special sample-holder has been developed in order to rapidly position the tissue and control the pressure applied in order to obtain a homogeneous flat

surface. The sample-holder is placed on a three-axis stage to allow rapid translation with respect to the microscope optics.

Imaging was performed through a 1 mm silica coverslip and water immersion microscope objective were immersed in an ultrasound gel (Aquasonic Clear, Parker Laboratories Inc., Fairfield, NJ, USA). Water-based gels have excellent optical properties and are commonly used in confocal microscopy as an immersion medium for objectives lens [37], [38].

Instrument

A description of the full-field compact OCT system has been detailed in the preceding chapters. In brief, a white-light halogen lamp illumination source is fibred to a beam splitter (interferometric principle of OCT). At one end, a silicon crystal mirror is cadenced by a piezoelectric stage actuator (reference arm) and the sample being imaged at the other end. A standard microscope objective (10X/0.3 numerical aperture, UMPLAN FLN, Olympus) is mounted on both extremities.

A high-speed CMOS camera is synchronized with the piezoelectric oscillations and captures each destructive or constructive interference generated by micron scale refractive index differences from the biological sample. The tungsten-halogen light source provides an effective camera response centred around 710 nm (near infrared) with a >125 nm bandwidth, thus achieving on optical section around 1.5 µm (axial resolution) and the diffraction limited lateral resolution close to 1.5 µm. At this resolution, the maximum penetration depth routinely used was around 100 µm, but only 20 to 50 µm in depth were necessary during this study.

Data analysis

In this observational study, assessment focused on qualitative image interpretation and correlation with the gold standard histology. A database of several images per sample was collected at different depths or different areas in the sample. The whole database was first reviewed, and representative normal, benign and malignant specimens were selected for further comparison with histology. Image selection was based on several factors including possible correlation with histology slides, overall image quality, and ratio of pathologic to non-pathologic specimens.

For this thesis, FFOCT images are displayed on an inverse or negative grayscale colormap (unless otherwise mentioned) with bright corresponding to low signal and black corresponding to strong signal. This type of representation is consistent with representations used in the literature for OCT images but the opposite of what is commonly used for confocal microscopy or ultrasound imaging. One would expect that either representation is equally representative. However, observations have shown that both grayscale colormap are actually complementary. In addition, a negative grayscale colormap replicates histology slides appearance whereby adipose tissue appear bright and fibrous tissue, dark.

III.1.3 Results

Figure III.1 shows the characteristic features of normal breast tissue as seen on FFOCT. (for a schematic diagram of the three main tissue areas of a female breast see figure III.2). A general morphological assessment clearly shows a mixing of adipose tissue (adipocytes) and surrounding fibrous stroma. Organized structures with well-circumscribed contours are clearly distinguishable, such as lobules and milk ducts. A characteristic tree-shape structure of a terminal duct lobular unit (TDLU) is clearly visible in the centre of the tomographic images. By inverting the grayscale map, ductal and lobular tissue appear bright due to hypo-scattering as confirmed in subsequent FFOCT images.

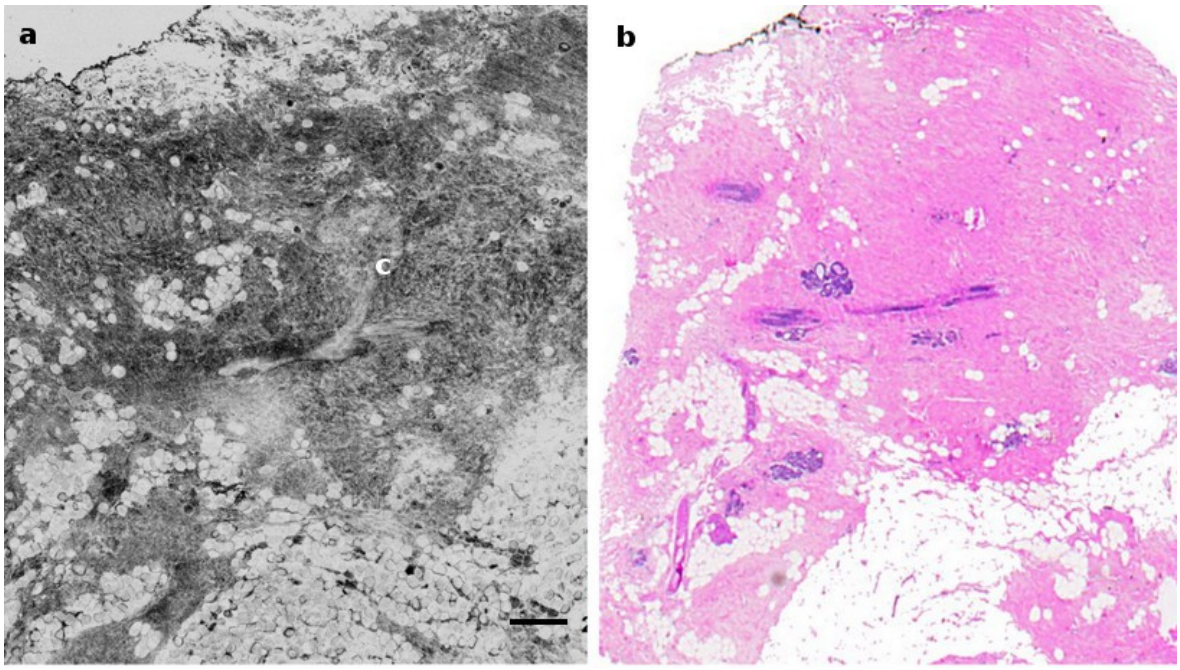

Figure III.1: FFOCT image of healthy breast tissue a) and corresponding histology slide b). A cauliflower-like structure characteristic of a terminal duct lobular unit (TDLU) can be seen in the center of the tomographic image c). The corresponding lobular structure is not visible on histology due to a probable difference of section depth or a different angle of slicing. Scale bar: 250µm.

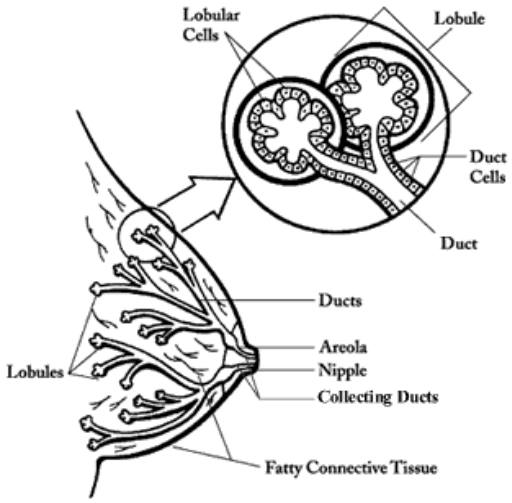

Figure III.2: Schematic of female breast tissues: mainly lobules (milk-producing glands), ducts (tubes that carry the milk from the lobules to the nipple), and stroma (fatty tissue and connective tissue surrounding the ducts and lobules, blood vessels, and lymphatic vessels. From Cancer.org

In contrast, figure III.3 shows a direct tomographic image – without look-up table inversion. Fatty tissue or adipocytes appear dark due to lower scattering and higher absorption properties compared to highly scattering surrounding structures (e.g. epithelial layers) or fibrous tissue.

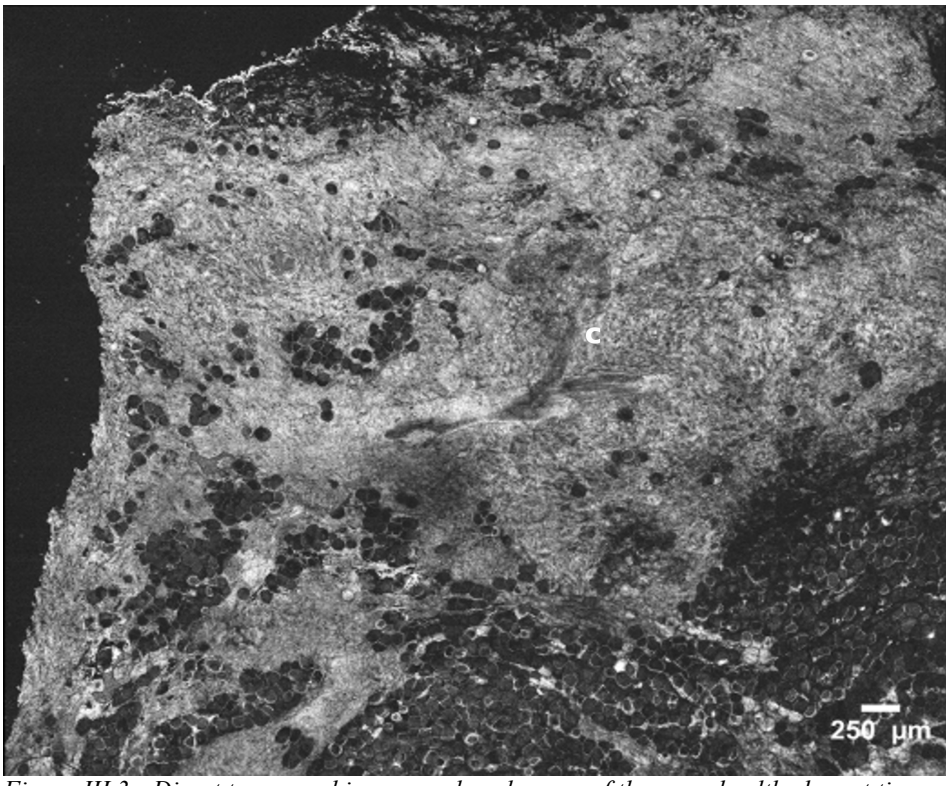

Figure III.3: Direct tomographic grayscale colormap of the same healthy breast tissue. The terminal duct lobular unit c) appears more distinctively compared to an inverse colormap. At the opposite, fatty tissue or adipocytes are dark on inverse grayscale map.

Figure III.4 presents distinct features of a ductal carcinoma in situ (DCIS) showing enlarged lobules – clusters of distended acini – and ductal structures with narrow lumen. The magnified view in figure III.5 confirms the presence of multiple distended acini (grape-like shape). In the ductal structure a narrow lumen (white area) is clearly distinguished and the remaining part of the duct is therefore packed with suspicious material. Those abnormal features (i.e. enlarged lobule and narrow duct's lumen) indicate a suspicion of malignancy.

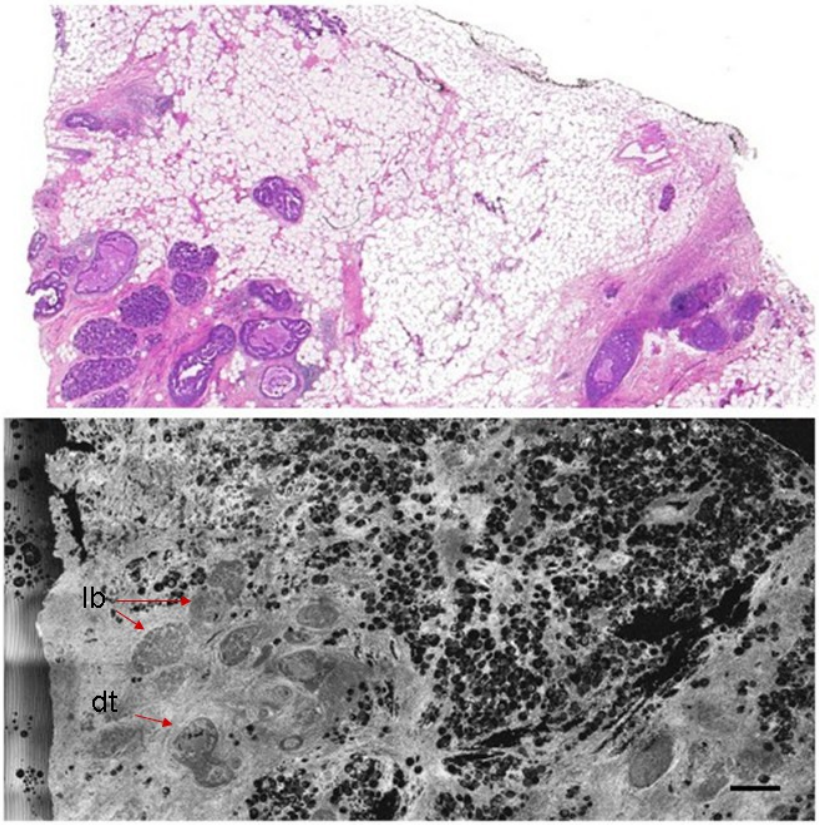

Figure III.4: ductal carcinoma in situ (DCIS). FFOCT image (bottom) along with corresponding histology (top). Enlarged lobules (clusters of distended acini) (lb) and, ducts with narrow lumen (dt) are readily distinguished. Scale bar: 250µm.

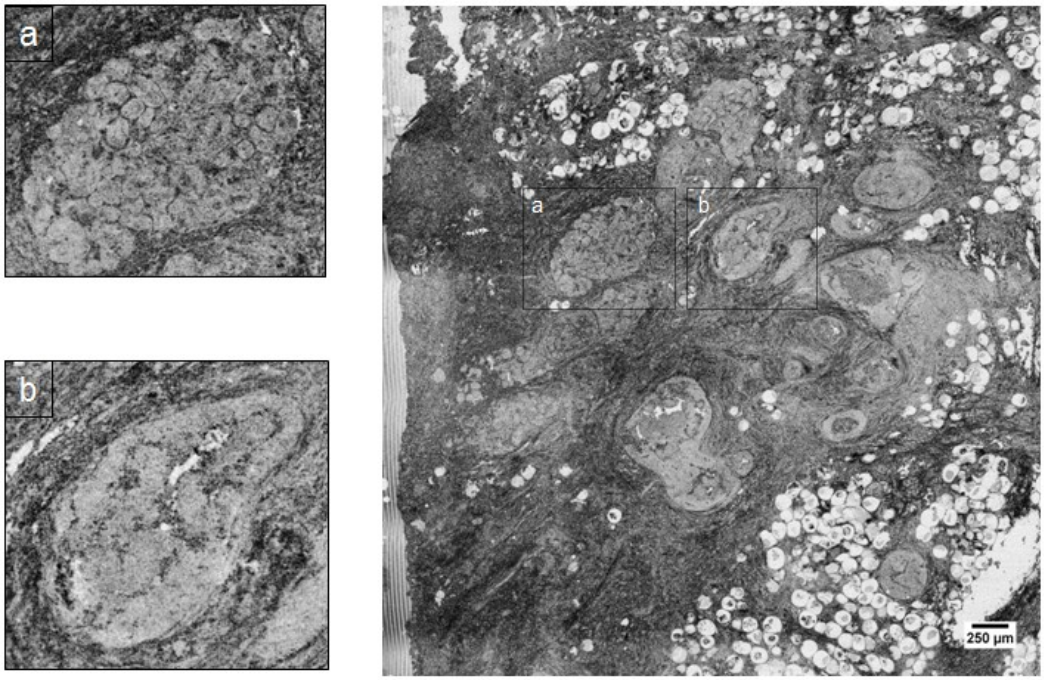

Figure III.5: zoomed view of an enlarged lobule and individual acini a) and galactophorus ducts filled by cell proliferation b).

A second example of ductal Carcinoma in situ (DCIS) is shown in figure III.6 and III.7. Lobular and ductal structures appear highly enlarged due to a proliferation of malignant cells within each structures.

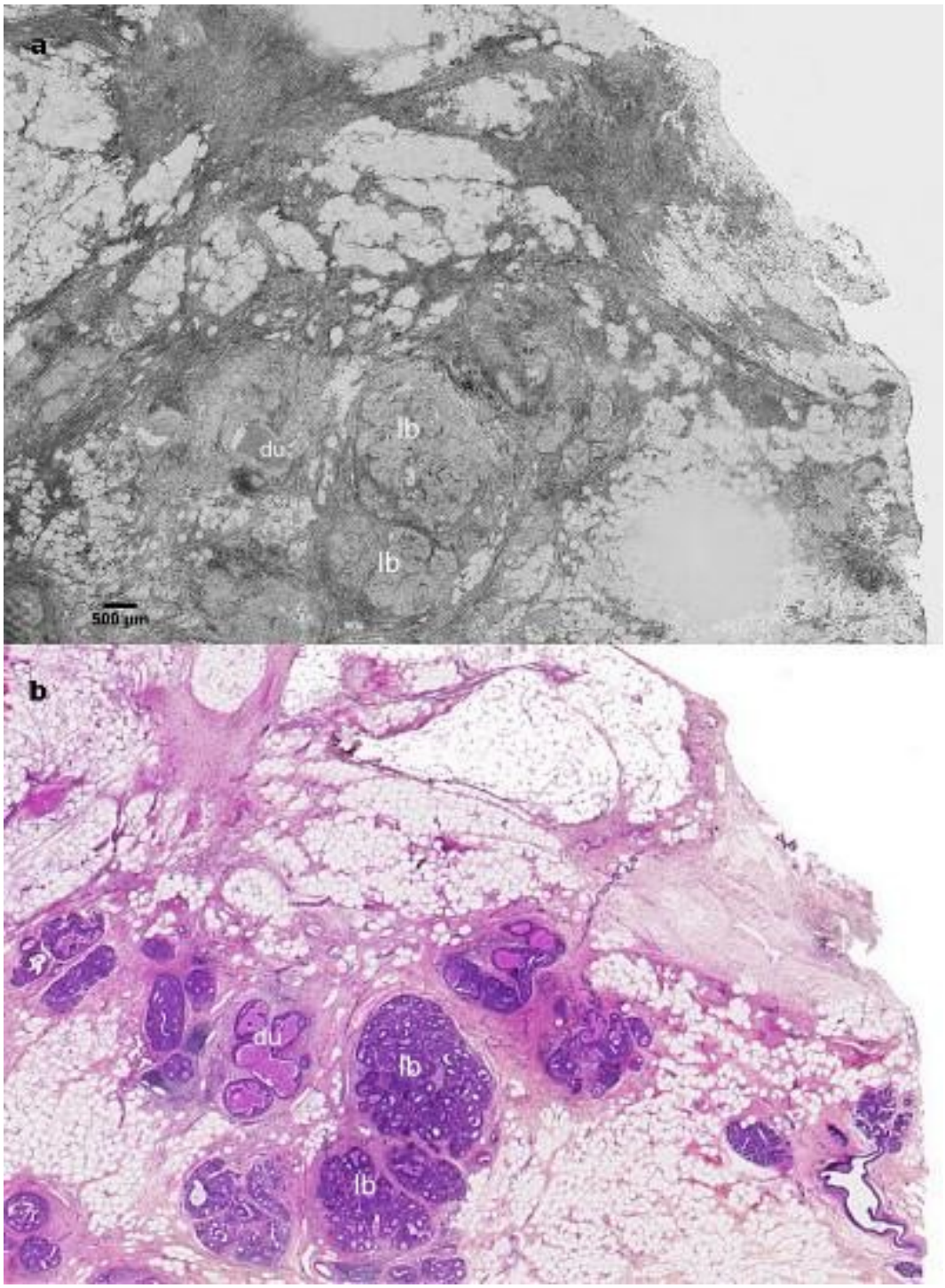

Figure III.6: Ductal Carcinoma in situ (DCIS). Tomographic image a) and corresponding histology section b). Lobular (lb) and ductal (du) structures appear highly enlarged due to a proliferation of malignant cells.

Figure III.7 shows a zoomed view on the enlarged ducts. The increase in size is an indication of abnormal cell growth. In addition, the narrow lumen, thin whitish area inside the duct is filled with suspicious material. All those criteria are converging towards a diagnosis of malignancy.

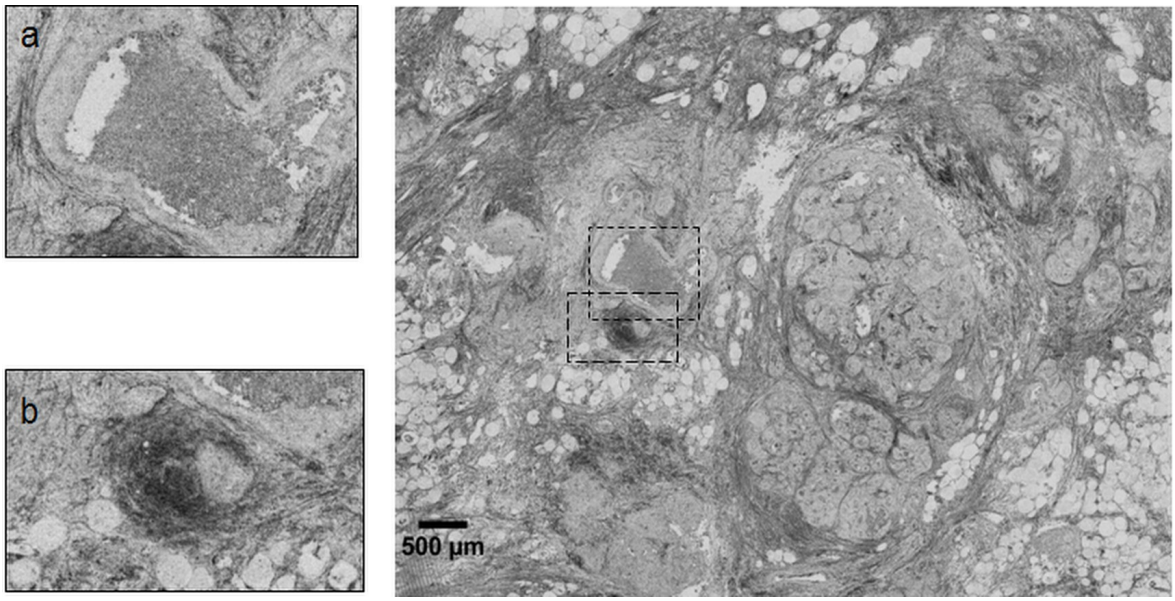

Figure III.7: zoomed view of figure III.6 showing a duct filled with suspicious material (grey area) and a narrow lumen (white area) a); and a duct filled with a possible calcification or necrosis b).

Figure III.8 presents an invasive ductal carcinoma observed in the FFOCT image. Notably the overall architecture appears clearly disorganized. Circular shape is characteristic of a nodule pushing border and is clearly visible on FFOCT imaging. Large clusters of glandular tumour cells are invading surrounding stroma with irregular borders. Adipocytes within the infiltrated stroma appear significantly reduced in size compared to larger adipose cells seen at the top left of the FFOCT image.

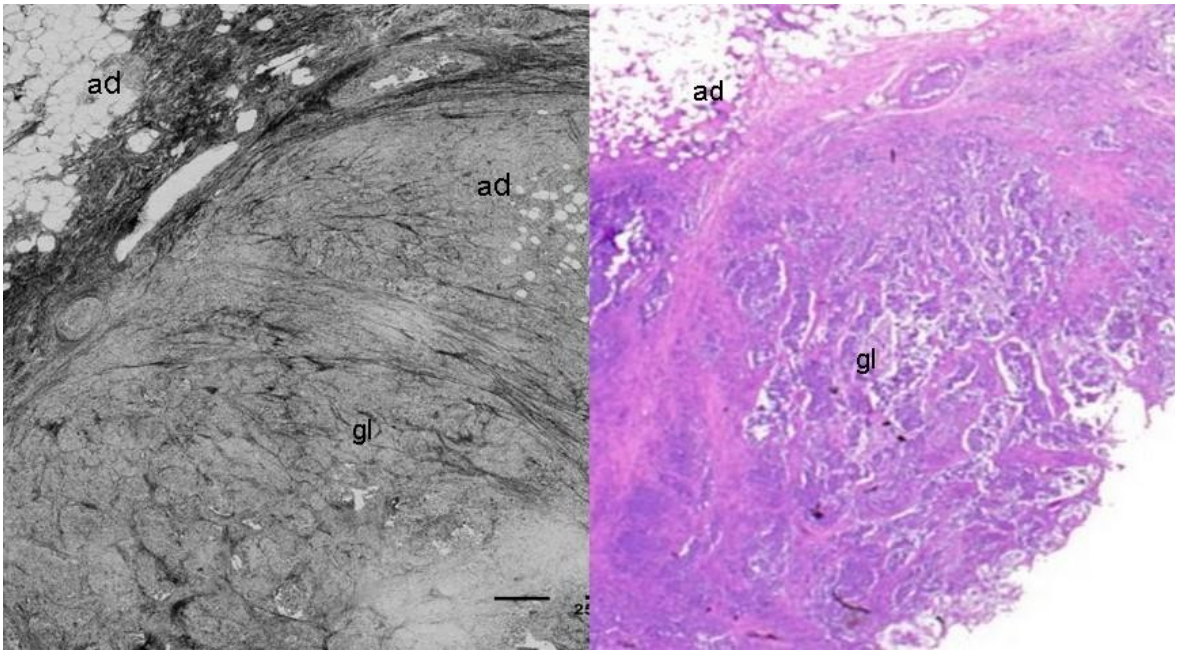

Figure III.8: Invasive breast carcinoma. FFOCT image (left) and corresponding histology (right). Adipose tissue (ad) present different sizes depending on tumor invasion. Glandular invaded fibrous tissue (gl) seen as dark purple on histology appear compressed and packed in clusters with a loss of regular shape on OCT. Bar scale: 250 µm.

A breast nipple tissue, which is not comparable to any previous tissue described as far, is shown in figure III.9. Breast nipples are composed of several layers with distinctive architectural structures. Linear structures positioned in the centre of both images are lactiferous or galactophorous ducts with surrounding epithelial layers appearing bright in contrast to the darker duct lumen (inverse grey scale map).

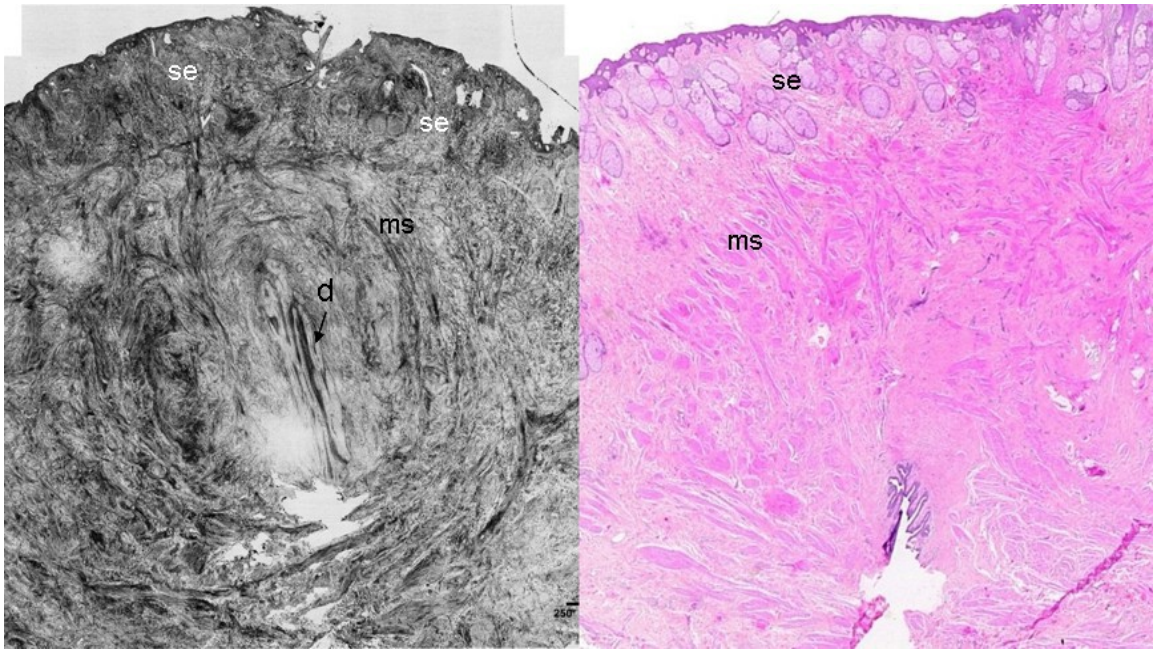

Figure III.9: Breast nipple. FFOCT image (left) along with corresponding histology (right). Distinctive features of breast nipple tissues are readily distinguishable: sebaceous glands (se); milk ducts (d), muscle fibers (ms).

At the external border of the nipple, the skin and sub-cutaneous covering appear as a thin dark layer. Underneath, sebaceous glands can be identified as round hypo-scattering glandular structures. Circular bands of muscle tissue are readily distinguished in the FFOCT image.

III.2 Core-needle biopsy study

III.2.1 Background

Needle biopsy of breast masses as alternative to open surgical biopsy is a widely performed procedure. It is recognized as highly accurate and cost-saving when tissue sampling is possible. Core-needle biopsy (CNB) or fine-needle biopsy (FNAB) are the two main methods. Difference between FNAB and CNB is needle's diameter (<0.8mm vs 2.1mm respectively). Usually if the lump is palpable, a fine-needle biopsy is sufficient in most cases. Otherwise, if there is suspicion of a solid or cloudy fluid, a core-needle biopsy is preferred under image-guidance using either stereotactic mammography or ultrasound.

Due to the size of the sample, FNA's investigation is solely done on cellular level in cytopathology[7] as no tissue structure is preserved after aspiration. Larger CNB allows a more accurate assessment because it removes a sufficient area of tissue for the pathologist to evaluate suspicious cells by maintaining surrounding tissue structure. As FNA samples are not directly comparable with FFOCT imaging due to a loss of tissue architecture after needle aspiration, we have therefore focused the comparison with core-needle biopsies in this study.

Both procedures, however, suffer from significant "*non-diagnostic sampling*" rates. While the term "non-diagnostic" has been reserved for cases where relevant material has been missed, a wider definition includes cases in which representative material has been obtained yet ambiguities remain [5].

For core-needle biopsies, non-diagnostic samples occur in 8–12% of image-guided procedures when non-palpable lesions are targeted [40–43]. Multipasses are often necessary to obtain relevant material. These difficulties lead to re-biopsies in approximately 4% of the patients who undergo percutaneous procedures [37,38]. When repeated biopsies need to be performed, it not only adds to the overall cost of diagnosis, but to the discomfort of the patient. In addition, with the growing use of highly sensitive techniques such as digital mammography and breast MRI, needle biopsies procedures performed on small non-palpable lesions is likely to rise.

III.2.2 Method and protocol

The compact FFOCT system was set up within the senology unit at Institut Curie and close to the radiology unit. Imaging was conducted within 15-25 minutes after excision on fixed tissues. No additional consent was required since FFOCT imaging was performed for research purposes on fixed tissue and the technique has been demonstrated not to interfere with subsequent histology staining. To prevent tissue degradation, samples were immersed in phosphate-buffered saline as soon as they were received for imaging. A schematic of the protocol is presented in figure III.10.

[7] *Cytopathology is generally used on samples of free cells or tissue fragments and based on DNA activity in the cell's nucleus ; in contrast to histopathology which investigates whole tissues.*

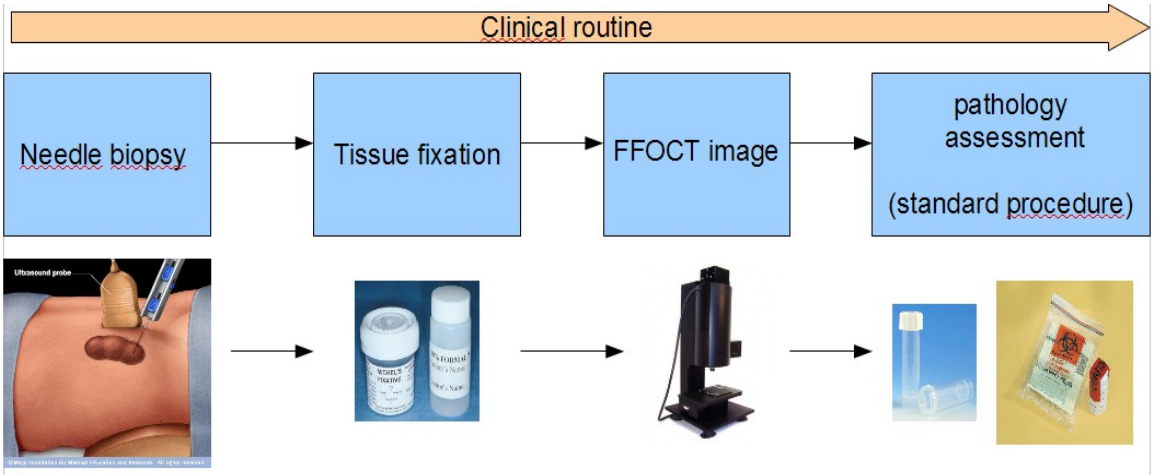

Figure III.10: Protocol flow chart for the compact OCT study under clinical conditions with core-needle biopsies.

Images were acquired with the FFOCT system through a 1mm thick coverslip (sample-holder) and objectives were immersed in ultrasound gel (Olympus, 10x/0.3 NA). 16 specimens from 13 patients were scanned and imaging was performed at two different depths. Most of biopsies were breast samples but kidney and other organs were also imaged under the same protocol (see final section).

III.2.3 Results

A benign breast lesion is shown on figure III.11. In this fibroadenoma, fibrous and fatty border is clearly visible. Lobules and acini can be differentiated from surrounding stroma as round globular structures. Before biopsy, a benign lesion was suspected; it could then confirm that the biopsy has been performed within the targeted area for further analysis.

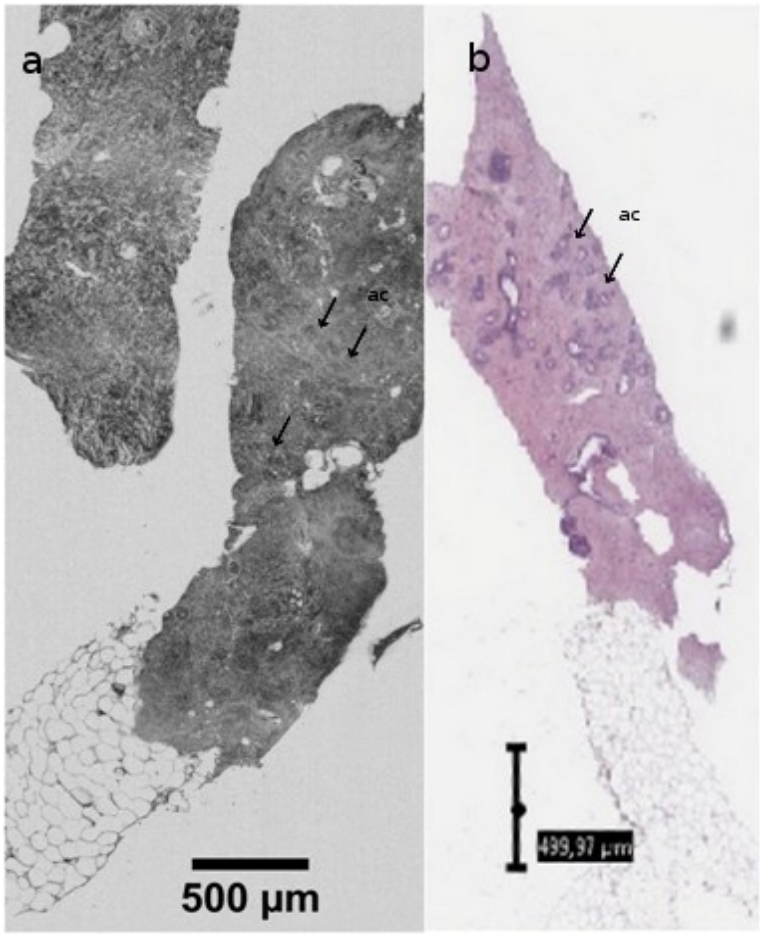

Figure III.11: FFOCT image and histology of breast fibroadenoma from a core-needle biopsy. Individual lobules' acini (ac) can be readily distinguished.

Figure III.12 demonstrates FFOCT features observed in malignant breast lesions. Although invading tumour cells are not clearly distinguished, architectural aspect appears disorganized and adipocytes reduced in diameter. Furthermore, no distinct structures are visible, which indicates suspicion of malignancy.

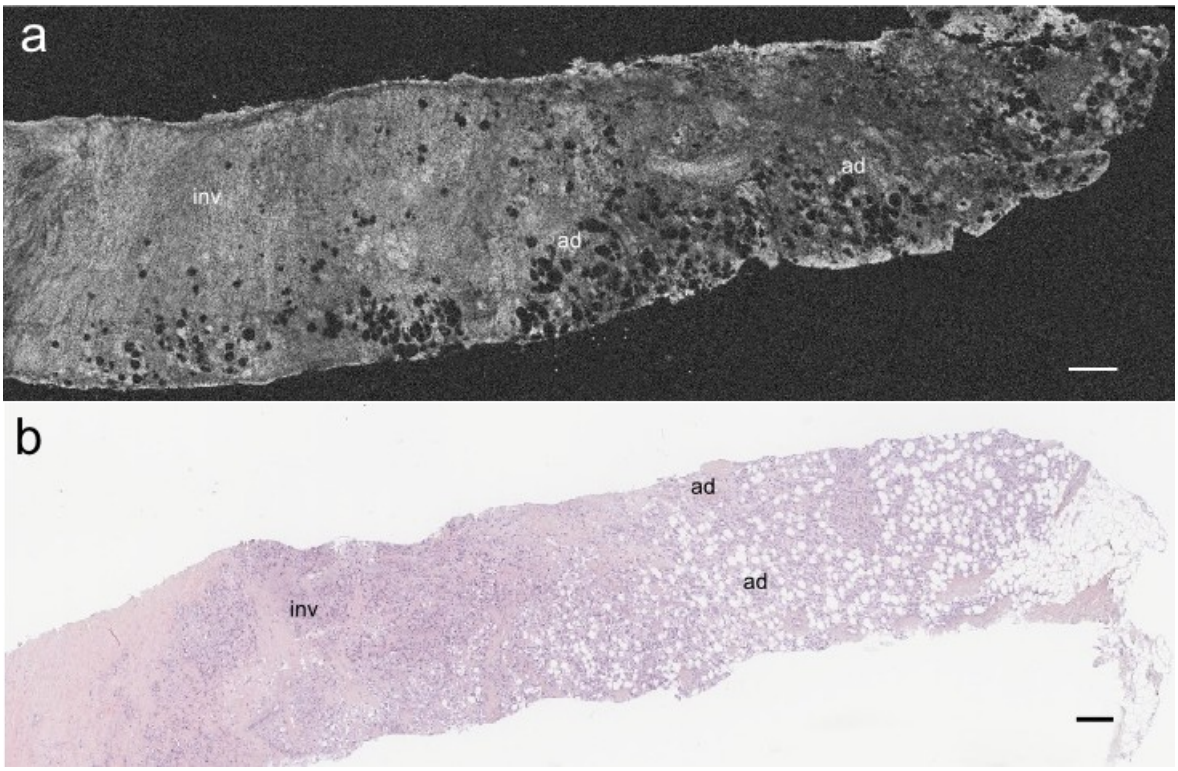

Figure III.12: Invasive breast carcinoma. FFOCT image a) and corresponding histology b). Although invading tumorous cells (inv) are not clearly distinguished, architectural aspect appears disorganized and adipocytes(ad) reduced in diameter. Furthermore, no distinct structures such as lobules or ducts are visible which indicates suspicion of malignancy. Scale bar 250µm.

Figure III.13 presents an infiltrative ductal carcinoma with large clusters of infiltrating cells appearing dark purple on histology. Although individual invasive cells are not directly seen in the tomographic image, clusters of proliferating tumour cells appear darker on OCT with stroma disorganization (wave-like appearance) and no normal mammary structures. All these elements indicate a high suspicion for malignancy.

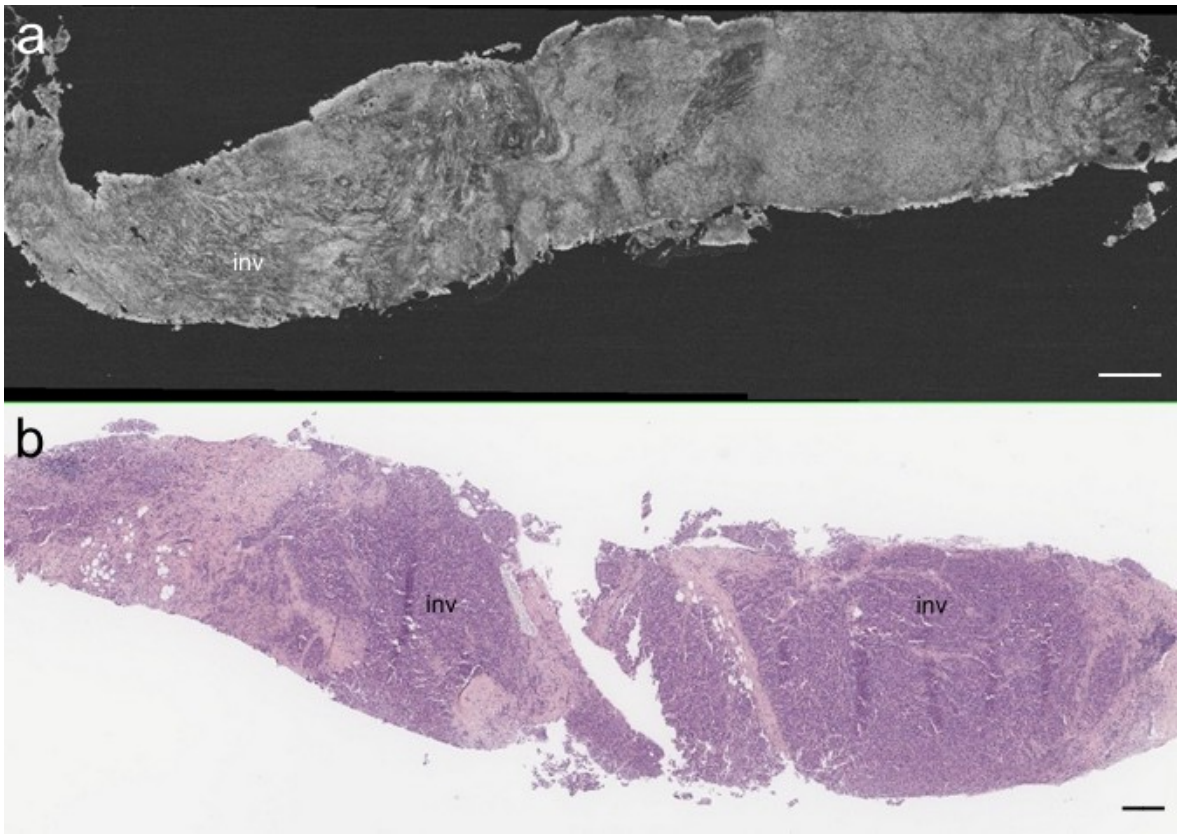

Figure III.13: core-needle biopsy of infiltrative breast carcinoma. FFOCT a) and corresponding histology b). Large clusters of infiltrating cells (inv) appear dark purple on histology and can be readily distinguished on OCT by the a wave-like appearance and disorganization of the stroma. In addition, no normal mammary structure can be found such as round-shaped lobules or ducts. Scale bar: 250µm

Other organ: kidney lesion

In figure III.14, a core-needle biopsy from a suspicious kidney shows clusters of circular and oviform cells clearly delineated. It corresponds to renal tubules as seen on histology (H&E). The magnified view allows us to differentiate individual proximal tubules characterized by round hypo-scattering lumina and hyperscattering brush borders.

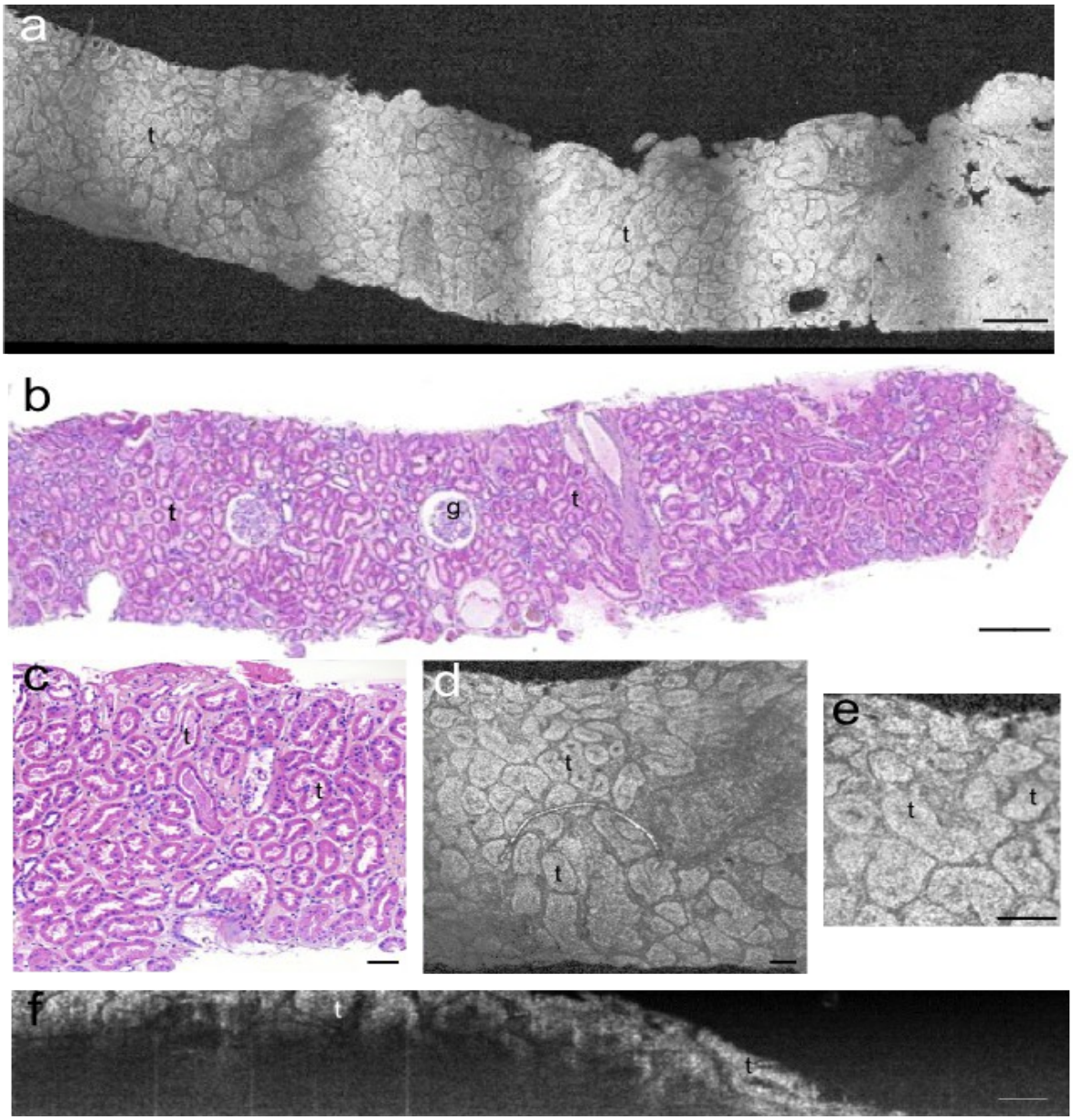

Figure III.14: FFOCT (a,d,e,f) and corresponding histological images (b,c) part of an adenomatous kidney biopsy (benign lesion). Structures shown here are normal elongated and convoluted tubules (t) readily distinguished on FFOCT images. Glomeruli (g) seen on the histological image are not present on the tomographic image at this particular position or depth. Dark bands on the FFOCT image are due to individual tiles stitching. FFOCT cross-section (f) with a depth field of view of 150µm. Individual renal tubules (t) can be distinguished up to 80-100 µm in depth. Scale bar: 250 µm (a,b) and 70 µm (c,d,e,f).

III.3 Discussion and Conclusion

In this study, full-field optical coherence tomography was investigated for ex-vivo imaging following breast resection and core-needle biopsies. The initial study assessed the capacity of FFOCT to image large zones (> 1cm²) and to accurately read for presence of relevant features of malignancy compared to the gold standard of histology. The biopsy study explored the feasibility of the compact system under clinical routine and tight time limitations.

The resolution achieved, predominantly along the x-,y-axis, enables tumour margin assessment by revealing features of malignancy; notably, loss of organized structures, change in shapes and scattering intensity variations. The reduced size of adipocytes appears as a valid indicator of tumorous cell proliferation, in particular accompanied with absence of well-delimited structures such as lobules or galactophorous ducts. Similarly, enlarged lobules and ducts tend to provide additional features of a benign lesion if cells have not invaded surrounding stroma. Such proliferation presented, for example, a wave-like appearance for the surrounding fibrous tissue and thus pointing out towards suspicion of higher grade malignancy.

As far as technical considerations are concerned, the equipment appeared to be reliable, making it suitable for clinical investigation outside the laboratory. Contrast is, however, affected by several optical factors related to the structures imaged such as multiple scattering effects and low index heterogeneities. A major advance however, compared to previous studies with optical coherence microscopy [1], [3] or confocal reflectance microscopy [44–48], is the large field of view achieved. Tiles stitching algorithm (LightCT) enabled the agglomeration of large areas of 10×10 mm² in less than 2 minutes for a field of view of 1 cm². With further increase in imaging speed towards real-time imaging, FFOCT would have the potential to serve as complement for intraoperative assessment of tumour margins during breast-conserving surgery.

One limitation of this study is the image correspondence between FFOCT and histology slides. The literature is abundant about those difficulties. Several factors can prevent exact image registration such as depth difference or a tilted slicing. For example, a few microns difference in slicing depth can already show new structures; likewise a slight angular difference during paraffin embedding or slicing generates a completely different plane. In addition, sample dehydration is performed prior to paraffin embedding. Such procedure modifies the chemical properties and therefore the architectural aspect of the specimen. Hematoxylin and eosin (H&E) images are generally slightly reduced in size compared to fresh or fixed tissue imaged with FFOCT.

The study presented here is a preliminary investigation and the relatively small sample size prevents any statistical analysis of sensitivity and specificity for malignancy. As with any other novel imaging technique, prospective studies with larger sample size would be needed to confirm these early findings. Yet, a calibrated grid of reading (e.g. specific malignancy features) has to be tested

on larger samples before attempting to measure the diagnostic efficacy for biopsies. Biopsies are by definition only a small portion of a larger specimen, only if reliable criteria can be found on larger samples then more studies would become pertinent for biopsies.

Finally, an important but lengthy phase in the introduction of a new type of images is the learning process from the medical community. In parallel to this work, it was carried out the first prospective study of FFOCT and it has shown encouraging results. The two histopathologists involved in this work (Drs. Sigal and Antoine) from two different hospitals were first shown a training set of FFOCT images with corresponding histology, followed by a “blinded” phase whereby two predefined criteria were assessed: normal vs. malignant. Results have shown a sensitivity of 93.5% (actual presence of a malignant lesion) and a specificity of 75.5% (actual absence of a malignant lesion). However, further clinical studies are essential in order to confirm those specificity and sensitivity rates. As with any novel imaging technique, these results and feedback will provide essential information regarding the potential of the technique over the long term as an aid or not for histopathologists.

References

[1] C. Zhou et al., "Integrated Optical Coherence Tomography and Microscopy for Ex Vivo Multiscale Evaluation of Human Breast Tissues.," *Cancer research*, Nov. 2010.

[2] A. Dubois, K. Grieve, G. Moneron, R. Lecaque, L. Vabre, and C. Boccara, "Ultrahigh-Resolution Full-Field Optical Coherence Tomography," *Applied Optics*, vol. 43, no. 14, p. 2874, May 2004.

[3] P.-L. Hsiung, D. R. Phatak, Y. Chen, A. D. Aguirre, J. G. Fujimoto, and J. L. Connolly, "Benign and Malignant Lesions in the Human Breast Depicted with Ultrahigh Resolution and Three-dimensional Optical Coherence Tomography1," *Radiology*, vol. 244, no. 3, pp. 865-874, 2007.

[4] P. Herz et al., "Ultrahigh resolution optical biopsy with endoscopic optical coherence tomography," *Optics Express*, vol. 12, no. 15, pp. 3532-3542, Jul. 2004.

[5] A. Jemal, R. Siegel, J. Xu, and E. Ward, "Cancer Statistics, 2010.," *CA: a cancer journal for clinicians*, p. caac.20073-, Jul. 2010.

[6] F. J. Fleming, A. D. K. Hill, E. W. Mc Dermott, A. O'Doherty, N. J. O'Higgins, and C. M. Quinn, "Intraoperative margin assessment and re-excision rate in breast conserving surgery.," *European journal of surgical oncology : the journal of the European Society of Surgical Oncology and the British Association of Surgical Oncology*, vol. 30, no. 3, pp. 233-7, Apr. 2004.

[7] G. P. Swanson, K. Rynearson, and R. Symmonds, "Significance of margins of excision on breast cancer recurrence.," *American journal of clinical oncology*, vol. 25, no. 5, pp. 438-41, Oct. 2002.

[8] C. Kunos et al., "Breast conservation surgery achieving>or=2 mm tumor-free margins results in decreased local-regional recurrence rates.," *The breast journal*, vol. 12, no. 1, pp. 28-36.

[9] A. M. Gonzalez-Angulo, F. Morales-Vasquez, and G. N. Hortobagyi, "Overview of resistance to systemic therapy in patients with breast cancer.," *Advances in experimental medicine and biology*, vol. 608, pp. 1-22, Jan. 2007.

[10] M. Z. Papa, D. Zippel, M. Koller, E. Klein, A. Chetrit, and G. B. Ari, "Positive margins of breast biopsy: is reexcision always necessary?," *Journal of surgical oncology*, vol. 70, no. 3, pp. 167-71, Mar. 1999.

[11] J. Willner, I. C. Kiricuta, and O. Kölbl, "Locoregional recurrence of breast cancer following mastectomy: always a fatal event? Results of univariate and multivariate analysis.," *International journal of radiation oncology, biology, physics*, vol. 37, no. 4, pp. 853-63, Mar. 1997.

[12] N. Cabioglu et al., "Role for intraoperative margin assessment in patients undergoing breast-conserving surgery.," *Annals of surgical oncology*, vol. 14, no. 4, pp. 1458-71, Apr. 2007.

[13] J. C. Cendán, D. Coco, and E. M. Copeland, "Accuracy of intraoperative frozen-section analysis of breast cancer lumpectomy-bed margins.," *Journal of the American College of Surgeons*, vol. 201, no. 2, pp. 194-8, Aug. 2005.

[14] R. Scheiden et al., “Accuracy of frozen section diagnoses of breast lesions after introduction of a national programme in mammographic screening,” *Histopathology*, vol. 39, no. 1, pp. 74-84, 2001.

[15] T. P. Olson, J. Harter, A. Muñoz, D. M. Mahvi, and T. Breslin, “Frozen section analysis for intraoperative margin assessment during breast-conserving surgery results in low rates of re-excision and local recurrence.,” *Annals of surgical oncology*, vol. 14, no. 10, pp. 2953-60, Oct. 2007.

[16] S. Weber, F. K. Storm, J. Stitt, and D. M. Mahvi, “The role of frozen section analysis of margins during breast conservation surgery.,” *The cancer journal from Scientific American*, vol. 3, no. 5, pp. 273-7.

[17] O. Riedl et al., “Intraoperative frozen section analysis for breast-conserving therapy in 1016 patients with breast cancer.,” *European journal of surgical oncology : the journal of the European Society of Surgical Oncology and the British Association of Surgical Oncology*, vol. 35, no. 3, pp. 264-70, Mar. 2009.

[18] C. Dener, A. Inan, M. Sen, and S. Demirci, “Interoperative frozen section for margin assessment in breast conserving energy,” *Scandinavian Journal of Surgery: SJS: Official Organ for the Finnish Surgical Society and the Scandinavian Surgical Society*, vol. 98, no. 1, pp. 34-40, 2009.

[19] T. H. NIEMANN, J. G. LUCAS, and W. L. MARSH, “To freeze or not to freeze : A comparison of methods for the handling of breast biopsies with no palpable abnormality,” *American journal of clinical pathology*, vol. 106, no. 2, pp. 225-228.

[20] S. E. Singletary, “Surgical margins in patients with early-stage breast cancer treated with breast conservation therapy,” *The American Journal of Surgery*, vol. 184, no. 5, pp. 383-393, Nov. 2002.

[21] L. Jacobs, “Positive Margins: The Challenge Continues for Breast Surgeons,” *Annals of Surgical Oncology*, vol. 15, no. 5, pp. 1271-1272, 2008.

[22] J. Q. Brown et al., “Optical assessment of tumor resection margins in the breast.,” *IEEE journal of selected topics in quantum electronics : a publication of the IEEE Lasers and Electro-optics Society*, vol. 16, no. 3, pp. 530-544, Mar. 2010.

[23] N. Ozawa, Y. Sumi, K. Shimozato, C. Chong, and T. Kurabayashi, “In vivo imaging of human labial glands using advanced optical coherence tomography,” *Oral Surgery, Oral Medicine, Oral Pathology, Oral Radiology, and Endodontology*, vol. 108, no. 3, pp. 425-429, Sep. 2009.

[24] S. G. Adie and S. A. Boppart, “Optical Coherence Tomography for Cancer Detection,” 2009, pp. 209-250.

[25] W. Jerjes et al., “Oral leukoplakia and erythroplakia subjected to optical coherence tomography: preliminary results,” *British Journal of Oral and Maxillofacial Surgery*, vol. 46, no. 7, p. e7–e7, 2008.

[26] C. S. Betz et al., “A set of optical techniques for improving the diagnosis of early upper aerodigestive tract cancer,” *Medical Laser Application*, vol. 23, no. 4, pp. 175–185, 2008.

[27] G. J. Tearney, M. E. Brezinski, J. F. Southern, B. E. Bouma, S. A. Boppart, and J. G. Fujimoto, “Optical biopsy in human pancreatobiliary tissue using optical coherence tomography.,” *Digestive diseases and sciences*, vol. 43, no. 6, pp. 1193-9, Jun. 1998.

[28] Y. Chen et al., “Ultrahigh resolution optical coherence tomography of Barrett’s esophagus: preliminary descriptive clinical study correlating images with histology.,” *Endoscopy*, vol. 39, no. 7, pp. 599-605, Jul. 2007.

[29] “Optical biopsy in human gastrointestinal tissue us... [Am J Gastroenterol. 1997] - PubMed result.” [Online]. Available: http://www.ncbi.nlm.nih.gov/pubmed/9382040. [Accessed: 27-May-2011].

[30] A. M. Zysk and S. A. Boppart, “Computational methods for analysis of human breast tumor tissue in optical coherence tomography images.,” *Journal of biomedical optics*, vol. 11, no. 5, p. 054015.

[31] N. V. Iftimia, M. Mujat, T. Ustun, R. D. Ferguson, V. Danthu, and D. X. Hammer, “Spectral-domain low coherence interferometry/optical coherence tomography system for fine needle breast biopsy guidance.,” *The Review of scientific instruments*, vol. 80, no. 2, p. 024302, Mar. 2009.

[32] W. Luo et al., “Optical biopsy of lymph node morphology using optical coherence tomography,” *Technology in Cancer Research & Treatment*, vol. 4, no. 5, pp. 539-548, Oct. 2005.

[33] A. M. Zysk, E. J. Chaney, and S. A. Boppart, “Refractive index of carcinogen-induced rat mammary tumours,” *Physics in Medicine and Biology*, vol. 51, no. 9, pp. 2165-2177, 2006.

[34] F. T. Nguyen et al., “Intraoperative Evaluation of Breast Tumor Margins with Optical Coherence Tomography,” *Cancer Res*, vol. 69, no. 22, pp. 8790-8796, Nov. 2009.

[35] S. Boppart, W. Luo, D. Marks, and K. Singletary, “Optical Coherence Tomography: Feasibility for Basic Research and Image-guided Surgery of Breast Cancer,” *Breast Cancer Research and Treatment*, vol. 84, no. 2, pp. 85-97, Mar. 2004.

[36] O. Assayag, M. Antoine, A. Burcheri, and C. Boccara, “BREAST TISSUE IMAGING WITH LIGHT COMPUTED TOMOGRAPHY (Light- CT TM),” *Methods*, pp. 75020-75020.

[37] A. Scope et al., “In vivo reflectance confocal microscopy of shave biopsy wounds: feasibility of intra-operative mapping of cancer margins.,” *The British journal of dermatology*, Sep. 2010.

[38] D. S. Gareau et al., “Confocal mosaicing microscopy in skin excisions: a demonstration of rapid surgical pathology,” *Journal of microscopy*, vol. 233, no. 1, pp. 149-159, Jan. 2009.

[39] W. A. Berg, “When is core breast biopsy or fine-needle aspiration not enough?,” *Radiology*, vol. 198, no. 2, pp. 313-5, Feb. 1996.

[40] A. Vega Bolivar, E. Ortega García, and F. Garijo Ayensa, “Stereotaxic core needle aspiration biopsy with multiple passes in nonpalpable breast lesions.,” *Acta radiologica (Stockholm, Sweden : 1987)*, vol. 39, no. 4, pp. 389-94, Jul. 1998.

[41] C. Wiratkapun, B. Wibulpholprasert, S. Wongwaisayawan, and K. Pulpinyo, “Nondiagnostic core needle biopsy of the breast under imaging guidance: result of rebiopsy.,” *Journal of the Medical Association of Thailand = Chotmaihet thangphaet*, vol. 88, no. 3, pp. 350-7, Mar. 2005.

[42] D. D. Dershaw, E. A. Morris, L. Liberman, and A. F. Abramson, “Nondiagnostic stereotaxic core breast biopsy: results of rebiopsy.,” *Radiology*, vol. 198, no. 2, pp. 323-5, Feb. 1996.

[43] R. M. Pijnappel et al., “Diagnostic accuracy for different strategies of image-guided breast intervention in cases of nonpalpable breast lesions.,” *British journal of cancer*, vol. 90, no. 3, pp. 595-600, Feb. 2004.

[44] A. Parrish, E. Halama, M. T. Tilli, M. Freedman, and P. A. Furth, “Reflectance confocal microscopy for characterization of mammary ductal structures and development of neoplasia in genetically engineered mouse models of breast cancer.,” *Journal of biomedical optics*, vol. 10, no. 5, p. 051602, Jan. 2005.

[45] M. T. Tilli et al., “Real-time imaging and characterization of human breast tissue by reflectance confocal microscopy.,” *Journal of biomedical optics*, vol. 12, no. 5, p. 051901.

[46] M. T. Tilli et al., “Real-time imaging and characterization of human breast tissue by reflectance confocal microscopy.,” *Journal of biomedical optics*, vol. 12, no. 5, p. 051901, 2007.

[47] L. Schiffhauer, J. N. Boger, T. Bonfiglio, J. Zavislan, M. Zuley, and C. Fox, “Confocal Microscopy of Unfixed Breast Needle Core Biopsies: A Comparison to Fixed and Stained Sections,” *BMC Cancer*, vol. 9, no. 1, p. 265, 2009.

[48] M. T. Tilli, A. R. Parrish, I. Cotarla, L. P. Jones, M. D. Johnson, and P. A. Furth, “Comparison of mouse mammary gland imaging techniques and applications: reflectance confocal microscopy, GFP imaging, and ultrasound.,” *BMC cancer*, vol. 8, p. 21, Jan. 2008.

Chapter IV. Contrast enhancement strategies: assessment and validation

Traditional histology or intraoperative frozen section provide colour maps of tissues based on their chemical or biological properties. Obtaining a similar type of mapping based on the optical or elastic properties of a tissue would complement the FFOCT image without having to alter tissue DNA or molecular content. This approach would prove valuable for subsequent immunohistochemical staining or targeted biobanking; notably with the advent of personalized medicine and genomic analysis [1–3].

In this chapter, the diagnostic feasibility, validity and limits of optical and elastic mapping is examined. The first section investigates a contrast enhancement method based on attenuation coefficients of large sample areas and in the second part, a proof of concept of optical elastography in ex-vivo breast tissues is presented.

IV.1 Assessment of mapping optical attenuation coefficients in breast tissues.

IV.1.1 Context and background

For histopathologists, tissue specific coloration constitutes the first visual assessment tool along with tissue architecture. This step is generally performed at low magnification (4X objectives). The examination of cell internal structures (e.g. nuclei shapes or nucleus to cytoplasm ratio) only comes as a confirmation step in the diagnostic process. A professor of histology interviewed during this work, confidently stated that 90% of pathology assessment could be performed at low magnification. It thus highlights the importance of tissue coloration and architecture in any diagnostic process. Since the early 90's, a variety of optical techniques have been tested in order to

extract the optical properties of tissues based on light propagation models. The goal was to measure the attenuation of the reflected signal in order to provide a diagnostic information about about the severity of tumour invasion.

Those techniques were mainly involving solutions to the radiative transfer equation [4] using diffusion theory approximations [5] and Monte Carlo simulations for describing light propagation in biological tissues [6–10]. Based on those models, Cheong et al. have compiled reference tables for attenuation coefficients for a large number of animal and human tissues. Optical properties measured for similar tissues show a wide variation of results that can be attributed to the different experimental methods employed. Major differences lies within tissue preparation, optical and experimental technique, theoretical model and data post-processing methods used [11].One major advantage of OCT is that optical parameters can directly be extracted from clinical specimens either ex-vivo or in-vivo.

The first attenuation measurements based on OCT data were demonstrated by Levitz et al on ex-vivo tissues by comparing normal and atherosclerotic human aortic samples [12]. Attenuation coefficients compared favourably with the theoretical model used, which takes into account multiple scattering effects.

Clark et al. at MD Anderson Cancer centre, compared the optical properties to distinguish normal from neoplastic oral mucosa [13]. Although some trends can be extracted, a wide variation in scattering coefficients was necessarily present. This difficulty can be addressed by averaging over a selected region within the en face plane (x-,y- axis). However such hand picking can lead to further ambiguity for a widespread use of this approach.

The issue has since been addressed by two groups that obtained a full “en-face” map of the attenuation coefficients. They have spatially mapped the entire specimen in an “en-face” view to generate an attenuation cartography based on the scattering properties over a 3-dimensional section by fitting the slope of the line of best fit. Maclaughlin et al. directly applied an attenuation extraction method and algorithm onto ex-vivo breast lymph nodes with a traditional swept source OCT model. They estimated tissue malignancy or cluster of metastatic cells based on attenuation coefficients extracted over a depth of 2 mm. They found that surrounding healthy stroma tissue appeared highly scattering compared to areas of cancerous cells. Malignant areas were found to have higher attenuation coefficients compared to residual non-involved area of the lymph cortex [14].

Recently, Tomlins et al. used a similar technique to characterize the severity of oral epithelial dysplasia with a commercially available swept source OCT model (Michelsons Diagnostics). The method termed scattering attenuation microscopy (SAM) provides an “en-face” view of attenuation coefficients. It was shown that mild/normal oral epithelial tissues display a characteristic Gaussian like distribution of values with a peak centred differently than for moderate/severe regions. And as stated, consistency in results among samples and patients seems to further confirm that attenuation coefficients were dominated by tissue heterogeneity rather than measurement noise. However, a substantial limitation of the study is that the signal magnitude

appears to highly fluctuate even in a logarithmic scale and the "average" slope or best fit appears hardly representative as shown on figure IV.1.

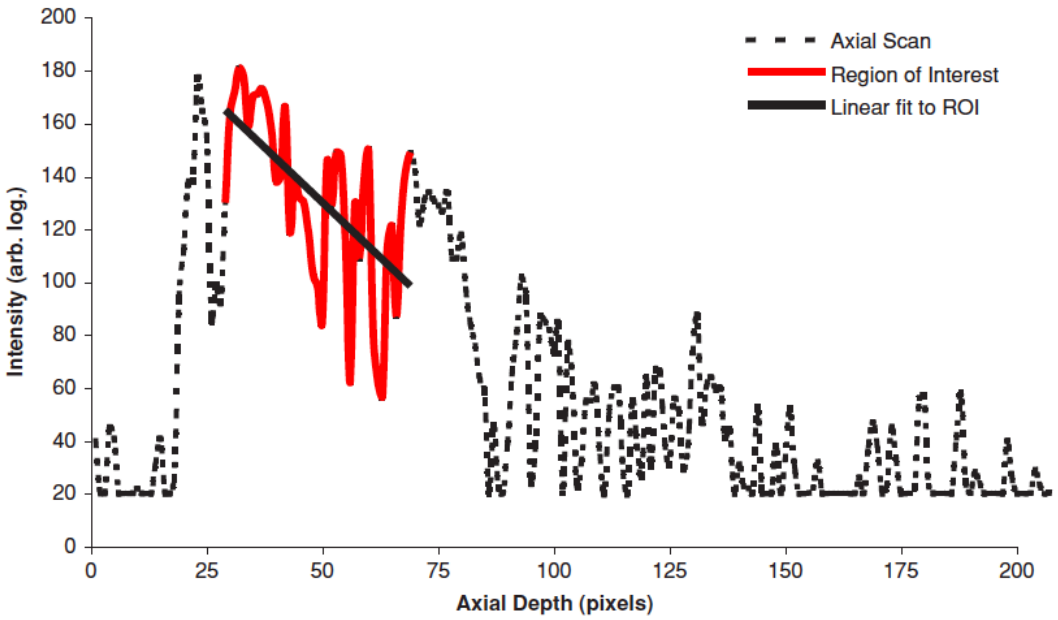

Figure IV.1: Described in this reference [52] as a typical A-scan, including the region of interest (red solid line), to which a straight line is fitted to estimate the scattering gradient μ. The slope of linear fit could potentially be quite different hence leading to a completely distinct estimate of its scattering gradient, μ. Published in the Journal of Biomedical Optics.

In the present feasibility study, measurements were limited to depths up to 100 μm, typically where multiple scattering starts to dominate for highly anisotropic tissues such as the breast [15], [16]. The aim of such an approach is to assess the feasibility and diagnostic validity of mapping optical attenuation coefficients in normal, benign and malignant breast tissues at shallow depths compared to traditional OCT.

IV.1.2 Material and methods

Specimen selection and instrument.

Tissues were selected based on the potential presence of diagnostic features for inclusion in the study and scanned at two different depths (e.g. healthy, benign or malignant tissue). The image acquisition was performed through a 1 mm silica coverslip immersed in water-based ultrasound gel. 7 different structures representing 41 cellular zones were examined.

A description of the full-field compact OCT system has been previously detailed. In brief, a white-light halogen lamp illumination source is fibred to a beam splitter (i.e. low coherence interferometry). At one end, a silicon crystal mirror is cadenced by a piezoelectric stage actuator

(reference arm) and the sample being imaged at the other end. A standard microscope objective (10X/0.3 NA, *UMPLAN FLN, Olympus)* is mounted on both extremities. A high-speed CMOS camera is synchronized with the piezoelectric oscillations and captures each destructive or constructive interference generated by micron scale refractive index differences and scattering from the probed volume of coherence within the specimen. The tungsten halogen light source provides a 160 nm bandwidth centred around 710 nm which determines the optical section achieved. Thus the axial and diffraction limited lateral resolution are approximately similar around 1.5 µm. In addition, the maximum penetration depth routinely used was around 100 µm, but only 20 to 50 µm in depth were necessary for measuring the attenuation coefficients over a homogeneous cross section.

Scattering coefficient analysis

The interaction of light with biological tissues is dominated by the optical properties of large scattering sites within the biological specimen (e.g. cell nuclei or mitochondria). In the single-scattering model of light propagation, it is assumed that only one back-scattering event occurs (i.e. only ballistic photons are collected). The scattering cross section is affected by the size and shape of each scattering centres and this gives rise to attenuation changes of light propagation.

Several studies have used this model to measure the optical attenuation either ex-vivo [17–21] or in-vivo [22–24]. In the OCT literature, this model is the most widely employed in comparison to multiple scattering models and was used in this work for its simplicity and robustness. The exponential attenuation of the OCT signal can therefore be modelled in accordance with the Beer-Lambert law. The returning power fraction or signal intensity $I_{(z)}$ at a given depth z can be expressed as follows:

$$I_{(z)} = I_0 \mathrm{e}^{-\mu_{(\lambda)} z} \tag{8}$$

where I_0 is the incident light's intensity and I the reflected intensity. In this experiment, the measured attenuation coefficient μ_t has therefore been extracted with the following equation:

$$\mu_t = \frac{[\ln(I_1) - \ln(I_2)]}{(z_1 - z_2)} \tag{9}$$

whereby I_1 et I_2 are the signal intensity from the two different depths z_1 and z_2 (with $z_1 > z_2$), and μ_t is the observed attenuation coefficient of the tissue. A factor of 2 should appear in equation (8) since the pathlength has to be doubled to take into account the return path of light from the tissue to the detector. However, the amplitude signal not the intensity is being measured with the equipments and thus the overall signal actually follows the decay indicated in (8) with $I_{(z)}$ representing the recorded signal.

In the experiment, $\mu_{(\lambda)}$ is the attenuation coefficient, which is the sum of the absorption and scattering coefficients. However, measurements were taken in the near-infrared region around 700 nm ($\Delta\lambda$=125 nm), and scattering coefficient is significantly higher than the absorption coefficient for

biological tissues at this wavelength. The attenuation coefficient was therefore assumed to equal the scattering coefficient.

Image acquisition and processing

Images at two different depth-of-focus were saved as floating point numbers with Image J software and translated into 32-bit format after subtraction of the two images and before applying a 10log format scale. A linear coefficient was applied onto the resulting image in order to display a map of mean free path values (l) or the attenuation coefficient, μ in mm^{-1}.

Additional post-processing was performed on each map by applying convolution presets with a Gaussian function for smoothing. A sigma of 5 for the Gaussian standard deviation was applied. Brightness and contrast were enhanced by an automatic updating of the look-up table (LUT), without altering pixel values.

IV.1.3 Results

Out of the 41 different cellular areas within the 7 specimens analysed, no statistically significant differences were found between healthy and benign or malignant breast tissues. A similar finding was found by another researcher in the laboratory on a different set of specimens. Attenuation coefficients were in the range of 10 to 30 $mm^{-1,}$ however the results did not show any statistically significant variation within each structure examined (e.g. duct, lobule, surrounding fibrous tissue,...) and possible explanations are discussed below.

One exception worth noticing is the attenuation difference between normal and malignant breast lobules (the terminal gland responsible for milk secretion). Lobules exhibit a more homogeneous packed structure than other regions and an increase in the average attenuation coefficient as the epithelial surface progresses from healthy to lobular carcinoma (i.e. tumorous cell invasion within the lobule) as shown on figure IV.2.

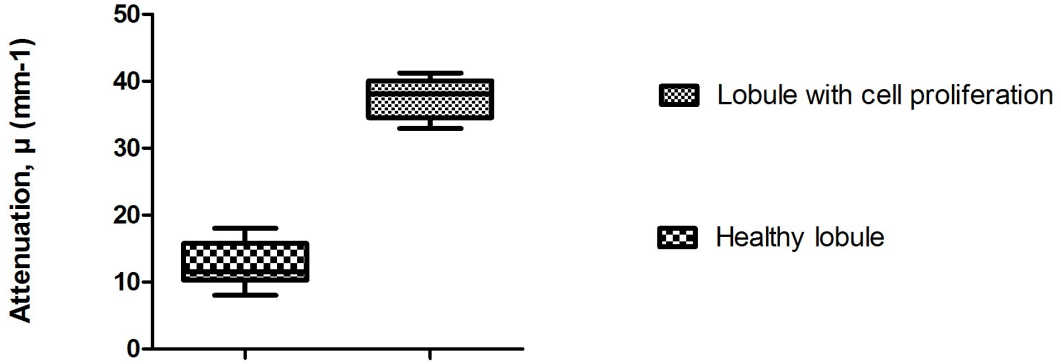

Figure IV.2: Comparison of attenuation coefficients between healthy and invaded breast lobule (carcinoma in situ); p-value <0.5 using a one-sided student t-test.

The mean attenuation coefficient from normal lobules was 12±3.5 mm^{-1} compared to 37±3.5 mm^{-1} for a specimen with intraductal invasion (p-value <0.5).

However, a major result of this investigation is the high heterogeneity of tissues over a range of only a few microns as illustrated by figure IV.3.

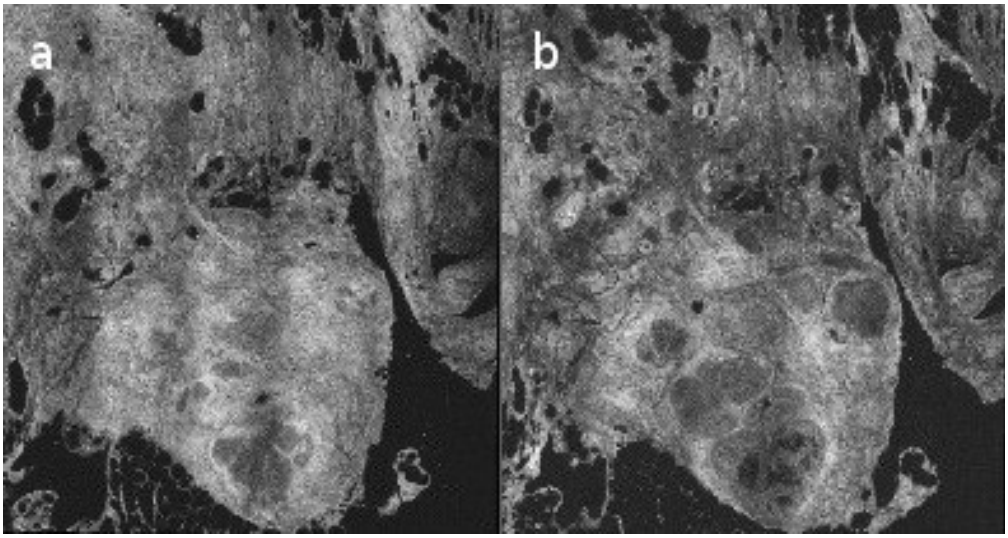

Figure IV.3: Breast ductal hyperplasia at 10 and 25 µm; images a) and b), respectively.

Numerous new epithelial structures appear over a range of 15 µm in depth. More importantly, those structures show a high variation of mean attenuation coefficients (e.g. highly scattering fibrous stroma replaced by highly attenuating lobules). Over larger penetration depths, there are therefore increased chances to come across similar tissue heterogeneity when the analysis is performed with a micron-scale resolution as it is the case for FFOCT.

IV.1.4 Discussion

These results illustrate the ability of high resolution full-field OCT to extract additional information without any particular tissue preparation or staining. The results are in line with the range of attenuation coefficients found in the literature for human breast tissues [25]. However, no clear difference in attenuation coefficients has been found between normal and malignant structures. The only statistically significant increase in attenuation found was in a lobular carcinoma in situ (LCIS) but this finding is highly undermined by the rare occurrence of this type of lesion [26] and the limited sample number used in this study.

In addition, the methodology employed is based on significant assumptions. Measurements assume that only a single structure or tissue type is sampled over the scanning range. However, these results highlights the limits of this hypothesis. The high resolution imaging method allowed to pinpoint the important heterogeneity with a range of a few microns. For example, a highly scattering structure at a given depth can be averaged by a less scattering structure (e.g. adipocytes or tumorous cells).

Previous studies on cervical tissues suggested that single layer models that assume tissue is homogeneous are not well suited to describe light propagation in vivo because of the large difference in scattering between epithelium and stroma [27]. Results reported here further emphasize this point by identifying potential separate layers within a few microns and with different scattering properties.

A recent study on ex-vivo urothelial tissues also confirmed this conclusion. Cauberg et al. used a conventional OCT to scan over 1-2 mm bladder biopsies but could not determine a quantitative criteria to differentiate healthy tissues from urothelial carcinoma. They nonetheless attributed those results to the experimental conditions of ex-vivo tissue scanning; yet mentioning that this hypothesis would only be confirmed with the future in-vivo study planned [28]

McLaughlin et al. have suggested that image segmentation techniques would be required to identify regions of homogeneous tissue so as to separately calculate the attenuation coefficient. A similar issue exist in medical imaging such as MRI, PET or CT scans and is known as partial volume effect (PVE), though mostly resolved by increasing the sectioning resolution. In OCT or FFOCT, a similar approach would not deem appropriate as most systems are constantly scanning at the maximum axial and lateral resolution possible.

Moreover, measurements assume that backscattered light is solely based on ballistic photons, ignoring multiple scattering effects from surrounding tissues. More sophisticated models have proposed to include the shower curtain effect or the heterogeneity of size, shape and density of the scatterers [29], [30]. However, these models seem to have a seldom implementation in the last decade.

Finally, the small number of patients included in the study is evidently an important limiting factor of these results. Nonetheless, the trend seems to show the limits of this approach to extract valuable information for the clinician

The attempt to accurately model micro-anatomical features of tissues based on their scattering properties is an appealing idea since it could be readily implemented for in-vivo measurements. The downside is its lack of solid criteria to accurately identify a potentially malignant area or at least a suspicion of abnormal structures. Those shortcomings are mainly due to the similarity in optical properties among inherently diverse tissues and distant by a few microns.

Recent studies have nonetheless used the same methodology to extract a colourful map for human axillary lymph nodes and obtained contrast enhancements. The essential criteria is less the feasibility of such approach but its sensitivity and specificity in comparison to the gold standard of histology [31].

IV.2 Feasibility of an experimental setup to measure the static elastic properties of a breast tissue.

IV.2.1 Background and context.

Faced with the shortcomings of the attenuation map approach, alternative quantitative diagnostic criteria were explored. Over the past two decades, research on the elastic properties of tissue as contrast mechanism has received increasing interest for medical applications [32–35]; and is now know as elastography. Originally ultrasounds and MRI have been the method of choice to understand and quantify the mechanical properties of tissues. Its implementation has been a success and several commercial systems are now available (e.g. Fibroscan® (Echosens), Aixplorer® (Supersonic Imagine) or Arfi® (Siemens)).

More recently, the optical variant or optical elastography has been tested with OCT as its underlying optical imaging modality [36–38]. Despite improvement in spatial resolution achieved by MRI (<1 mm) or high-frequency ultrasound (~50-70 µm)[39], the gain in resolution offered by OCT (3-15 µm) or high-resolution OCT (~1 µm) provide new capabilities to measure elastic changes at the cellular level. The goal is to quantify micron-scale strain induced inside a tissue by applying a load or stress externally. This approach has been investigated for medical applications, such as skin stiffness [36], [40–42], atherosclerosis plaque [43–45]and breast tissues [46]. The underlying hypothesis is that tissue stiffness is strongly related to pathological change.

FFOCT takes advantage of a broadband light source and a short coherence length to track the relative motion of individual internal structures of a tissue under an external load. The micron-scale deformation or relative strain distribution of individual tissue elements can recorded before and after applying an external force. The traditional assumption in elastography of biological tissues is that the resulting map is equivalent to a modulus image. By applying a known force or stress and by extracting the strain from the OCT map, then the Young's modulus can be estimated. It requires

to consider the biological tissue as an incompressible, homogeneous, and isotropic linear elastic material. If a uniform stress is applied in the axial direction, the local stress then becomes equivalent to the applied stress (and constant throughout the sample). For a homogeneous sample, one can therefore extract the Young's modulus following this linear relationship:

$$E = \frac{\sigma}{\varepsilon}, \tag{10}$$

where E is the Young's modulus, σ the stress, and ε the strain. Since a quasi-static measurement is performed as opposed to a dynamic or harmonic approach, the strain image is usually considered to approximate the modulus distribution. This simple, direct linear elastic and isotropic methodology is generally favoured since elasticity values can be assigned to individual structures within the tissue and a map can be readily generated with fairly simple image processing.

However, most biological soft tissue do not exhibit a truly homogeneous elastic response due to the heterogeneity of the individual structures targeted which exhibit anisotropic, viscoelastic and incompressible properties. So several conditions must be fulfilled so that linear elasticity or Hooke's law can be a valid approximation. The non-linearity of the elastic constants can be neglected under the assumptions that a small deformation is applied (<1%) [47]. In addition, the tissue is assumed to be uniform, linearly elastic, isotropic and subject to a constant stress field. The strain map can then reflect the relative measure of elasticity distribution, whereby a small displacement implies a rigid tissue and a large strain a more compliant (soft) tissue [48].

In this experiment, the aim was to assess whether a quasi-static strain mapping is achievable while maintaining the micron-scale resolution of FFOCT. A doctoral project has subsequently been initiated to further expand this preliminary study.

IV.2.2 Experimental setup

In order to obtain a strain map of displacement, a rotating sample holder inducing gradual loads was mounted on a customized platform directly onto the FFOCT system. A schematic diagram of the system is presented on figure IV.4.

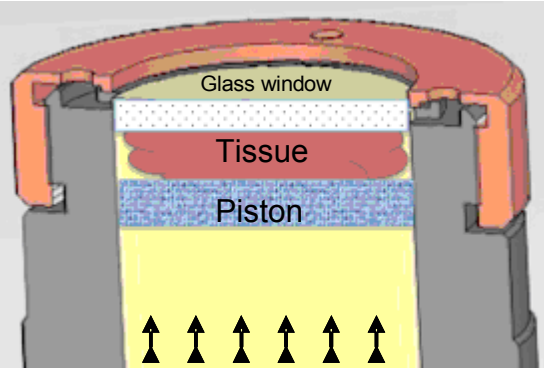

Figure IV.4: sample-holder schematic diagram. Arrows indicate direction of load. Pressure could also be applied from the top to bottom (glass window).

The specimen was brought into contact with the glass window before applying a uni-axial compressive loading. With the sample-holder used, pressure could be applied either from the same side as the illumination beam (top) or from the bottom side.

cross-correlation-based method

Image stacks were acquired before and after uni-axial load. From the resultant deformation pattern, strain maps are obtained by numerically differentiating the axial displacement component assuming the applied stress was uniform. A particle image velocimetry program (PIV) developed in Matlab® was used (PIVLab [49])to generate strain maps. As previously described strain image is considered to approximate the modulus distribution for individual structures in the tissue.

A 2-D cross-correlation coefficient can be determined by examining pixel-intensity array subsets on two subsequent corresponding images. A crucial aspect is the size of the correlation window and the interrogation area chosen in order to extract a 2-D correlation. This aspect will be discussed further in the discussion section. In the result presented, the interrogation window was 5 μm² with a displacement of approximately 9.5 μm.

IV.2.3 Results

These are only sample results to show the feasibility of the methodology. As stated earlier, since the beginning of this work, a full-time thesis project has been initiated to fully explore the addition of an elasticity map.

The specimen is a breast fibroadenoma which is commonly considered a benign lesion formed of duct-like spaces surrounded by a fibroblastic stroma. The load was applied from the bottom side of the sample. Figure IV.5 shows the FFOCT axial scan over a depth of 75μm with maps of axial and lateral displacement and its strain component map.

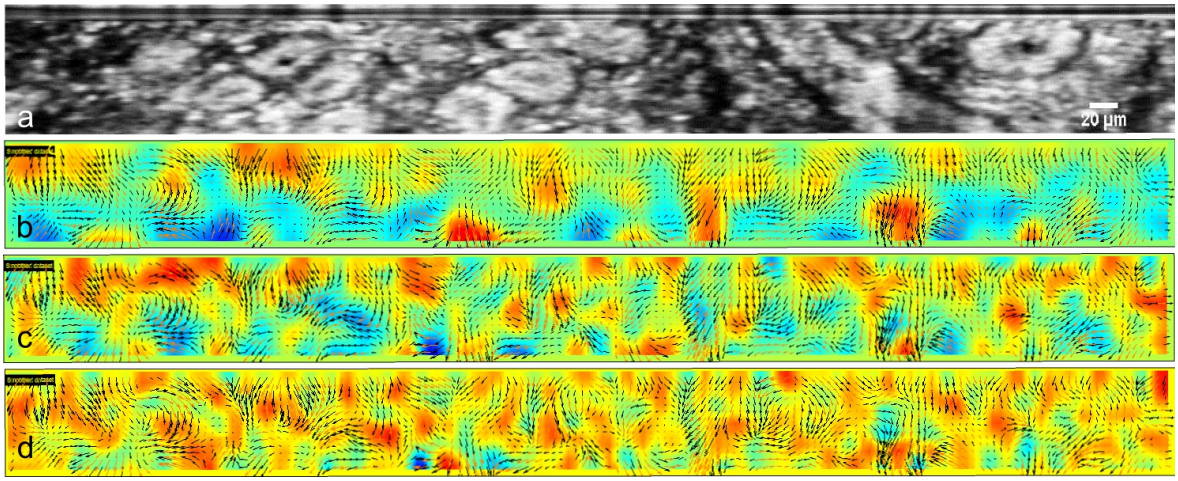

Figure IV.5: a) FFOCT original image after load. b) vertical displacement map. c) lateral displacement map. d) strain component map. Color scale: from blue to red. Red indicates high magnitude in displacement. z-axis depth: 75μm.

The strain map shows the high elastic heterogeneity of individual elements in the tissue. Some red zones indicates structures with higher magnitudes of displacement within the window of interrogation. A possible hypothesis would be to correlate those areas with more rigid tissue structures. This assumption is discussed in more details in the discussion section.

In this first feasibility tests, the piston or the sample-holder was not equipped with pressure sensors which limits any numerical data. The relative displacement was measured by measuring the piston length and monitored via the acquisition software. It was later found that the Young's modulus of breast tissues is highly dependent on the level of tissue pre-load.

IV.2.4 Discussion

This study shows the feasibility of a FFOCT setup to obtain micron-scale strain maps of tissues. In order to fully characterize the biomechanical properties of tumorous cells, several aspects need to be taken into consideration.

As mentioned, biological tissues are anisotropic and their response to an external load has both an elastic and a viscous component. A possible way of solving this problem, as suggested by Sun et al., would require to determine in advance both the elastic and viscoelastic properties of soft tissues. And more generally, it would require to describe the behaviour of individual tissues depending on the conditions of interest such as parameters of the loading profile, material properties, geometric feature of the structure, boundary conditions, and/or a combination of these behaviours[48].

Understanding the properties of individual cancerous cells at the micron-scale is of great importance. Several studies have reported considerably lower viscoelasticity of tumour cells compared to normal tissue [50], [51]. Cell lines examples include breast, bladder or pancreatic cancer. These findings appear consistent with their ability to move through tissue, to intravasate into the blood and lymph systems, and finally to form metastases. The highly heterogeneous strain map presented in the results could potentially illustrate this aspect. Therefore, the micron-scale resolution is both an advantage and a major limitation of optical-coherence elastography compared to traditional elastography techniques.

In addition, an important criteria in the correlation-based algorithm is the size of the interrogation window. A too small window may induce inaccurate strain maps. Likewise, too large windows tend to average out displacement differences of small structures and would lose in precise displacement tracking. From this preliminary experiment, this has been one of the major difficulty encountered. Thus far, strain map are calculated from the gradient of displacement fields but the differentiation calculation is highly sensitive to local errors. Examples can include excessive surface displacement (e.g. in-plane, out-of-plane or rotational) or excessive surface tilt.

Kirkpatrick et al. proposed two separate methods for small and large deformation. For large tissue displacement, an approach based on the Doppler effect was used, while a maximum-likelihood estimation method was implemented for small deformations. A mask or convolution kernel was directly generated from the grey values of a small background region of the strain-encoded map; and then convolved with this kernel in 2 dimensions to display the local strain magnitude [38].

Finally, a 3-D correlation approach should be considered since 2-Dimension correlation do not take into consideration out of plane displacements in the x,y direction (or x-,z- axis if “en-face” view). Recently, Optical-coherence elastography with 3-D maps have been performed on in-vivo skin specimen [42].

Additional applications are expected to be explored due to the high resolution offered by full-field optical coherence elastography in areas such as tissue engineering or to measure the biomechanical properties of large cancer cell models in-vivo.

IV.2.5 Conclusion

Results presented here demonstrate that the optical scattering properties of a biological tissue may be obtained with full-field optical coherence tomography. Further studies are often warranted to define the validity of the proposed methodology for potential diagnostic use. However, in this case, several limits have been highlighted, such as inhomogeneous structures over only a few microns and a variety of conflicting attenuation coefficients for a specific tissue.

On the other hand, Optical-coherence elastography holds greater prospects for characterizing tissue internal structure at the micron-scale level and imaging the spatial distribution of tissue elasticity. However, cancerous cells biomechanical properties need to be more fully understood in order to extract valuable diagnostic information. Micron-scale resolution provides both advantages and limitations compared to traditional ultrasound or MRI elastography which can assess larger areas and focus on large cluster of tumorous cells. At the cellular-level, malignant cells have highly heterogeneous viscoelastic properties that need to be taken into consideration.

References

[1] C. Compton, “Getting to personalized cancer medicine: taking out the garbage.,” *Cancer*, vol. 110, no. 8, pp. 1641-3, Oct. 2007.

[2] J. C. Denny et al., “Identification of genomic predictors of atrioventricular conduction: using electronic medical records as a tool for genome science.,” *Circulation*, vol. 122, no. 20, pp. 2016-21, Nov. 2010.

[3] D. M. Roden et al., “Development of a large-scale de-identified DNA biobank to enable personalized medicine.,” *Clinical pharmacology and therapeutics*, vol. 84, no. 3, pp. 362-9, Sep. 2008.

[4] M. S. Patterson, B. C. Wilson, and D. R. Wyman, “The propagation of optical radiation in tissue I. Models of radiation transport and their application,” *Lasers in Medical Science*, vol. 6, no. 2, pp. 155-168, Jun. 1991.

[5] A. Ishimaru, “Diffusion of light in turbid material,” *Applied Optics*, vol. 28, no. 12, p. 2210, Jun. 1989.

[6] S. G. Demos, A. J. Vogel, and A. H. Gandjbakhche, “Advances in optical spectroscopy and imaging of breast lesions.,” *Journal of mammary gland biology and neoplasia*, vol. 11, no. 2, pp. 165-81, Apr. 2006.

[7] V. V. Tuchin, *Tissue optics: light scattering methods and instruments for medical diagnosis*. SPIE Press, 2007, p. 840.

[8] S. A. Prahl, M. J. C. van Gemert, and A. J. Welch, “Determining the optical properties of turbid mediaby using the adding–doubling method,” *Applied Optics*, vol. 32, no. 4, p. 559, Feb. 1993.

[9] S. L. Jacques, “Time resolved propagation of ultrashort laser pulses within turbid tissues,” *Applied Optics*, vol. 28, no. 12, p. 2223, Jun. 1989.

[10] V G Peters et al, “Optical properties of normal and diseased human breast tissues in the visible and near infrared,” *Physics in Medicine and Biology*, vol. 35, no. 9. p. 1317, 1990.

[11] J. Qu, C. MacAulay, S. Lam, and B. Palcic, “Optical properties of normal and carcinomatous bronchial tissue,” *Applied Optics*, vol. 33, no. 31, p. 7397, Nov. 1994.

[12] D. Levitz et al., “Determination of optical scattering properties of highly-scattering media in optical coherence tomography images,” *Optics Express*, vol. 12, no. 2, p. 249, Jan. 2004.

[13] A. L. Clark, A. Gillenwater, R. Alizadeh-Naderi, A. K. El-Naggar, and R. Richards-Kortum, “Detection and diagnosis of oral neoplasia with an optical coherence microscope,” *Journal of Biomedical Optics*, vol. 9, no. 6, pp. 1271-1280, Nov. 2004.

[14] R. A. McLaughlin, L. Scolaro, P. Robbins, S. Hamza, C. Saunders, and D. D. Sampson, “Imaging of Human Lymph Nodes Using Optical Coherence Tomography: Potential for Staging Cancer,” *Cancer Res*, vol. 70, no. 7, pp. 2579-2584, Apr. 2010.

[15] A. F. Fercher, W. Drexler, C. K. Hitzenberger, and T. Lasser, “Optical coherence tomography - principles and applications,” *Reports on Progress in Physics*, vol. 66, no. 2, pp. 239-303, 2003.

[16] K. Bizheva, A. Siegel, and D. Boas, “Path-length-resolved dynamic light scattering in highly scattering random media: The transition to diffusing wave spectroscopy,” *Physical Review E*, vol. 58, no. 6, pp. 7664-7667, Dec. 1998.

[17] A. Miyazawa et al., “Tissue discrimination in anterior eye using three optical parameters obtained by polarization sensitive optical coherence tomography.,” *Optics express*, vol. 17, no. 20, pp. 17426-40, Sep. 2009.

[18] C. Xu, J. M. Schmitt, S. G. Carlier, and R. Virmani, “Characterization of atherosclerosis plaques by measuring both backscattering and attenuation coefficients in optical coherence tomography.,” *Journal of biomedical optics*, vol. 13, no. 3, p. 034003.

[19] J. M. Schmitt, A. Knüttel, M. Yadlowsky, and M. A. Eckhaus, “Optical-coherence tomography of a dense tissue: statistics of attenuation and backscattering.,” *Physics in medicine and biology*, vol. 39, no. 10, pp. 1705-20, Oct. 1994.

[20] F. J. van der Meer, D. J. Faber, D. M. Baraznji Sassoon, M. C. Aalders, G. Pasterkamp, and T. G. van Leeuwen, “Localized measurement of optical attenuation coefficients of atherosclerotic plaque constituents by quantitative optical coherence tomography.,” *IEEE transactions on medical imaging*, vol. 24, no. 10, pp. 1369-76, Oct. 2005.

[21] E. Cauberg, D. de Bruin, and D. Faber, “Quantitative measurement of attenuation coefficients of bladder biopsies using optical coherence tomography for grading urothelial carcinoma of the bladder,” *dare.uva.nl*.

[22] G. van Soest et al., “Atherosclerotic tissue characterization in vivo by optical coherence tomography attenuation imaging.,” *Journal of biomedical optics*, vol. 15, no. 1, p. 011105.

[23] A. I. Kholodnykh, I. Y. Petrova, M. Motamedi, and R. O. Esenaliev, “Accurate measurement of total attenuation coefficient of thin tissue with optical coherence tomography,” *IEEE Journal of Selected Topics in Quantum Electronics*, vol. 9, no. 2, pp. 210-221, Mar. 2003.

[24] L. Meng, B. Lv, S. Zhang, and B. Yv, “In vivo optical coherence tomography of experimental thrombosis in a rabbit carotid model.,” *Heart (British Cardiac Society)*, vol. 94, no. 6, pp. 777-80, Jun. 2008.

[25] H. Key, E. R. Davies, P. C. Jackson, and P. N. T. Wells, “Optical attenuation characteristics of breast tissues at visible and near-infrared wavelengths,” *Physics in Medicine and Biology*, vol. 36, no. 5, pp. 579-590, May 1991.

[26] E. R. Frykberg, “Lobular Carcinoma In Situ of the Breast,” *The Breast Journal*, vol. 5, no. 5, pp. 296-303, Sep. 1999.

[27] T. Collier, M. Follen, A. Malpica, and R. Richards-Kortum, “Sources of scattering in cervical tissue: determination of the scattering coefficient by confocal microscopy,” *Applied Optics*, vol. 44, no. 11, p. 2072, Apr. 2005.

[28] E. Cauberg and D. de Bruin, “Quantitative measurement of attenuation coefficients of bladder biopsies using optical coherence tomography for grading urothelial carcinoma of the bladder,” *Journal of Biomedical Optics,* 2010.

[29] L. Thrane, H. T. Yura, and P. E. Andersen, “Analysis of optical coherence tomography systems based on the extended Huygens–Fresnel principle,” *Journal of the Optical Society of America A*, vol. 17, no. 3, p. 484, Mar. 2000.

[30] J. M. Schmitt and A. Knüttel, “Model of optical coherence tomography of heterogeneous tissue,” *Journal of the Optical Society of America A*, vol. 14, no. 6, p. 1231, Jun. 1997.

[31] L. Scolaro et al., “Parametric imaging of the local attenuation coefficient in human axillary lymph nodes assessed using optical coherence tomography.,” *Biomedical optics express*, vol. 3, no. 2, pp. 366-79, Feb. 2012.

[32] G. Sadigh, R. C. Carlos, C. H. Neal, and B. A. Dwamena, “Accuracy of quantitative ultrasound elastography for differentiation of malignant and benign breast abnormalities: a meta-analysis.,” *Breast cancer research and treatment*, pp. 1-9, Mar. 2012.

[33] J. Ophir, I. Céspedes, H. Ponnekanti, Y. Yazdi, and X. Li, “Elastography: a quantitative method for imaging the elasticity of biological tissues.,” *Ultrasonic imaging*, vol. 13, no. 2, pp. 111-34, Apr. 1991.

[34] K. J. Parker, L. S. Taylor, S. Gracewski, and D. J. Rubens, “A unified view of imaging the elastic properties of tissue,” *The Journal of the Acoustical Society of America*, vol. 117, no. 5, p. 2705, May 2005.

[35] K. J. Parker, M. M. Doyley, and D. J. Rubens, “Imaging the elastic properties of tissue: the 20 year perspective.,” *Physics in medicine and biology*, vol. 56, no. 1, p. R1-R29, Jan. 2011.

[36] J. Schmitt, “OCT elastography: imaging microscopic deformation and strain of tissue,” *Optics Express*, vol. 3, no. 6, p. 199, Sep. 1998.

[37] R. K. Wang, Z. Ma, and S. J. Kirkpatrick, “Tissue Doppler optical coherence elastography for real time strain rate and strain mapping of soft tissue,” *Applied Physics Letters*, vol. 89, no. 14, p. 144103, Oct. 2006.

[38] S. J. Kirkpatrick, R. K. Wang, and D. D. Duncan, “OCT-based elastography for large and small deformations,” *Optics Express*, vol. 14, no. 24, p. 11585, Nov. 2006.

[39] Y. P. Zheng et al., “High resolution ultrasound elastomicroscopy imaging of soft tissues: system development and feasibility,” *Physics in Medicine and Biology*, vol. 49, no. 17, pp. 3925-3938, Sep. 2004.

[40] S. G. Adie, B. F. Kennedy, J. J. Armstrong, S. A. Alexandrov, and D. D. Sampson, “Audio frequency in vivo optical coherence elastography.,” *Physics in medicine and biology*, vol. 54, no. 10, pp. 3129-39, May 2009.

[41] X. Liang, A. L. Oldenburg, V. Crecea, E. J. Chaney, and S. A. Boppart, “Optical micro-scale mapping of dynamic biomechanical tissue properties,” *Optics Express*, vol. 16, no. 15, p. 11052, Jul. 2008.

[42] B. F. Kennedy et al., “In vivo three-dimensional optical coherence elastography,” *Optics Express*, vol. 19, no. 7, p. 6623, Mar. 2011.

[43] R. Karimi, T. Zhu, B. E. Bouma, and M. R. K. Mofrad, “Estimation of nonlinear mechanical properties of vascular tissues via elastography.,” *Cardiovascular engineering (Dordrecht, Netherlands)*, vol. 8, no. 4, pp. 191-202, Dec. 2008.

[44] R. C. Chan et al., “OCT-based arterial elastography: robust estimation exploiting tissue biomechanics,” *Optics Express*, vol. 12, no. 19, p. 4558, Sep. 2004.

[45] J. Rogowska, “Optical coherence tomographic elastography technique for measuring deformation and strain of atherosclerotic tissues,” *Heart*, vol. 90, no. 5, pp. 556-562, May 2004.

[46] X. Liang, S. G. Adie, R. John, and S. A. Boppart, “Dynamic spectral-domain optical coherence elastography for tissue characterization,” *Optics Express*, vol. 18, no. 13, p. 14183, Jun. 2010.

[47] A. Oberai, “Towards the Early Detection of Breast Cancer in Young Women,” 2005.

[48] C. Sun, “Optical coherence elastography: current status and future applications,” *Journal of Biomedical Optics*, 2011.

[49] W. Thielicke., “PIVlab - time-resolved particle image velocimetry (PIV) tool. Code covered by the BSD License.,” *http://pivlab.blogspot.com/*, 2011. [Online]. Available: http://pivlab.blogspot.com/.

[50] J. Guck et al., “Optical deformability as an inherent cell marker for testing malignant transformation and metastatic competence.,” *Biophysical journal*, vol. 88, no. 5, pp. 3689-98, May 2005.

[51] S. SURESH, “Biomechanics and biophysics of cancer cells☆,” *Acta Materialia*, vol. 55, no. 12, pp. 3989-4014, Jul. 2007.

[52] P. H. Tomlins, O. Adegun, E. Hagi-Pavli, K. Piper, D. Bader, and F. Fortune, “Scattering attenuation microscopy of oral epithelial dysplasia.,” *Journal of biomedical optics*, vol. 15, no. 6, p. 066003, Jan. 2010.

Chapter V. Advances in biology: in-vivo imaging of Drosophila melanogaster

Visualizing the dynamic formation of organs is the overarching goal in developmental biology. In order to elucidate underlying mechanisms that lead to form and function, the ability to image a developing embryo in three-dimension is essential. In small vertebrates or insects, the embryonic development has been extensively studied by imaging the embryo from the outside. However, mechanisms taking place underneath have so far been limited to tedious reconstruction of histology slides performed on postmortem specimens. Despite recent progress to achieve in-vivo imaging, an accurate understanding of the morphological changes happening inside a fully functioning living organism, such as insects, is still not well understood. This study on Drosophila melanogaster shows the feasibility of FFOCT to perform high-resolution imaging on living specimens during the transitional pupal phase of larva to adult fly, also known as metamorphosis. To our knowledge, these are the first images able to visualize the dynamic series of events of organ formation with a micron resolution in a living pupa.

V.1 Background

Attempts to perform in-vivo measurements with high resolution optical imaging techniques have so far been limited. Confocal microscopy is not particularly adapted for imaging embryos in-vivo over an extended period of time. The limiting factors include for example: vast amounts of laser light, photo-bleaching, photo-damage and heat. Recently introduced techniques have shown major improvements in the case of thin cultured cells or fixed and cleared tissues. These methods are yet still inadequate for large scattering objects. This incompatibility is particularly true for techniques that depend upon the interference or overlap of two laser beams or the projection of patterns; such as structured illumination, 4Pi or stimulated emission depletion. Aberrations occur due to the distortion of the intended pattern caused by scattering of the living specimen [1], [2].

Recently, a different approach has been demonstrated and shows promising results. It consists of recording the scattered light and then use an advance inversion scheme to reconstruct the fluorescence structure. The research group of Claudio Vinegoni in Boston, MA have been able to reconstruct green fluorescent protein (GFP) from a developing pupa by applying Fermi simplification of the Fokker-Planck solution of photon transport theory, which operates in a highly forward-scattering regime [3]. They succeeded to follow the morphogenesis of a pupa's wings in-vivo for six consecutive hours in three-dimension. In the study published in Nature Methods, they emphasize on the practical difficulties encountered by imaging opaque structures such as a developing Drosophila melanogaster. The prowess here is the penetration depth achieved, up to a few millimetres, associated with the ability to perform measurements on a living organism for a few hours. Nonetheless, this method called mesoscopic fluorescence tomography (MFT) is the still trading resolution for penetration depth [4].

An optical techniques offering higher resolutions (e.g. <5 μm) such as Born normalized Optical Projection Tomography (OPT) encounter difficulties associated with photon scattering within the tissue. In addition, the method requires having the sample made optically transparent through a chemical clearing process By doing so, scattering and absorption from the specimen are highly reduced, therefore making the diffuse light negligible [5],[6]. However, chemical treatment applied prevent any imaging in living organisms. Its major advantage is the possibility to track molecular contrast agents, which makes it a promising tool in combination with in-vivo imaging techniques.

Other non-optical methods have to be cited as alternatives for the imaging of in-vivo small animals and insects such as fruit flies. To this end, Magnetic resonance imaging (MRI) best known for anatomical imaging in clinical applications, has made tremendous progress towards microscopic imaging [7], [8]. Resolution of 100 μm in all dimensions is now routinely attained in living animals, and now 10 μm^3 is feasible in fixed specimens[9]. Likewise, microscopic CT imaging that depends on spatial differences in absorption of X-rays can also image the interior of small vertebrates and insects [10], [11]. Although studies with these two techniques have demonstrated key achievements bolstering their potential value, several limitations remain. Both techniques suffer from the necessity to use contrast agents which often lack flexibility or specificity (i.e. non-targetable) to monitor a particular organ growth or gene expression.

As far as the drosophila model is concerned, MRI appear to have taken a step ahead. A research group in Stanford have recently been able to reconstruct the inside of a living pupa and of an adult fly with high-field MRI of 18.8 Tesla [12]. This approach is potentially appealing to image larger embryo specimens such as mouse embryos or other vertebrates since the penetration depth achieves several centimetres in depth. However, the technique suffers a number of downsides. Although the magnet strength is strongly increased, the spatial resolution achieved is still in the region of 30 to 40 μm, a value not sufficient to identify and differentiate structures at the cellular-level during embryogenesis or morphogenesis.

In addition, the equipment cost of high field magnets or CT scanners dedicated to small animals can be rebutting for most laboratories, particularly if no specific staining can be visualized. Yet recent combinations of CT or MRI with PET or SPECT can now track specific contrast agents

over time. Such alternatives remain far from being applied to small-animal development imaging, mainly for cost and resolution limitations.

Drosophila melanogaster model

The fruit fly is one of the most studied eukaryote organism and a model of choice in genetics and medicine. Genes in Drosophila melanogaster are surprisingly and fortuitously very similar to humans. Closely related genes working in highly conserved regulatory networks are used to extrapolate findings for other species and humans in particular. Current knowledge about the molecular pathways of animal and human development comes from studies of model systems such as the fruit fly.

It is also a powerful model organism for developmental biologists. Larval development or embryogenesis has been extensively studied. However little is know about the development of organs taking place during metamorphosis (i.e. pupal stage). This phase of development is particularly poor in visual data and void of any in-vivo imaging of the dynamic mechanisms taking place underneath the cuticle –the brown protective outer covering surrounding the larva. The different phases of development are summarized in figure V.1 showing the two phases of metamorphosis: prepual and pupal stage.

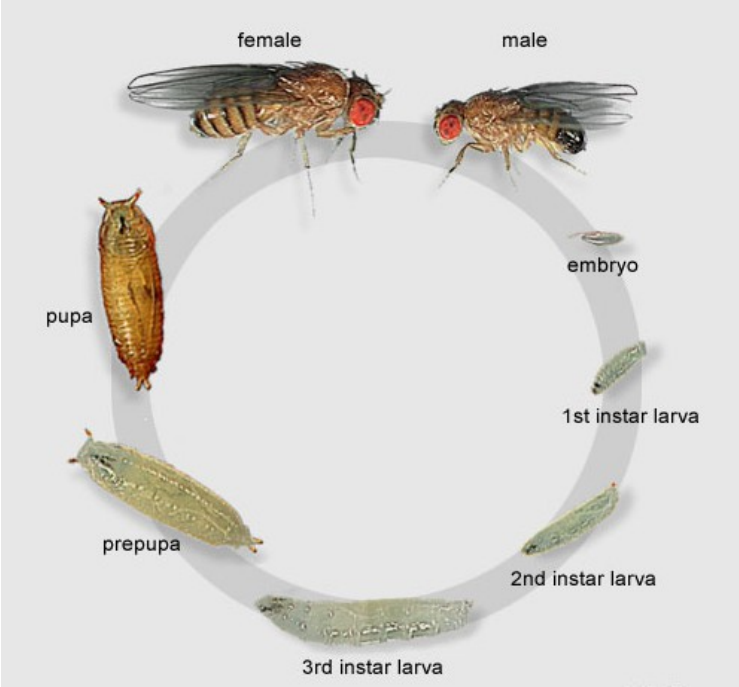

Figure V.1: Drosophila melanogaster life cycle. The pupa and prepupa phases are the focus of this study. Adapted from [25].

Once inside the pupal case, the larvae undergo dramatic changes in its body plan organization. This process takes about 96 to 100 hours to complete (i.e. approximately 4 days). Juvenile larval tissue disintegrates and are replaced through a rapid proliferation and differentiation of the cells that lead to the adult structure.

The adult fly emerges mainly from clusters of cells called *imaginal discs*. Contained within the body of the larva, there are pairs of apparently undifferentiated nests of cells that will form, for instance, the legs or antennae or other structures in the adult fly [13]. Thus, within any larva, there are two distinct populations of cells: the larval cells, which are used for the functions of the juvenile insect, and the thousands of imaginal cells, which lie in clusters, awaiting the signal to differentiate. There are 9 pairs of these, placed on either side of the larva body as shown on figure V.2.

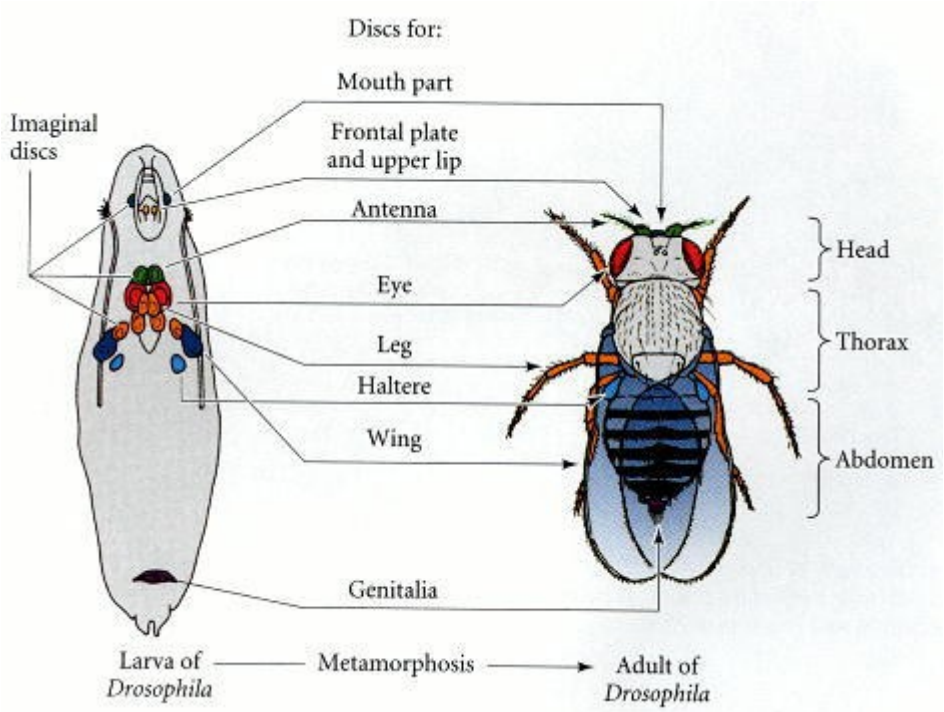

Figure V.2: The locations and developmental fates of the imaginal discs in Drosophila melanogaster. After[26] ,[23]

Imaginal discs are shaped like flattened balloons and will extend and differentiate during metamorphosis. For example, the eyes and antennae develop from one pair of discs, the wings part of the thorax from another, the same holds true for the first pair of legs, and so on [14–16]. The dynamic processes taking place inside the pupa is the subject of the current study –from the prepupal stage up to eclosion.

In brief, the transformation of the larval cuticle into a puparium marks the onset of metamorphosis. The puparium is initially soft and whitish yellow but very soon hardens, turning tan and eventually forms a protective yet brittle case.

V.2 Material and method

Instrument

A description of the full-field compact OCT system has been detailed in previous chapters. In brief, a white-light low-coherence halogen lamp illumination source is fibred to a beam splitter (interferometric principle of OCT). At one end, a silicon crystal mirror is cadenced by a piezoelectric stage actuator (reference arm) and the sample being imaged at the other end. A standard microscope objective (10X/0.3 numerical aperture, UMPLAN FLN, Olympus) is mounted on both extremities. A high-speed CMOS camera is synchronized with the piezoelectric oscillations and records the interference pattern at each pixel.

For this particular experiment, the objectives were immersed in silicon oil. The difference in refractive index between oil (n=1.40) and water does not induce significant spherical aberrations on the image output with our full-field OCT system. It must be noted that silicon oil is the immersion medium in both arms which also limits the consequence of the index mismatch.

Image acquisition

Series of 100 optical sections distant by 1 µm (z-axis) were acquired with a field of view 800×800 µm² at 16-bit colour depth. For each image, a smooth blurring and summation of 2 to 5 consecutive z-stack was applied. Stack of images were stored as TIFF files but JPEG format are presented (85% compression).

During the 4 days of recording (i.e. 96 h), an illumination timer was automatically activated every 6 hours for a duration of 45 minutes to avoid dehydration of the insect. The number of image accumulation was set to 250 images for each section of 100 µm z-stacks. With a camera frequency of 130Hz, one field of view of 800×800 µm² takes around 4 seconds per image and the overall acquisition time took approximately 7 minutes.

A depth-related index correction was applied by assuming a refractive index of 1.55 for the chitin [17–19]. As derivative of glucose, chitin is one of the main component of the larval cuticle with proteins [20], [21].

Pupa preparation

Pupa strains were a *mutant W118* with white eyes phenotype. An early pupa (prepual stage P0/P1), still white-yellowish (end of larval phase) was selected for the experiment. The pupa was delicately placed onto a glass slide (size adapted to the sample holder) within a drop of olive oil. A thin foil of olive oil has been shown to improve the signal to noise ratio as it matches the refractive index of the silicone window. Olive oil is also a crucial aid to allow respiration and maintain the insect alive during the entire metamorphosis. The pupa and the glass slide were then placed into the sample holder and maintained slightly compressed by the piston. Such manipulation allows to

be as close as possible from the pupa's cuticle and to slightly flatten the ovoid shape of the pupa in order to maintain an adequate signal up to 80—100 µm in depth.

Nonetheless, since our study focuses on pupal development over an extensive period of time (i.e. 96h), it is imperative to keep the pupal case intact throughout the measurements. As mentioned by Vinegoni et al. with mesoscopic imaging, even a minor resection significantly alter the mechanical strength of the pupa, resulting in loss of internal fluids, change of shape, size and eventually leading to a death of the insect. Another crucial factor was to maintain the environment at a relative high humidity. It was done so via the use of olive oil and by constant aeration through air holes present all around the sample holder. Although a tungsten halogen lamp is relatively harmless (2 mW/mm²), the heat generated can still cause an environment not supported by the insect and was therefore only activated every 6 hours.

Major steps of the pupal phase

An outline synopsis of the 15 key pupal stages used in this work are summarized in figure V.3 with a selection of 6 characteristic photographs (figure V.4).

Stage	Time (hours)	Developmental event
P1	0–1	White puparium: wriggling stops completely
P2	1–3	Brown puparium: oral armature stops moving permanently, heart stops pumping, gas bubble becomes visible within abdomen
P3	3–6.5	Bubble prepupa: puparium becomes separated from underlying epidermis; bubble in abdominal region is large, causing prepupa to become positively buoyant at end of this stage (it floats)
P4	6.5–12.5	Buoyant and moving bubble: prepupa is buoyant, and bubble moves, first appearing in the posterior of the puparium, displacing pupa anteriorly, and then appearing in the anterior, displacing the pupa posteriorly. Imaginal head sac is everted and oral armature of larva is expelled
P5	12.5–25	Malpighian tubules migrating and white: legs and wings extend; Malpighian tubules move from thorax to abdomen and become visible as white structures in dorsal anterior abdomen
P6	25–43	Green Malpighian tubules: Malpighian tubules turn green, and dark green "yellow body" appears between the anterior ends of the two Malpighian tubules
P7	43–47	"Yellow body": "yellow body" (actually dark green) moves back between the Malpighian tubules; transparent pupal cuticle separates from underlying epidermis; eye cup becomes yellow at its perimeter
P8	47–57	Yellow-eyed: eyes become bright yellow
P9	57–69	Amber: eyes darken to deep amber
P10	69–73	Red-eye Bald: eyes become bright red; orbital and ocellar bristles and vibrissae darken
P11	73–78	Head and thoracic bristles: head bristles, followed by thoracic bristles, darken
P12	73–78	Wings grey: wings become gray; sex comb darkens
P13	78–87	Wings black: wings become black; tarsal bristles darken and claws become black
p 14	87–90	Mature bristles: green patch (the meconium–waste products of pupal metabolism) appears dorsally at posterior tip of abdomen
P15	90–103	Meconium and eclosion: tergites become tan, obscuring Malpighian tubules and "yellow body"; legs twitch; flies able to walk prematurely if puparium removed; eclosion completed

Figure V.3: The 15 stages of pupation (prepupal and pupal phase). P1 starts approximately four days after the larval cycle and is characterized by a still white larva yet no longer able to crawl. Timing is variable among individuals, and hours given are a simplification from the reference paper of Bainbridge et al. and adapted from [21].

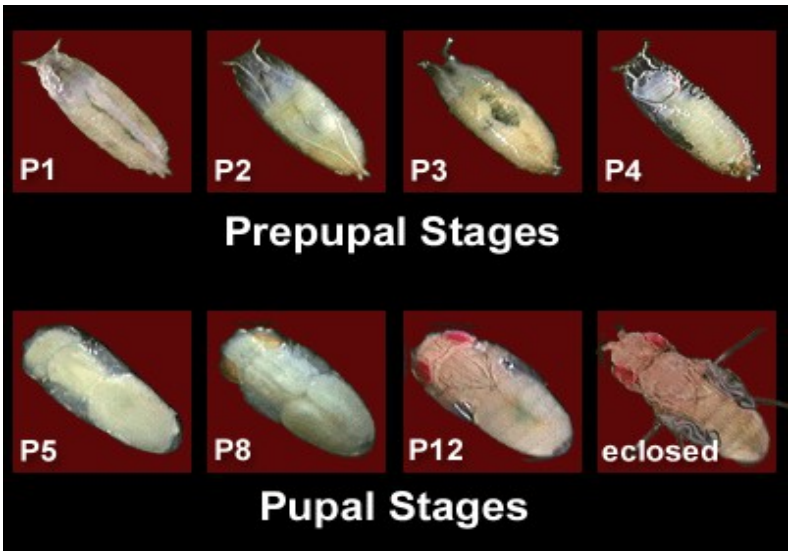

Figure V.4: photographs of different stages of pupation [24]

V.3 Results

A series of 3-D stacks of images has been recorded at high resolution and a sample of the results is presented. It should be underlined that three-dimensional data are obviously more adapted to a video mode to appreciate the dynamics of the changes taking place. Nonetheless the development of the pupa can still be tracked by following organs' growth in each individual images. Figure V.5 shows a picture of the pupa at the start of the experiment while still at prepupal stage (P0/P1) before turning darker for the following 96 hours of metamorphosis.

Figure V.6 highlights four critical stages of pupa metamorphosis. The ovoid shapes corresponds to undifferentiated nests of cells -the imaginal discs- in preparation of future organs. Those organs distinctly appear towards the end of pupation before eclosion as adult fruit fly.

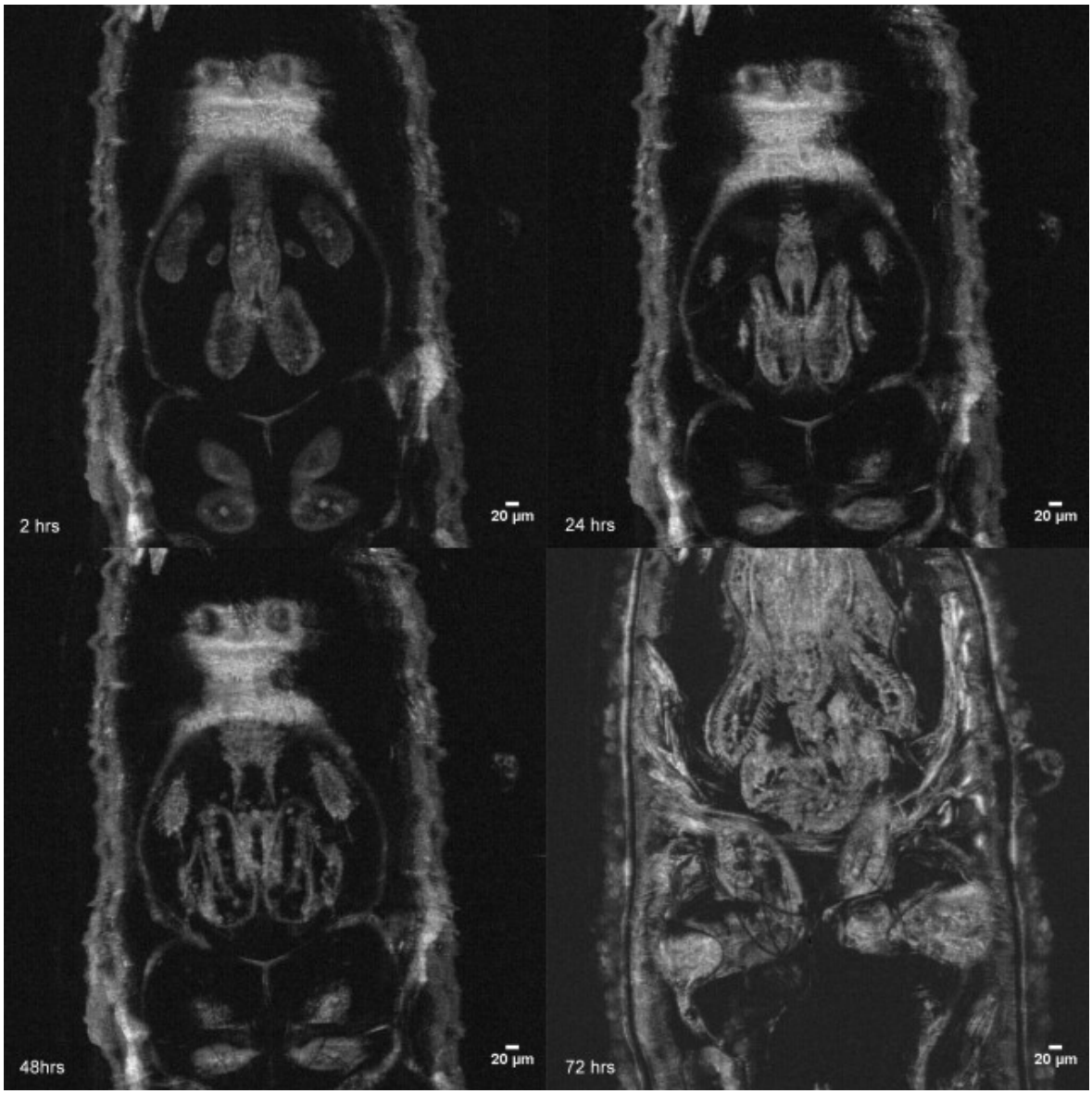

Figure V.7 exhibits the same four stages of development at three different depths (25, 40 and 65 µm) for each phase. The display starts from the early pupa at the top left to the fully developed insect at the bottom right.

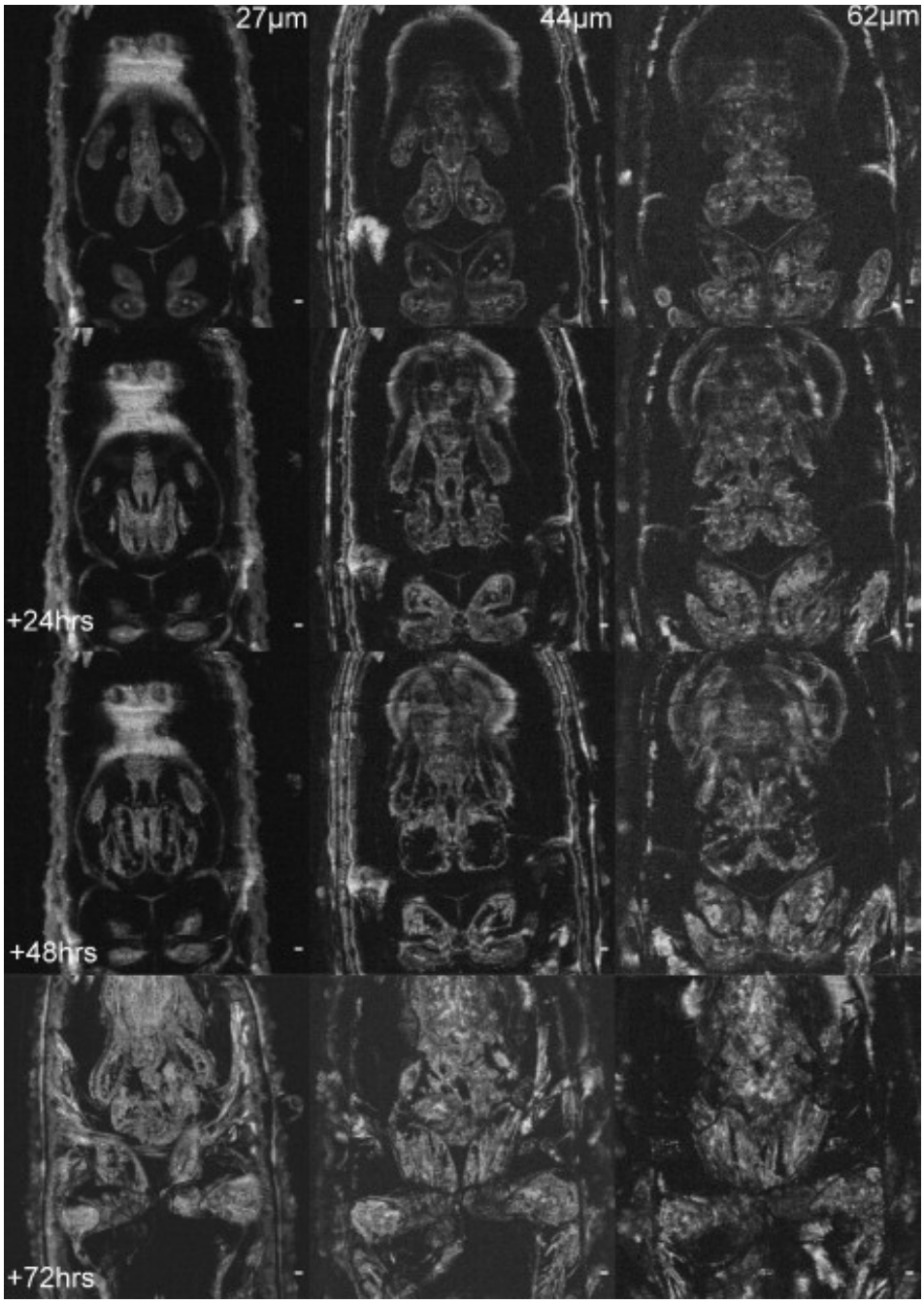

Figure V.7: 72 hours development: from early pupa at the top row (P0/P1), 24 h, 48 h and the fully developed pupa at the bottom-72 hours later (P11/P12). Different depth from the same hour of development are displayed vertically for the respective depths of: 27, 44 and 62µm.

As mean of comparison, a sample of traditional photographs taken from the outside of pupae at different stages of development are shown in figure V.8.

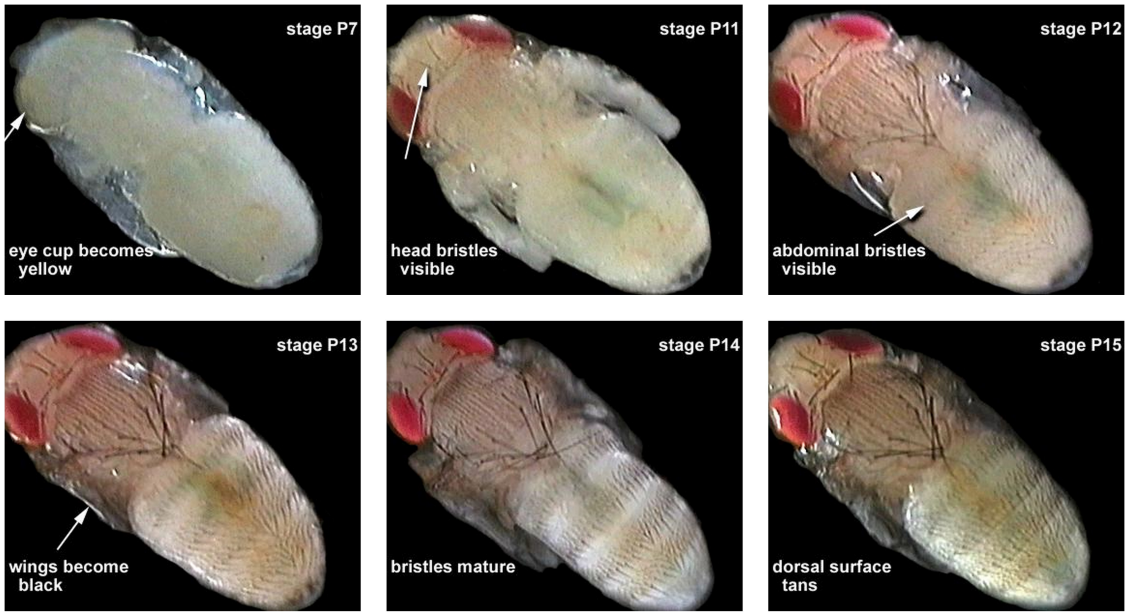

Figure V.8: examples of six stages from the pupal phase. Images taken after dissection of the puparium. From [24]

Imaginal discs present at the early stage of metamorphosis are undifferentiated nests of cells that will ultimately become a portion of the outside of the adult insect (e.g. legs, antennae, eyes, etc...). Two of these pairs are shown on figure V.7.

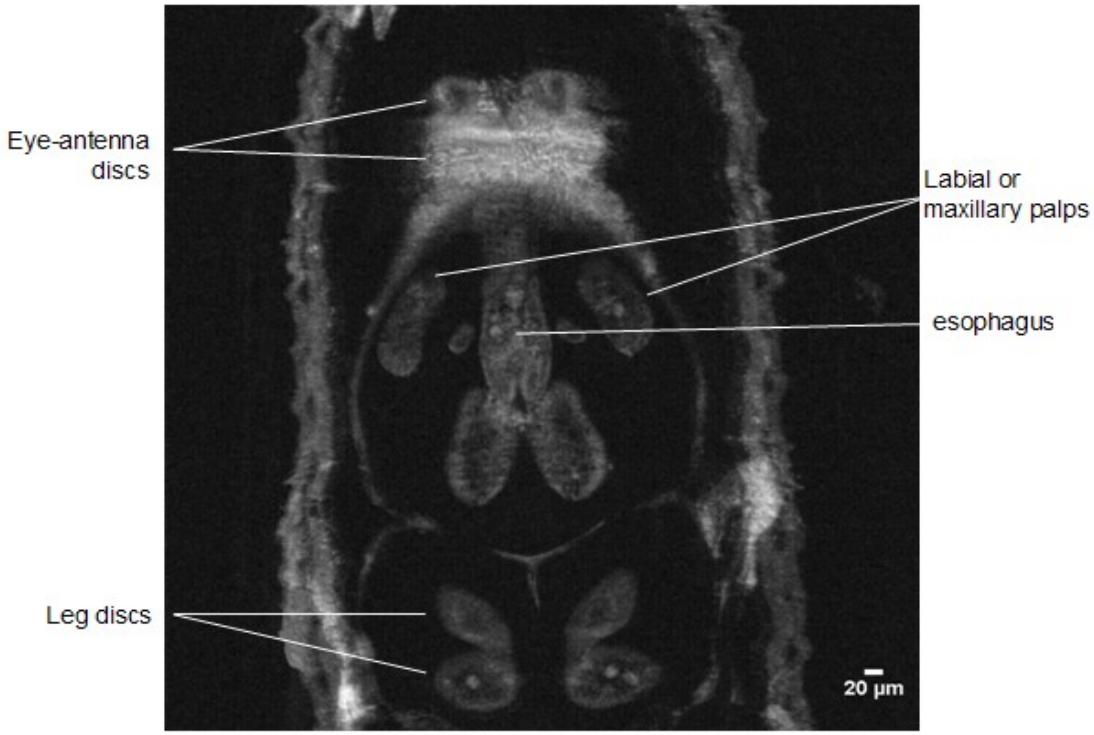

Figure V.9: Prepupa at 2 h (P1 stage) showing the imaginal discs (i.e. the undifferentiated nests of cells) responsible for the formation of a particular organ (e.g. legs, antenna, eyes, etc...).

Figure V.9 provides a series of images extracted from 10 to 50 µm in depth with an interval of 2 µm between each individual image. The list of images is taken at the median phase of the pupal development at the P8/P9 stage or approximately at 54 hours after the end of larval stage. Figure V.10 shows a focus at approximately 25 µm in depth.

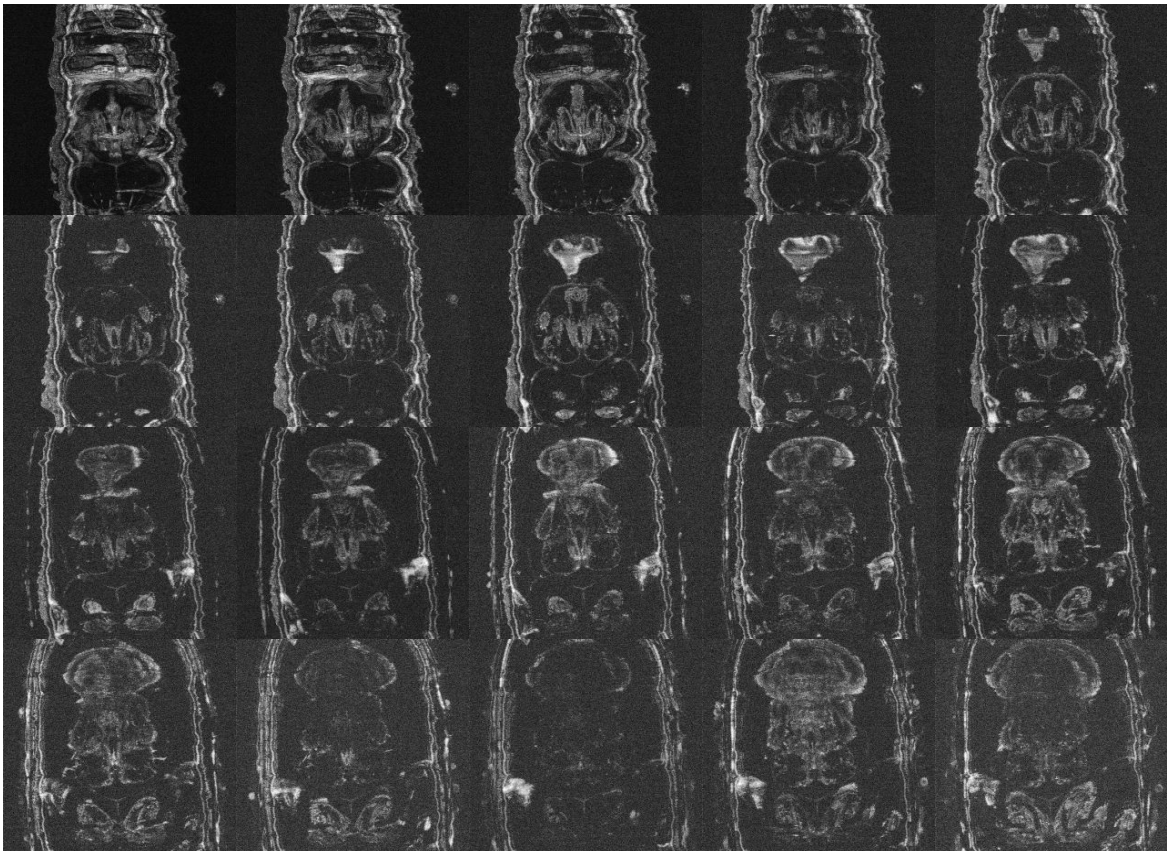

A 3-Dimensional profile allows to differentiate the relative position of each organs in formation. For example, the head positioned underneath the eye bulbs, which are placed under the oral armature in the puparium.

Adult fruit fly

Figure V.11 shows an adult fruit fly performed ex-vivo conditions. In this case, the insect was anaesthetized in ice and the head segment was imaged into an echographic gel. The image shows a sum of 30 z-stacks taken slightly from the top of the adult fly with its proboscis pointing towards the back (i.e. the mouthpiece of Drosophila melanogaster).

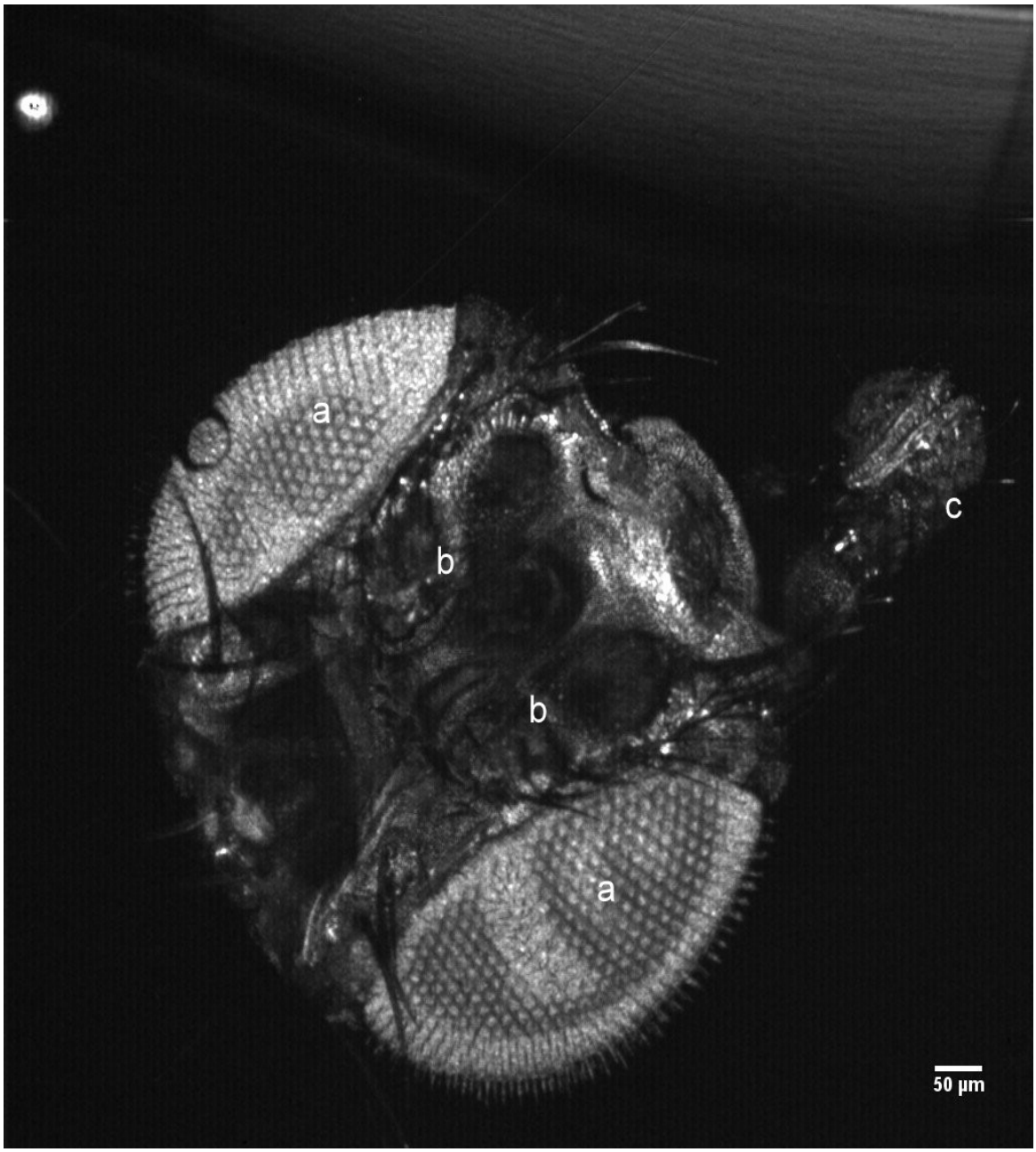

Figure V.11: Frontal view of a cutaway fly head by summation of 30 FFOCT z-stack images. It shows the main elements of the visual, sensory and olfactory systems: a) eyes with the hundreds of unit eyes or ommatidia; b) antenna pairs and c) the proboscis, the fly elongated mouthpiece. 1,024 × 1,024 pixels at 16-bit color depth.

V.4 Discussion

The conditions of the experiment were particularly challenging and notably the intricate balance for maintaining the fly alive during the four days of measurement. The combination of a thin

layer of olive oil and an appropriate pressure were the key factors to maintain the insect growth and stable during the four days of measurements. In comparison, ultrasonic gel turns into a highly scattering white jelly after several hours of exposition to air. In addition, a precise control of the lightning was crucial to avoid any overexposure to light and heat. Although the beam projects only 2 mW/mm^2 of light power intensity (i.e. approximately equivalent to sunlight), a prolonged exposure lead to a complete dehydration of the insect.

The circadian cycle of the fly was not particularly monitored yet this parameter seemed not to interfere with the experiment. In several insect species, adult eclosion commonly occurs during a narrow window of time, generally around dawn when environmental humidity is as its peak. However, studies have shown contradicting results regarding the correlation between periodicity of the environment (day or night) and/or the periodicity of eclosion rhythm [22]. In this study, full development was achieved and monitored throughout the median duration metamorphosis. In addition, image interpretation can be subject to errors since no other studies has shown the development of fruit flies organs underneath the surface with this resolution.

Nonetheless, the role of full-field OCT is not likely to supersede traditional microscopy techniques (e.g. confocal microscopy or two-photons microscopy), but to serve as potential complement. Microscopy techniques remain inadequate to monitor the evolution of a living drosophila in 3-D with a micron-scale resolution. Recent studies with high-field MRI (i.e. 18.8 T) show great progress for imaging the entire specimen [12],however the resolution remains 20 times lower than FFOCT (~20 µm). Regarding applications of 3-D in-vivo FFOCT for drosophila, a potential area of interest would be the analysis of altered phenotypes in mutant flies. A variety of mutant genotypes could be monitored during metamorphosis for example drosophila models of muscular dystrophy or particular anatomical areas such as the eye-antenna imaginal discs.

V.5 Conclusion

This study marks progress toward the development of a potential novel *in-vivo* imaging technique for developmental biology. FFOCT as a non-destructive optical method offer the ability to image the organ formation of a living organism at a depth of 80 -100 µm with an isotropic resolution of 1 µm. This method could allow to overcome the limitations of traditional microscopy techniques such as laser damage or postmortem slice reconstruction in the imaging of specific organs of small animals.

References

[1] S. W. Hell, “Far-field optical nanoscopy.,” *Science (New York, N.Y.)*, vol. 316, no. 5828, pp. 1153-8, May 2007.

[2] J. Huisken and D. Y. R. Stainier, “Selective plane illumination microscopy techniques in developmental biology.,” *Development (Cambridge, England)*, vol. 136, no. 12, pp. 1963-75, Jun. 2009.

[3] C. Vinegoni, D. Razansky, C. Pitsouli, N. Perrimon, V. Ntziachristos, and R. Weissleder, “Mesoscopic fluorescence tomography for in-vivo imaging of developing Drosophila.,” *Journal of visualized experiments : JoVE*, no. 30, Jan. 2009.

[4] C. Vinegoni, C. Pitsouli, D. Razansky, N. Perrimon, and V. Ntziachristos, “In vivo imaging of Drosophila melanogaster pupae with mesoscopic fluorescence tomography.,” *Nature methods*, vol. 5, no. 1, pp. 45-7, Jan. 2008.

[5] J. Sharpe et al., “Optical projection tomography as a tool for 3D microscopy and gene expression studies.,” *Science (New York, N.Y.)*, vol. 296, no. 5567, pp. 541-5, Apr. 2002.

[6] H.-U. Dodt et al., “Ultramicroscopy: three-dimensional visualization of neuronal networks in the whole mouse brain.,” *Nature methods*, vol. 4, no. 4, pp. 331-6, Apr. 2007.

[7] A. E. Petiet, M. H. Kaufman, M. M. Goddeeris, J. Brandenburg, S. A. Elmore, and G. A. Johnson, “High-resolution magnetic resonance histology of the embryonic and neonatal mouse: a 4D atlas and morphologic database.,” *Proceedings of the National Academy of Sciences of the United States of America*, vol. 105, no. 34, pp. 12331-6, Aug. 2008.

[8] G. A. Johnson, G. P. Cofer, S. L. Gewalt, and L. W. Hedlund, “Morphologic Phenotyping with MR Microscopy: The Visible Mouse,” *Radiology*, vol. 222, no. 3, pp. 789-793, Mar. 2002.

[9] B. Driehuys et al., “Small animal imaging with magnetic resonance microscopy.,” *ILAR journal / National Research Council, Institute of Laboratory Animal Resources*, vol. 49, no. 1, pp. 35-53, Jan. 2008.

[10] M. J. Paulus, S. S. Gleason, S. J. Kennel, P. R. Hunsicker, and D. K. Johnson, “High resolution X-ray computed tomography: an emerging tool for small animal cancer research.,” *Neoplasia (New York, N.Y.)*, vol. 2, no. 1-2, pp. 62-70.

[11] D. W. Holdsworth and M. M. Thornton, “Micro-CT in small animal and specimen imaging,” *Trends in Biotechnology*, vol. 20, no. 8, p. S34-S39, Aug. 2002.

[12] B. Null, C. W. Liu, M. Hedehus, S. Conolly, and R. W. Davis, “High-resolution, in vivo magnetic resonance imaging of Drosophila at 18.8 Tesla.,” *PloS one*, vol. 3, no. 7, p. e2817, Jan. 2008.

[13] S. F. Gilbert and S. Singer, *Developmental Biology, Eighth Edition*. Sinauer Associates Inc., 2006, p. 785.

[14] V. Hartenstein and J. A. Campos-Ortega, “Fate-mapping in wild-typeDrosophila melanogaster,” *Development Genes and Evolution*, vol. 194, no. 4, pp. 181–195, 1985.

[15] A. Martinez-Arias and P. A. Lawrence, “Parasegments and compartments in the Drosophila embryo.,” *Nature*, vol. 313, no. 6004, pp. 639-42.

[16] “Drosophila and the Molecular Genetics of Pattern Formation. II. Homeotic Selector Genes and the Patterning of Body Parts 41, 50.” Garland Science, 1994.

[17] G. S. Watson and J. A. Watson, “Natural nano-structures on insects–possible functions of ordered arrays characterized by atomic force microscopy,” *Applied surface science*, vol. 235, no. 1-2, pp. 139–144, 2004.

[18] M. Pryor, “On the hardening of the cuticle of insects,” *Proceedings of the Royal Society of London. Series B, Biological Sciences*, vol. 128, no. 852, pp. 393–407, 1940.

[19] I. B. J. Sollas, “On the identification of chitin by its physical constants,” *Proceedings of the Royal Society of London. Series B, Containing Papers of a Biological Character*, pp. 474–481, 1907.

[20] S. O Andersen, “Biochemistry of Insect Cuticle,” Nov. 2003.

[21] S. O. Andersen, P. Hojrup, and P. Roepstorff, “Insect cuticular proteins,” *Insect Biochemistry and Molecular Biology*, vol. 25, no. 2, pp. 153-176, Feb. 1995.

[22] D. A. Paranjpe, D. Anitha, M. K. Chandrashekaran, A. Joshi, and V. K. Sharma, “Possible role of eclosion rhythm in mediating the effects of light-dark environments on pre-adult development in Drosophila melanogaster.,” *BMC developmental biology*, vol. 5, no. 1, p. 5, Jan. 2005.

[23] D. Fristrom, “Cellular degeneration in the production of some mutant phenotypes in Drosophila melanogaster,” *MGG Molecular & General Genetics*, vol. 103, no. 4, pp. 363-379, Dec. 1969.

[24] M. S. Tyler, “Pupal stages | devbio.net.” [Online]. Available: http://www.devbio.net/node/120. [Accessed: 03-Oct-2011].

[25] K. Weigmann et al., “FlyMove – a new way to look at development of Drosophila,” *Trends in Genetics*, vol. 19, no. 6, pp. 310-311, Jun. 2003.

[26] Scott F Gilbert., “Developmental Biology.” Sinauer Associates, 2000.

Chapter VI. Infrared Full-Field OCT and penetration depth improvement

As presented in preceding chapters, OCT and FFOCT imaging for biological tissues is highly dependent upon scattering events. A general trend for the scattering coefficient, μ_s is to decrease with increasing wavelength. Therefore, a longer wavelength would potentially be more advantageous for deeper imaging.

However, there are two limitations to consider for the evaluation of imaging depth in biological tissues. The first one is the FFOCT setup detection sensitivity limit. The minimum signal detectable determines the maximum probing depth. The second and more crucial limit is the depth threshold at which contrast and image resolution degrade to a point were no useful information is provided. Such degradation has been hypothesized to result from multiple scattered light. For standard OCT that operates with a low numerical aperture beam (typically 10 times smaller than FFOCT), contrast loss due to deeper imaging should not be affected by the loss of focusing ability as it is the case with FFOCT or confocal microscopy, mostly using medium or large numerical apertures. In this work, the wavelength dependence of the scattering component was evaluated by comparison of penetration depth at lower wavelength ranges. This is detailed in the second part of the chapter while the first part presents the experimental system and its performance.

As with the other experimental work in this thesis, the contribution of several persons must be appropriately acknowledged in advance. In particular, Osnath Assayag, post-doctoral fellow and Sylvie Nadolny whose collaboration on the infrared setup made possible the results presented here. Florian Poisson, a graduate student at ESPCI Paristech who carried out several measurements shown in this chapter. Contributions from Fabrice Harms and Franck Martins from LLTech has also been crucial regarding machinery improvements and immersion medium properties. As far as the software and technical aspects are concerned, Charles Brossolet has been instrumental in all the related issues of this work.

VI.1 InGaAs FFOCT setup

VI.1.1 Background and objectives

As stated previously, two objectives were sought: first to improve the imaging depth in biological tissues and secondly to evaluate the variation in scattering level with regards to depth. The second objective will be discussed in the last part of this chapter.

For traditional OCT, longer wavelength systems operating in the 1050 nm and 1300 nm spectral bands were introduced soon after the first generation of systems operating in the visible range. Initially, the 700-850 nm range was particularly adapted to retinal examination since any larger wavelengths would have been restricted by the water dominant fluid-filled gap between the cornea and the retina. Above the 1100 nm wavelength the penetration restriction is imposed by the steep increase in the optical absorption of liquid water [1], [2]. With the first investigation of epithelial tissues (e.g. skin, oral mucosa, etc...), an improved penetration depth was demonstrated by Brezinski et al. in 1996. In the early experiment, a 1300 nm wavelength was employed on ex-vivo vascular tissues (i.e. atherosclerotic plaques).

In order to extend the capabilities of the full-field OCT technique and to improve the penetration depth without a loss in resolution, an infrared InGaAs FFOCT system has been developed for this purpose. As detailed in the introduction, imaging depth can be improved by using a detector optimized for a particular wavelength range. A general trend in biological tissues is a decrease in scattering coefficient with increasing wavelength. Therefore, a longer wavelength is potentially more advantageous for deeper imaging.

For FFOCT systems, the camera detection sensitivity range is the limiting factor and therefore silicone-based (Si) cameras are more commonly used to probe the 600-1000 nm wavelength region. Whereas for longer wavelengths (>1000 nm) Si cameras are advantageously replaced by Indium Gallium Arsenide (InGaAs) chips with a detection range in the 900-1700 nm band as shown in this work. Performance results presented here have been carried out in silicone oil immersion instead of liquid water. This type of configuration, according to the authors knowledge, has not been used in the past.

VI.1.2 Material and method

Infrared system

An indium gallium arsenide detector camera (InGaAs) has been used since its spectral quantum efficiency in the near-infrared ranges from 0.9 µm to 1.7 µm. As previously described, in FFOCT a low coherent light source illumination is used and therefore the effective spectrum output is limited by camera sensitivity response and the transmission of the optics. A coated infrared beamsplitter was used but microscope objectives were not optimized for this particular wavelength range (see discussion section). The InGaAs camera (Xeva-1.7-640c, Xenic, Leuven, Belgium) has been mounted onto a full-field OCT configuration as shown on figure VI.1.

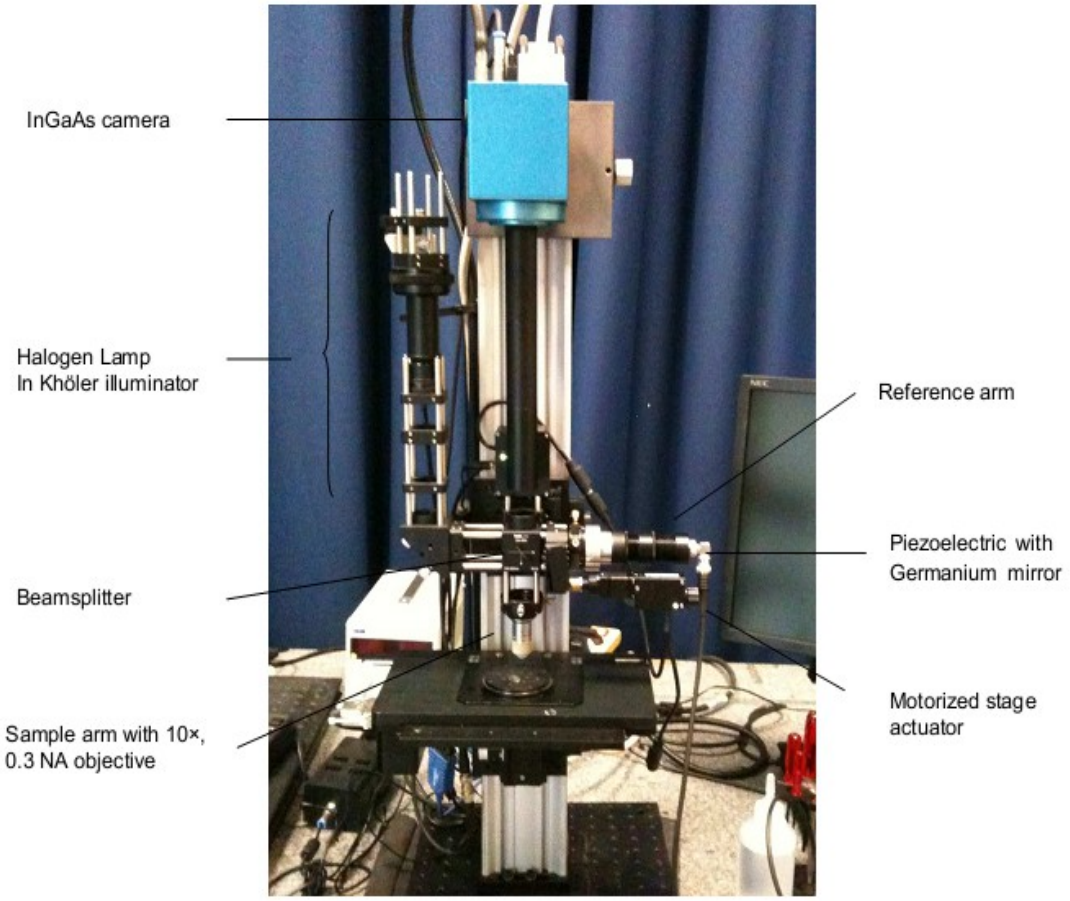

The InGaAs camera full-well capacity or the largest charge that the camera can hold per pixel before saturation is approximately 3 million e^- with and a frame rate of 25 Hz. Since silicone-based reflectors are transparent in the infrared, a Germanium rod was used instead for the reference arm. Its refractive index at 1100nm wavelength is n= 4.4 giving a reflectivity ratio of 27%. This configuration is noted as “IR” or infrared configuration in the text.

Si camera system.

This system configuration has been detailed in the previous chapter, here a fibre-bundle halogen light source has been used instead (Schott KL 1500). Measurements in the visible range were performed with a CMOS detector array (complementary metal oxide semiconductor – Photon Focus, MV-D1024E-160). The camera full well capacity (FWC) is around 0.2 million e^-. As far as speed considerations are concerned, the 15x lower full well capacity compared to the InGaAs camera is compensated by a frame rate of 150 Hz (6x higher). The effective spectrum of the system has been measured to peak at 710 nm with a bandwidth of approximately 125 nm. The reference mirror is a silicon wafer (n=3.42); within silicone oil immersion medium, a reflectivity of 17.5% has been measured. This configuration is noted as “visible” system in the text. Similar objectives (10x, 0.3NA, Olympus) were used in both configurations.

VI.1.3 Performance comparison

Measurements were performed at two distinct spectrum range: around 700 nm (visible) and 1100-1200 nm (near-infrared range or NIR) and by replacing the water-based immersion medium (echographic gel) by silicone oil (n=1.40-1.41). As previously discussed, this change has been dictated by practical considerations (dehydration, increase stability,...) but also appeared to increase the spectral bandwidth and the penetration depth, particularly in the near-IR range. The absorption spectrum of water is indeed a major limiting factor when imaging at higher wavelengths. The light beam has to cross over a 5 mm-thick layer of water, twice the objective working distance adjusted to n', the refractive index of the biological specimen (e.g. n'=1.37-1.40), and this cannot be neglected. Figure VI.2 shows the lower number of fringes when measurements are performed in oil immersion for the near-infrared setup (InGaAs) in comparison to water immersion.

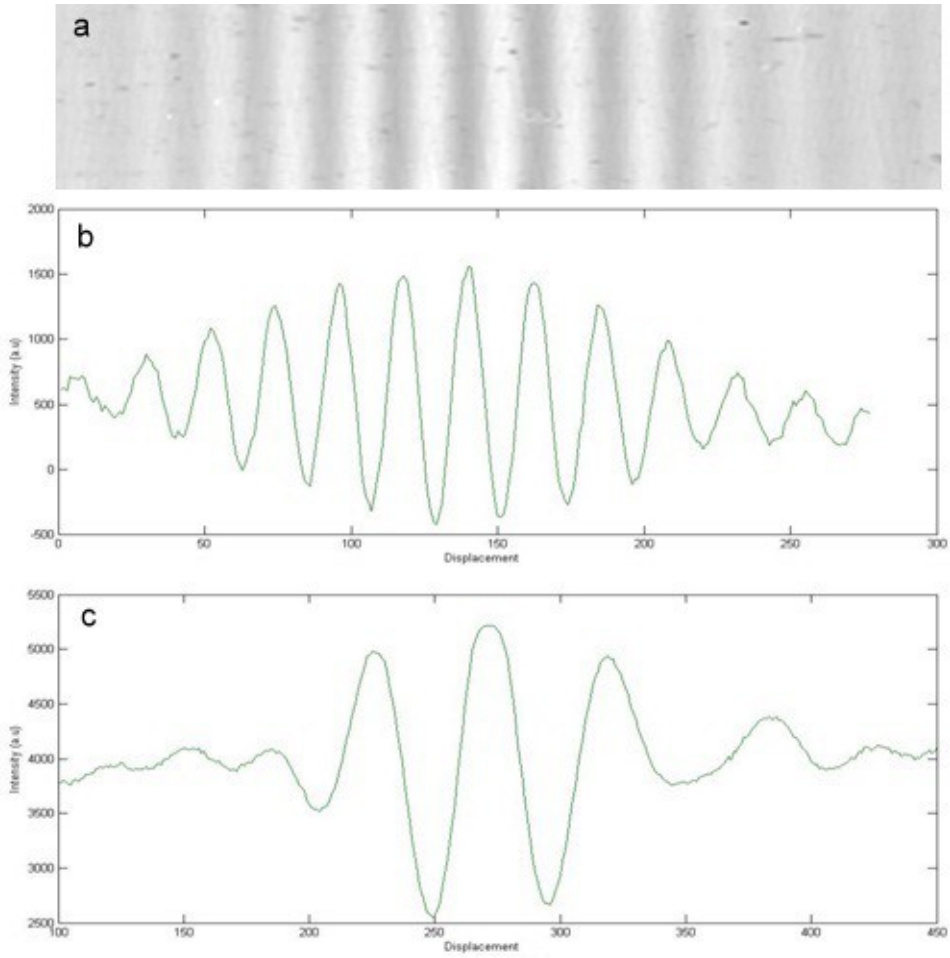

One can see the increased number of fringes with water immersion medium despite a thin layer of water (1 mm overall) compared to 6.6 mm in the case of silicone oil (2×3.3 mm). Silicone oil refractive index is about 1.41 which limits its usage to medium numerical aperture objectives (typically NA <0.35). Nonetheless it allows a quasi full transmission from 0.9 µm up to 1.6 µm (or 6250 cm^{-1}) except for two absorption bands as shown on figure I.3.

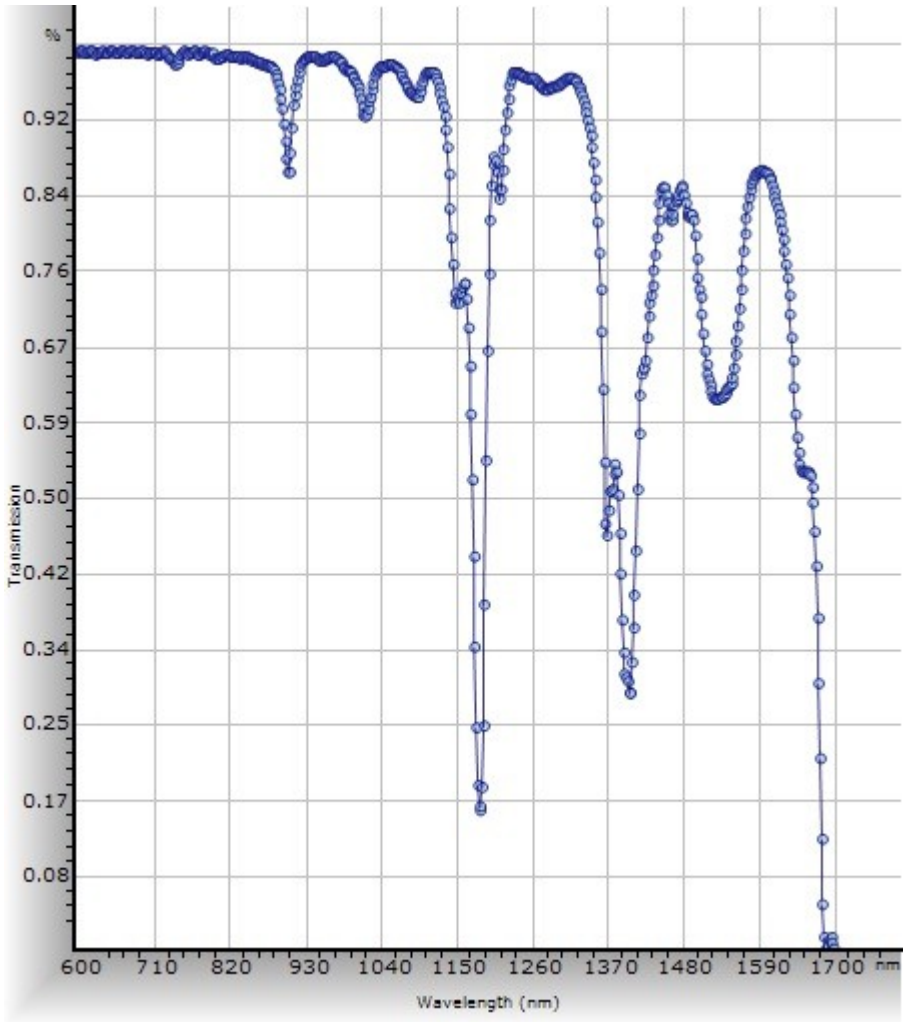

figure VI.3: Silicone oil transmission spectrum measured in a 1cm-thick cuvette. Note the two major dips near 1200 nm and 1400 nm wavelengths. Under experimental conditions, those two absorption dips are almost halved since only ~0.5 cm of silicone-oil is passed through – the frontal distance of the objective in water is 3.5 mm and 3.7 mm in silicone-oil, thus the beam path is about 5.4 mm or 0.54 cm (by subtracting the double pathlength of1 mm for the microscopic glass slide).

Silicone-oil immersion medium can thus be used as an alternative immersion liquid for both visible (Si camera) and near-infrared systems (InGaAs).

Figure VI.4 shows the effective spectrum deduced from inverse Fourier transform out of the interferograms for both the Si system in the visible range and the InGaAs setup with silicone oil immersion medium. The wings in the InGaAs effective spectrum are due to the dips from silicone oil absorption, in particular near 1200 nm.

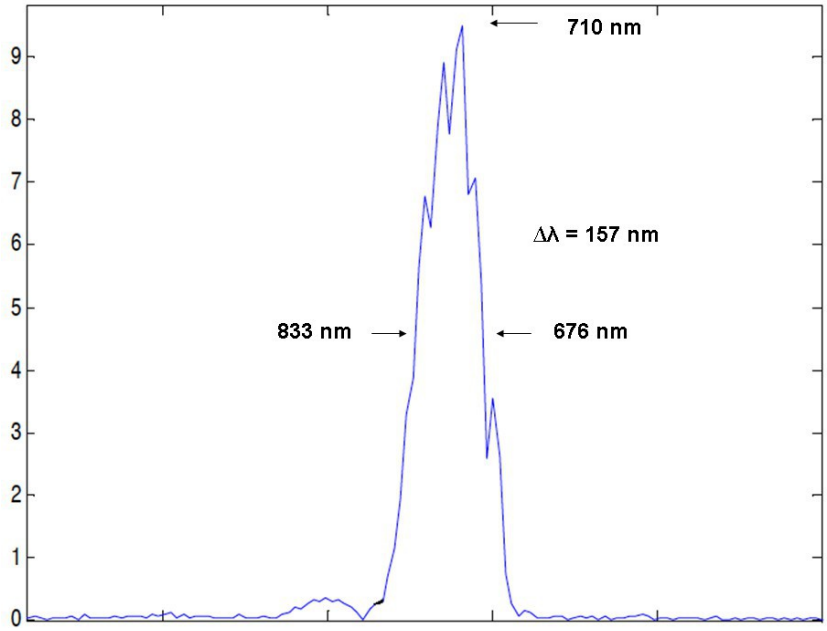
710 nm
Δλ = 157 nm
833 nm
676 nm
0
1
2
3
4
5
6
7
8
9

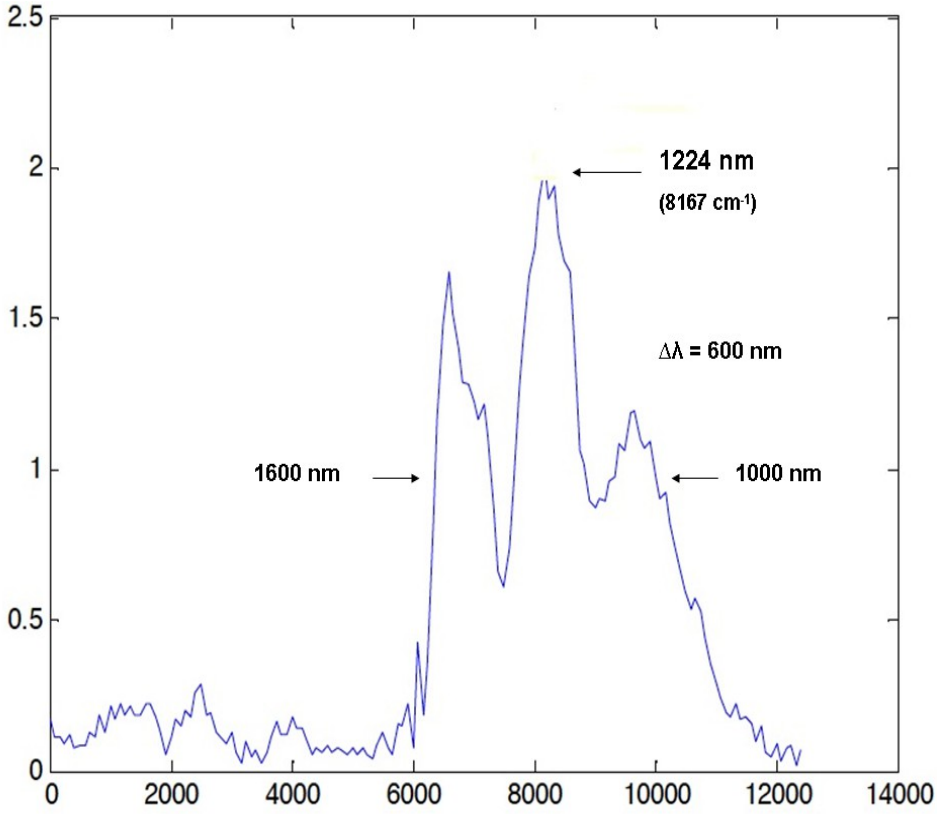
1224 nm
(8167 cm-1)
Δλ = 600 nm
1600 nm
1000 nm
0
0.5
1
1.5
2
2.5
0
2000
4000
6000
8000
10000
12000
14000

In comparison to a configuration with silicone-oil in the visible range (i.e. CMOS camera), the spectral bandwidth achieved by the InGaAs setup is significantly larger (i.e. ~ 600 nm vs. 150-200 nm) as seen on figure VI.5. For this bandwidth, the theoretical axial resolution is approximately similar in both configuration (around 1 µm). However, the gain lies in the effective spectrum achieved with silicone-oil immersion and therefore a gain in penetration depth. The high absorption of water above 1100 nm is thus drastically reduced by the oil immersion medium in both arms, allowing to fully benefit from the near-infrared part of the polychromatic light source. Recently, Dubois's group compared two similar FFOCT configurations (both silicon and InGaAs cameras) but within a water immersion medium showing the limitations of the water spectrum in the near-infrared range [5].

Thus, by replacing the immersion medium with silicone oil, results obtained in this study suggest that this approach takes full advantage of the possibilities offered by the infrared spectral response of the InGaAs camera.

VI.2 Penetration depth assessment in biological tissues.

VI.2.1 Background

Biological tissues are characterized by scatterers randomly distributed over the volume of interest or focal plane – under the condition of alignment with the coherence plane. As wavelength increases the damping of ballistic photons intensity in a scattering media decreases linearly in OCT [6], [7]. Within biological tissues, the mean free path of photons varies as λ^4 in the case of Rayleigh scattering (particle size much smaller than the wavelength) to λ^n (with $n<4$) in Mie scattering regime (particles larger than the wavelength).

In comparison to confocal microscopy, the penetration depth achieved with an interferometric technique such as FFOCT should in theory be improved. With a dual confocal and high-resolution OCT system (often referred as OCM for optical coherence microscopy), Aguirre et al. found that the confocal response alone degrades deep in tissue leading to loss of resolution [8]. This loss of resolution appears to be caused by a decreased ability to focus in tissue as confirmed by the widening confocal response profile. As the confocal signal would be the integral of the response profile over all depths, it confirms the hypothesis that the ratio of light detected from outside the focal plane to light returning from the focal plane increases and that signal to noise ratio limit is reached.

In contrast, the FFOCT approach used with the algorithm developed allows to maintain a constant focus with increased penetration into the tissue, by dynamic adjustment of the coherent

plane (see chapter on FFOCT instrument). However, contrast in FFOCT (and OCT) also degrades with depth.

The most probable hypothesis for this result is an increasing amount of multiple scattered light and not geometrical aberrations from the focus plane. These results are confirmed in this work for measurements performed within the 700-800 nm range (visible range) while the infrared part of the spectrum appears significantly less disrupted by multiple scattering events.

VI.2.2 Material and method

FFOCT system

Three different full-field OCT systems have been employed. Two systems in the visible range, with high-pass filters at 600 and 650 nm and the infrared system centred around 1200 nm. Each configuration was described earlier in this chapter. Measurements were performed under similar conditions by averaging 50 “en-face” scans from the same biological sample area.

Specimen properties

In the near-infrared spectrum, absorption by freshly excised breast tissues is mainly caused by oxy- and deoxy- haemoglobin, water and lipids. Figure VI.6 shows a modelled absorption spectrum for a water concentration of 70% and 30% of fat content. In fixed tissues, these are the two most absorbing chromophores which greatly influence the effective spectrum output (in particular above 1100 nm).

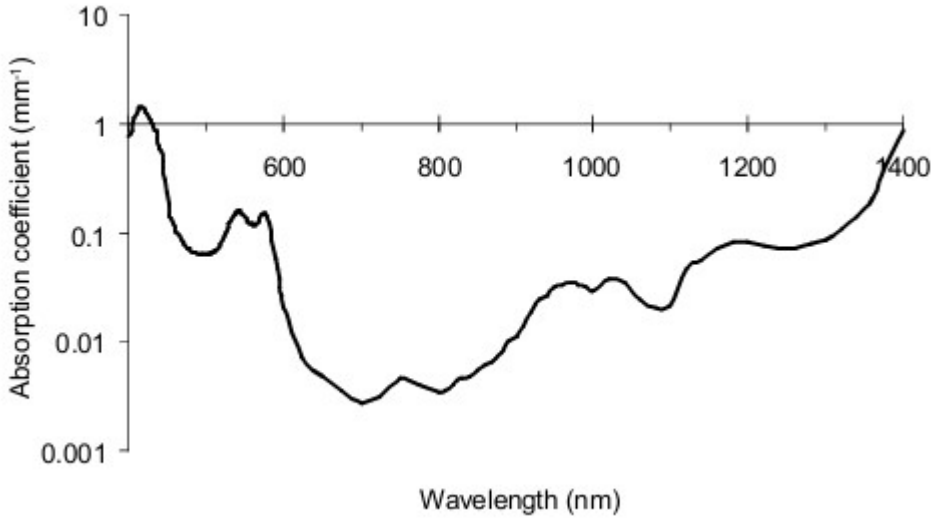

Figure VI.6: Absorption spectrum of a typical breast tissue obtained by calculating the absorption spectra of the contributing chromophores. A water concentration of 70%, a fat concentration of 30% and oxy-and deoxy-haemoglobin concentrations of 20µM and 10µM respectively. From (Eker, 1999).

VI.2.3 Results

Images comparison

Figures VI.7 and VI.8 show a cross section comparison for the breast fibroadenoma[8] sample obtained in each wavelength ranges.

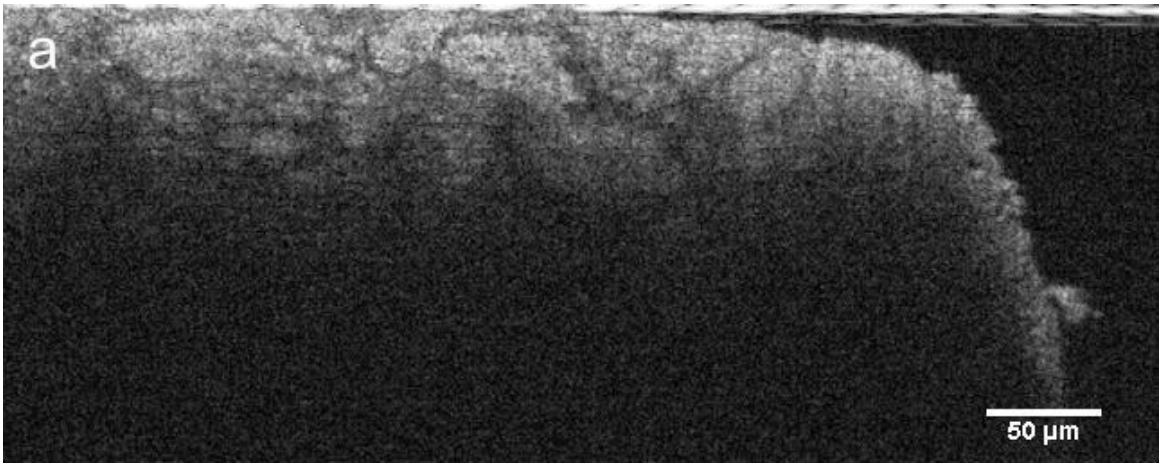

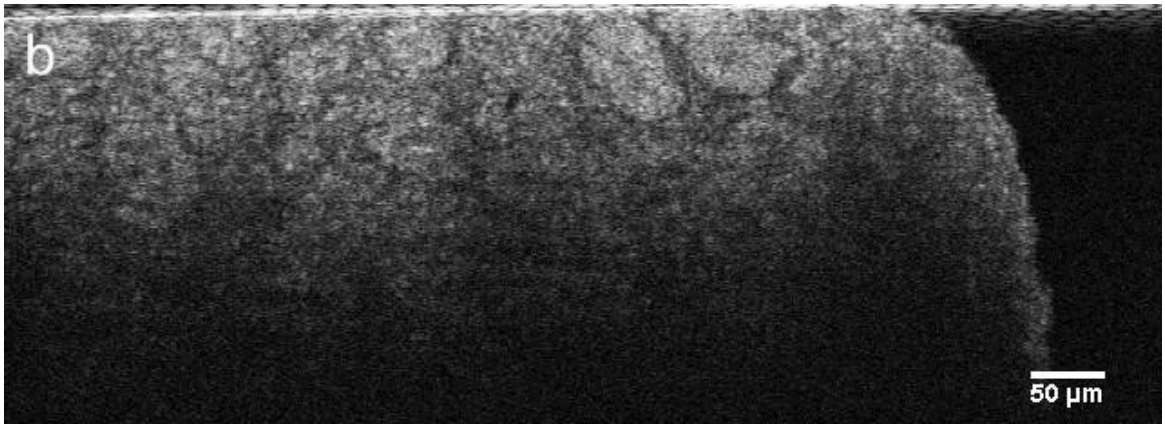

figure VI.8: Same sample cross-sectional view imaged with the infrared configuration (InGaAs camera). Image depth : 300µm.

A qualitative assessment confirms the expected increase in penetration depth in the near-infrared range (InGaAs camera) in comparison to the Si-camera based configurations.

OCT signal attenuation and penetration depth

[8] *benign lesion (noncancerous) characterized by fibrous and glandular tissue forming a lump.*

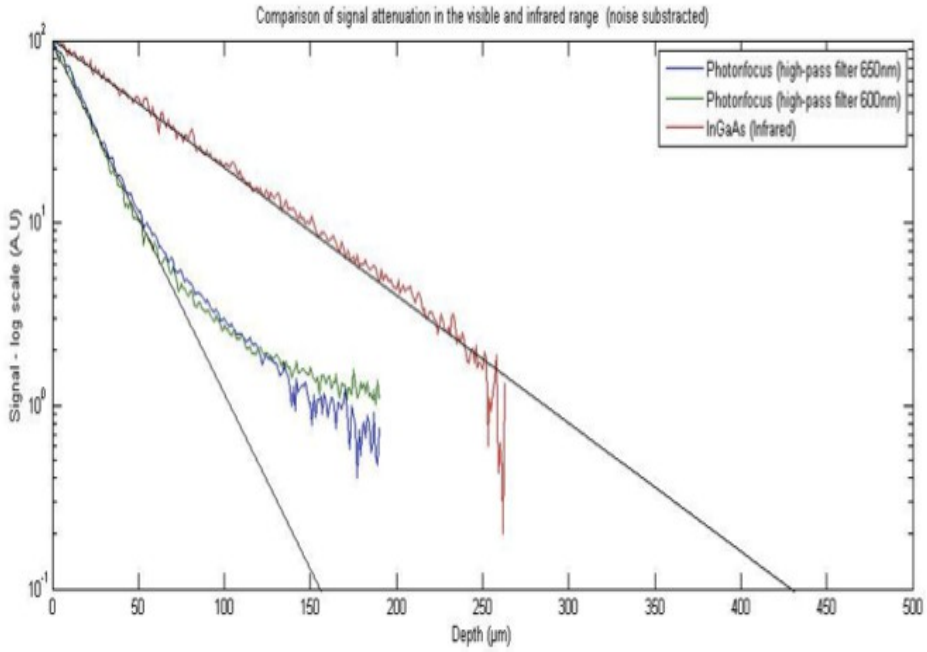

Figure VI.9: signal attenuation comparison relative to the spectral response of different detectors measured with fixed human breast tissue (fibroadenoma lesion). Divergence from the exponential attenuation indicates a multiple scattering regime according to the model demonstrated by Thrane [7].

As expected a significant increase in photons' mean free path is observed with the InGaAs configuration as shown on figure VI.9. The linear attenuation measure shows an approximately three-fold increase in penetration depth for the infrared system (red curve) in comparison to systems in the visible (blue and green curves). By replicating this measurement, a similar increase in penetration depth is observed with at least a factor two gain. For this particular tissue (i.e. fibroadenoma), the multiple scattering shown by the divergence from the linear signal attenuation [7], is quasi absent from the infrared curve up to 250 µm in depth while it already occurs at around 70 µm for the two systems in the visible range. From this result, a power law expressing the wavelength dependence can be extracted. The broadness of both spectra require the use of each central spectrum resulting in a power law dependence of λ^2 (2 order of magnitude) typical of Mie scattering regime.

VI.2.4 Discussion

The second part of this study aimed at assessing the penetration depth with an oil immersion medium and to evaluate the scattering components of the signal as a function of depth. As expected, results tend to show an increased penetration depth with the infrared configuration (InGaAs camera) compared to the two systems in the visible range (silicon cameras). However,

this can lead to an overestimate of the usable depth since resolution and contrast are critical factors in this assessment. In traditional OCT, imaging depth is usually perceived based on the sensitivity limit in which the signal falls to the noise floor. For the configuration in the visible range, the transition to the multiple scattering regime appears before the noise floor and therefore limits the depth at which ballistic, single scattering light can be probed. For the infrared setup, those results suggest a lesser proportion of multiple scattering and a predominance of ballistic photons detected with an almost factor 3 increase. While measurements among the three systems have not been adjusted to the relative full-well capacity and frame rate difference, the increased full-well capacity of the InGaAs camera is compensated by a higher frame rate for the Si-cameras. Furthermore, such difference does not influence the overall shape of the linear fit and therefore no specific adjustment was implemented.

Some technical conditions could be improved to fully benefit from the infrared spectrum. For example, the microscope objectives used in the experiment (10×, 0.3 NA, Olympus) were not optimized for the 1200 nm wavelength region. The transmission drops from 81% at 800 nm to 59% at 1200 nm. In addition, optical aberrations are corrected for visible light range, image contrast and resolution are therefore not optimal for higher wavelengths.

Finally, a major downside remains the cost of the gallium arsenide detector chip (InGaAs) compared to silicon-based detectors (e.g. CCD or CMOS sensors). An InGaAs camera, as the one used in this work, costs around 30,000 USD (approximately 25,000 EUR), five to ten-fold higher than silicon-based cameras.

VI.3 Conclusion

This study has been conducted to test the performance of an InGaAs camera optimized for imaging in the infrared region (900 – 1700 nm) and mounted onto a full-field OCT setup. This work confirms the increase in penetration depth achieved into biological tissues in comparison to traditional FFOCT imaging usually performed in the visible range. Measurements showed a minimum of a factor two increase in penetration depth with the near-infrared configuration and reduced multiple scattering effects. In addition, the replacement of water as immersion medium by silicone oil significantly lowers the absorption above the wavelength threshold of 1000–1100 nm. This allows to take full advantage of the near-infrared part of the polychromatic light source.

References

[1] J. A. Curcio and C. C. Petty, “The Near Infrared Absorption Spectrum of Liquid Water,” *Journal of the Optical Society of America*, vol. 41, no. 5, p. 302, May 1951.

[2] T. R. Hillman and D. D. Sampson, “The effect of water dispersion and absorption on axial resolution in ultrahigh-resolution optical coherence tomography,” *Optics Express*, vol. 13, no. 6, p. 1860, Mar. 2005.

[3] M. E. Brezinski et al., “Optical Coherence Tomography for Optical Biopsy : Properties and Demonstration of Vascular Pathology,” *Circulation*, vol. 93, no. 6, pp. 1206-1213, 1996.

[4] K. Bizheva et al., “Compact, broad-bandwidth fiber laser for sub-2-μm axial resolution optical coherence tomography in the 1300-nm wavelength region,” *Optics Letters*, vol. 28, no. 9, p. 707, May 2003.

[5] D. Sacchet, J. Moreau, P. Georges, and A. Dubois, “Simultaneous dual-band ultra-high resolution full-field optical coherence tomography,” *Optics Express*, vol. 16, no. 24, p. 19434, Nov. 2008.

[6] W. Drexler, *Optical Coherence Tomography: Technology and Applications (Google eBook)*. Springer, 2008, p. 1346.

[7] L. Thrane, “Optical Coherence Tomography : Modeling and Applications,” 2001.

[8] A. Aguirre and J. Fujimoto, “Advances in optical coherence tomography and microscopy for endoscopic applications and functional neuroimaging,” *Thesis*, 2008. p182–183 and 207-208.

General Conclusion

This thesis reports a combination of ex-vivo clinical studies, in-vivo biological imaging, and technological developments of a full-field OCT system. Overall, these studies demonstrated unprecedented image quality and resolution.

A major part of this work was to adapt a laboratory instrument to the clinical setting (from “bench to bedside”) by enabling a dialogue between clinicians, engineers and researchers. The initial study on ex-vivo breast lesions assessed the capability of FFOCT to image large areas (up to 1 cm²) and to accurately read for presence of relevant features of malignancy compared to the gold standard of histology. The biopsy study explored the feasibility of a compact prototype under clinical routine and time limitations. Both results highlighted the capacity to reveal tumour margin based on specific criteria such as loss of organized structures, change in shapes and scattering intensity variations. It also revealed the limitations of the technology. Despite an isotropic resolution close to 1.5 µm, important features for histopathologists were not visible such as individual nuclei usually revealed by staining. In addition, the learning process of image interpretation was underestimated though the first prospective and blinded study showed encouraging results for the accuracy of the technique.

A second aspect of this work was the improvement of the technique through new contrasts methods. To address the limitation of a weak endogenous cellular contrast, attenuation maps based on the scattering properties of a tissue would be an appealing idea but results suggest the opposite. The accuracy of attenuation coefficients is highly undermined by the heterogeneity of a biological tissue when examined at the micron-scale level. The difference of attenuation between normal, benign or malignant lesions appeared highly unreliable, although in part, this may have been due to the limited number of samples investigated. These results, although negative, should perhaps have been published to help future work to explore this more fully. This would have required a stronger statistical significance against the hypothesis that attenuation maps could be a relevant diagnostic criteria for tumour assessment. This is unfortunately a frequent bias [1–3]. As far as the second methodology is concerned, optical elastography holds greater prospects. However, individual cancerous cells and their biomechanical properties need to be more fully understood in order to extract valuable diagnostic information. Micron-scale resolution provides

both advantages and limitations compared to ultrasound or MRI elastography which can assess larger areas. At the cellular-level, malignant cells have highly heterogeneous viscoelastic properties that need to be taken into consideration.

A third aspect of this work was to improve the performance of the FFOCT system. This was done by implementing a new camera operating in the near-infrared range (900–1600 nm). The immersion medium was also replaced by silicone oil instead of water-based gel. This setup was shown to take full advantage of the large spectrum of the polychromatic light source by increasing the penetration depth by a minimum of a factor two. This gain was in accordance with diffusion models and showed a power law dependence of λ^2 (2 order of magnitude) typical of Mie scattering regime.

Finally, the in-vivo imaging capability of the technique was demonstrated during the four-days of metamorphosis of a Drosophila melanogaster. FFOCT was able to image the organ formation of a living organism at a depth of 80–100 µm with a micron-scale isotropic resolution. As a non-destructive optical method, the instrument overcomes the limitations of traditional high-resolution microscopy techniques which require either post-mortem slice reconstruction or can induce laser damage if performed in-vivo. This study marks progress toward potential applications in developmental biology.

Future perspectives

For now, FFOCT in its current configuration, presents a higher potential for research purposes. As shown in this work, research applications could include the in-vivo tracking of organ formations in small-animals. A variety of mutant phenotypes could be monitored during embryonic development or metamorphosis as demonstrated with Drosophila melanogaster. The aim would be to gain an in-vivo understanding of the dynamic processes taking place at the anatomical level of an organ. Smaller cluster of cells offering high inherent contrast (e.g. collagen filaments, chitin-protein matrix,...) could also be potential targets of in-vivo 3-D imaging.

Another potential area to explore include bio-banking applications from human biopsies. It could allow a swift triage of specimen collected without the need for time-consuming histology process or chemical staining. In general, the conservation of tissues in bio-banks seeks to avoid the destructive process of tissue staining and paraffin embedding for subsequent genetic exploration. Similarly, some tiny fragments extracted from fine-needle biopsies cannot risk the chemical staining process for conservation and further analysis.

Concerning a traditional clinical application, including tumour margin assessment during surgery or the replacement of frozen-sections analysis; additional specificity and sensitivity studies are needed. Despite the research interest that a new tool could provide or the high expectations hold by its promoters, objective criteria appear critical to measure a potential diagnostic utility. One such criteria could include the time required to enter a double-blinded study or to measure the sensitivity and specificity of the technology in comparison to the gold standard (e.g. histopathologic

diagnosis). Preliminary results detailed here are encouraging, but only repeated and concordant results by different research groups can ultimately lead to a wider adoption.

As of to date (early 2012), the commercial and clinical success of the parent technique, OCT, has only been achieved in the medical field of ophthalmology. This success is primarily due to the unique possibility offered by OCT to visualise the back of the eye in-vivo. For turbid media, the tremendous challenge encountered over the past 10 years to provide a pertinent diagnostic information to clinicians should raise concern about the current trend in OCT and FFOCT. In other words, is this trend technology-driven or problem-driven? In ophthalmology, the medical community needed a tool able to quantitatively measure the retinal nerve thickness, an information not provided by any other techniques.

Contrary to ex-vivo image acquisition, in-vivo probes or endoscopic approaches are clearly problem-driven improvements, since no 3-D information is available with confocal microscopy or with camera-based techniques. Naturally, the parent technique, OCT tend to shift its research priorities towards this goal. In that context, FFOCT could provide a remarkable advantage thanks to its high resolution and larger scanning surface. Innovative approaches have recently been tested at the laboratory with a rigid endoscopic probe [4]. Similarly, a dual fluorescence-FFOCT system is also under investigation and could prove an ideal instrument for research applications.

In definitive, for non-transparent biological tissues, it is essentially in the context of a problem-driven approach that research in FFOCT could provide a real medical advance. For now, applications for small animal imaging and in developmental biology hold greater prospects.

References

[1] U. Dirnagl and M. Lauritzen, “Fighting publication bias: introducing the Negative Results section.,” *Journal of cerebral blood flow and metabolism : official journal of the International Society of Cerebral Blood Flow and Metabolism*, vol. 30, no. 7, pp. 1263-4, Jul. 2010.

[2] J. P. A. Ioannidis, “Why most published research findings are false.,” *PLoS medicine*, vol. 2, no. 8, p. e124, Aug. 2005.

[3] K. Dwan et al., “Systematic review of the empirical evidence of study publication bias and outcome reporting bias.,” *PloS one*, vol. 3, no. 8, p. e3081, Jan. 2008.

[4] A. Latrive and A. C. Boccara, “In vivo and in situ cellular imaging full-field optical coherence tomography with a rigid endoscopic probe.,” *Biomedical optics express*, vol. 2, no. 10, pp. 2897-904, Oct. 2011.

Annexe: Résumé en Français

Table des Matières

Cette annexe constitue un résumé des principaux résultats de ces travaux de thèse. Il en demeure néanmoins volontairement à un niveau essentiellement déductif car le lecteur intéressé par plus de détails est invité à se reporter au chapitre correspondant du manuscrit.

Contexte et problématique

La tomographie par cohérence optique ou OCT (pour Optical Coherence Tomography) est devenue en moins d'une quinzaine d'années une technique incontournable pour le diagnostic des pathologies de la rétine. Le succès médical et commercial obtenu pour un tissu transparent comme le globe oculaire s'est naturellement accompagné du même espoir pour les tissus diffusants, et ce dès les premiers pas de l'OCT dans les années 90 [1–5]. Dès lors, l'OCT a connu une effervescence exponentielle, et n'a cessé de voir de nouvelles approches et variantes se développer. La technique d'OCT plein-champ issue du laboratoire d'optique de l'ESPCI[9] et développée depuis une dizaine d'années s'inscrit dans ce contexte avec pour but d'apporter une

[9] *Pour* École Supérieure de Physique et Chimie de Paris.

information diagnostique pertinente: un véritable défi pluridisciplinaire pour opticiens, ingénieurs et médecins.

Au cours de ces travaux de thèse nous avons ainsi cherché à nous affranchir des mécanismes physiques qui limitent la qualité des images comme la diffusion des tissus, à optimiser les dispositifs existants, à en développer de nouveaux et en améliorer les performances à partir de données obtenues en conditions opératoires. Ces travaux ont contribué à initier la phase clinique de la tomographie par cohérence optique plein champ (FFOCT) et à la situer avec plus de précision dans le contexte de l'imagerie biomédicale.

Principes et État de l'art en OCT dans les milieux biologiques

Le premier chapitre situe les deux techniques d'OCT (conventionnel et plein-champ) par rapport aux méthodes d'imagerie médicales existantes, entre d'une part l'imagerie à ultrasons et la microscopie confocale à haute résolution. L'OCT peut être comparé à une échographie optique, or pour s'affranchir de la limite mécanique imposée par la vitesse de la lumière, le faisceau incident est séparé en deux, au moyen d'un montage reproduisant un interféromètre de Michelson. L'information utile est ainsi fournie en modulant la différence de marche entre le bras de référence et le bras objet. Cette méthode d'acquisition est communément appelé Time-Domain OCT (TD-OCT) du fait du balayage temporel du miroir référence. Une variante permet d'éviter ce balayage mécanique en se plaçant dans l'espace de Fourrier conjugué par une mesure parallèle du signal interférométrique. En effet, les différences d'indices sont déjà incluses dans les fréquences du spectre du signal d'interférence, on parle alors de Spectral ou Fourrier-Domain OCT dont l'avantage principal est le gain en temps lors de l'acquisition [6–8].

Dû fait de la faible résolution de l'OCT traditionnel (2–15 µm), une tendance actuelle est le retour aux méthodes d'OCT à haute résolution (OCM ou Optical Coherence Microscopy, OCT "plein-champ") [9–13]. Pour les applications biomédicales, il s'agit essentiellement de montages endoscopiques ou par sondes [14–24], d'avancées en Doppler-OCT [25–27] ou bien encore les tentatives de couplage acousto-optiques [28], [29], et d'amélioration du contraste au moyen de nanoparticules magnétiques [30–33], ou par élastographie optique [34–38].

Nous décrivons ensuite les outils nécessaire à la compréhension de l'interaction de la lumière avec les tissus biologiques, en fonction de la taille des structures rencontrées. Dans un milieu biologique, les photons sont principalement atténués par la diffusion, μ_s. L'autre composante, l'absorption, μ_a ne contribue que pour une fraction de l'atténuation du faisceau incident mais augmente fortement avec la longueur d'onde, du fait notamment des bandes d'absorption du spectre de l'eau, constituant principal des tissus biologiques.

Dispositifs d'OCT « plein-champ »

Contrairement à l'OCT classique, l'approche plein-champ évite tout balayage mécanique du faisceau par une acquisition parallèle de l'image au moyen d'un détecteur de type caméra CCD ou CMOS[10]. De plus, une simple lampe halogène à filament de tungstène est utilisée comme source d'illumination, un avantage notable par rapport aux systèmes lasers complexes et coûteux souvent utilisés en OCT traditionnel.

Une autre particularité est que deux objectifs sont montés sur chaque bras de l'interféromètre afin d'améliorer la résolution latérale du dispositif, qui dépend ainsi directement de l'ouverture numérique et de la longueur d'onde employée. Et contrairement à la microscopie confocale, où la résolution axiale est dictée par l'ouverture numérique des objectifs, ici la résolution en profondeur est essentiellement déterminée par la largeur du spectre effectif et la longueur d'onde centrale de la source lumineuse. L'image finale correspond en chaque voxel à une tranche de virtuelle résultant des interférences des photons balistiques ou mono-diffusés, volume inversement proportionnel à la la largeur du spectre de la source, à une demi-longueur de cohérence près. Une lumière polychromatique dite faiblement cohérente, permet par exemple d'extraire une tranche virtuelle, Δz de l'ordre du micron pour un spectre effectif centré autour de 700-800 nm et une largeur de bande d'environ 125-150 nm. Il faut souligner que le spectre effectif est essentiellement limité par la réponse spectrale de la caméra CCD ou CMOS en Silicium (pour des capteurs en Arséniure de Gallium et d'Indium, voir dispositif infrarouge plus bas).

Le second chapitre détaille ainsi le dispositif d'OCT "plein-champ" utilisé au cours de ces travaux et inclus les ajustements techniques apportés afin d'aboutir à un système robuste pour une utilisation en routine clinique sous différentes contraintes, notamment de temps et de praticité. Cette phase a surtout été menée en collaboration avec l'équipe de LLTech, start-up issue du laboratoire, dont le plein démarrage a eu lieu en même temps que cette thèse. Une part notable de la conduite du projet de recherche a ainsi consisté à établir un dialogue entre cliniciens, ingénieurs et chercheurs, sans oublier les décideurs. L'aspect technique s'avère parfois être le plus simple à résoudre si les attentes de chaque interlocuteur coïncident. Il a donc fallu cadrer les attentes des cliniciens, participer aux réunions internes et éclairer sur les pistes à fort potentiel, ou au contraire moins réalistes. Cet aspect central du projet de recherche doctoral a contribué en partie à l'amélioration de l'interface utilisateur du logiciel de contrôle, à fournir des idées pour la conception d'un porte-échantillon adapté à une routine clinique, ou bien encore à la réalisation d'un projet de recherche innovant en biologie du développement (application non envisagée en début de thèse) et détaillé plus bas. Finalement, une innovation simple mais critique au prototype clinique fut le remplacement du gel échographique par une huile de synthèse (silicone) offrant une plus grande résistance à l'évaporation tout en maintenant un indice proche de celui des lames de silices (n = 1.40–1.41); le mérite revient à l'équipe de LLTech.

[10] *CMOS pour Complementary Metal–Oxide–Semiconductor et CCD pour Charge-Coupled Device.*

Le chapitre 6 présente un nouveau dispositif expérimental développé en vue d'améliorer la profondeur de pénétration et d'étudier l'influence de la gamme spectrale du proche infrarouge dans des milieux biologiques fortement diffusants. L'objectif étant de tirer pleinement avantage du spectre effectif de la lampe halogène en élargissant la réponse spectrale par le remplacement d'un capteur caméra non plus en Silicium mais en Arséniure d'Indium et de Gallium (InGaAs).

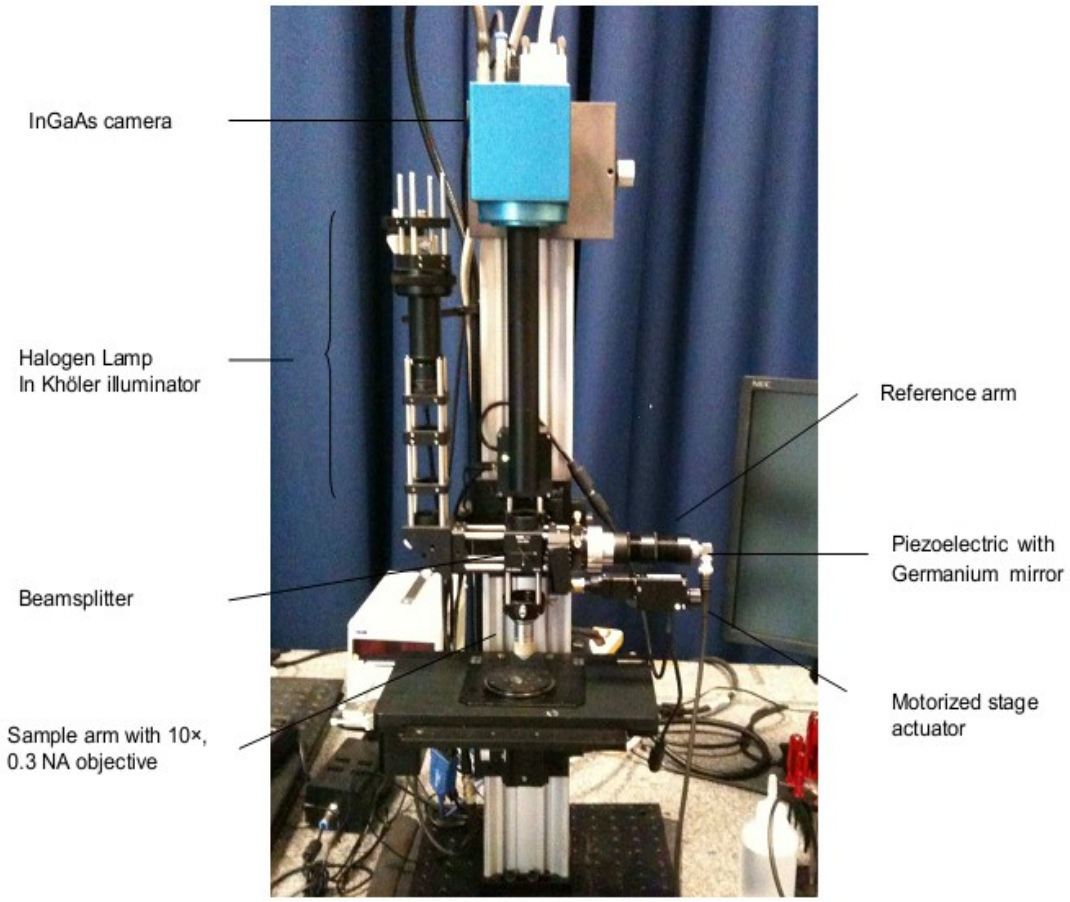

Le spectre effectif obtenu atteint une largeur de bande, Δλ de 600 nm centrée au voisinage de 1225 nm, et permet ainsi, au minimum un doublement de la profondeur de pénétration dans les tissus par rapport aux dispositifs opérants dans le visible comme le montrent les figures 2,3 et 4.

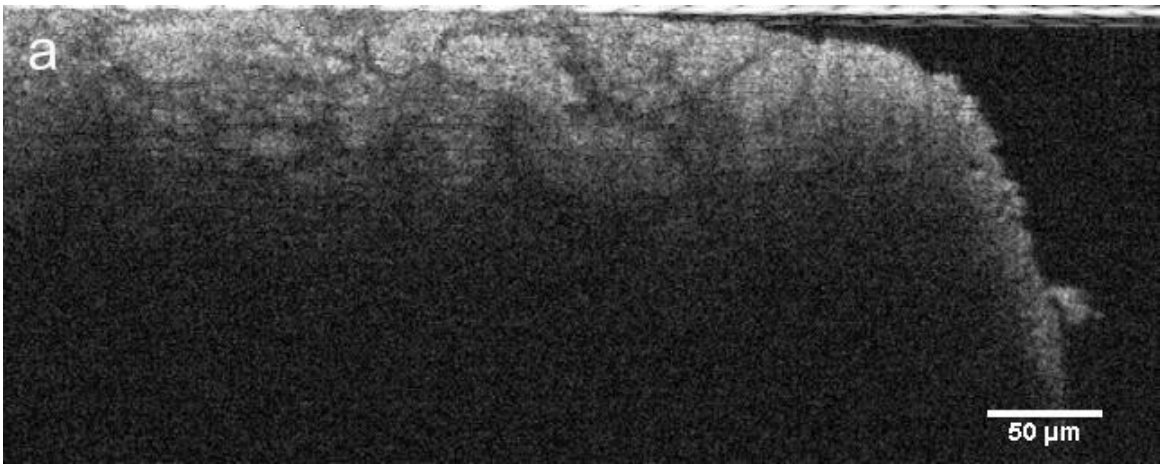
a
50 µm

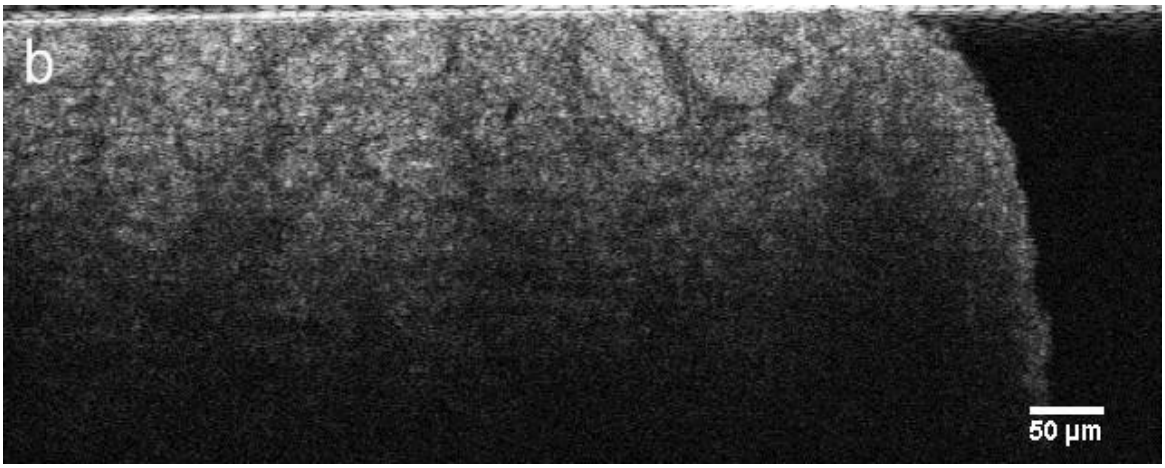
b
50 µm

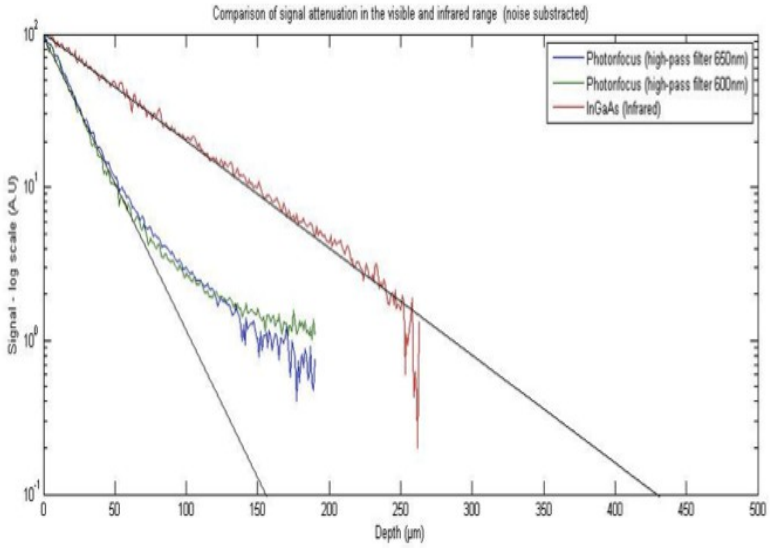
Comparison of signal attenuation in the visible and infrared range (noise substracted)
Photonfocus (high-pass filter 650nm)
Photonfocus (high-pass filter 600nm)
InGaAs (Infrared)
Signal - log scale (A.U)
Depth (µm)

Ce gain en profondeur de pénétration, d'au minimum un facteur deux, est en accord avec les modèles de diffusion et met en évidence une diffusion caractéristique du régime de Mie pour des tissus biologiques. Le coût de la caméra InGaAs demeure néanmoins une limitation majeure pour une utilisation clinique et commerciale.

Étant donné la maturité de la technique sur le plan de l'instrumentation, l'enjeu du projet de recherche s'est porté sur la phase d'application clinique et l'évaluation d'outils quantitatifs innovants.

Etudes cliniques sur lésions mammaires et biopsies

Deux études collaboratives ont été menées au cours de ces travaux, l'une réalisée en laboratoire sur tissus frais et fixés et la seconde en conditions de routine clinique. Les résultats présentés se concentrent essentiellement sur les lésions de tissus mammaires et une analyse de biopsies rénales (voir figure 5 et 6).

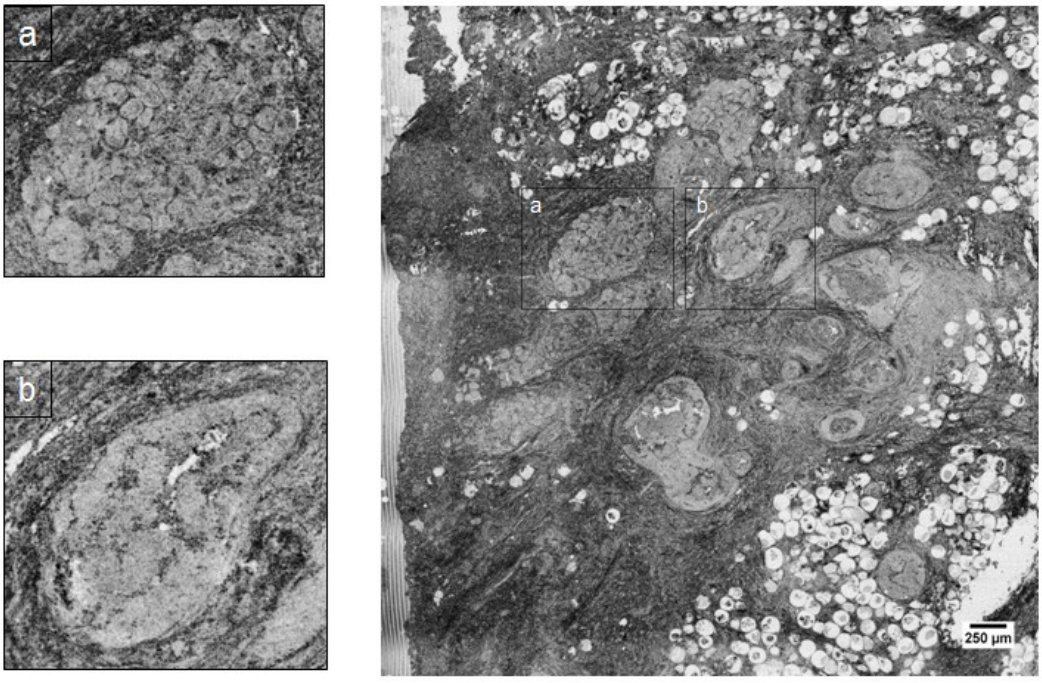

L'objectif initial était d'établir une grille d'analyse diagnostique des images OCT à partir de lames histologiques du même échantillon. Le second objectif visait à évaluer la faisabilité du dispositif en véritables conditions de routine clinique. Un protocole de préparation et de fixation des tissus a ainsi été établi et validé.

De même, une première grille d'analyse des images OCT a pu être constituée en collaboration avec les anatomopathologistes de l'institut Curie et de l'hôpital Tenon à Paris. Les résultats ont mis en évidence la capacité du système à scanner une large surface d'environ 1 cm^2 au moyen d'un algorithme optimisé pour l'assemblage des images.

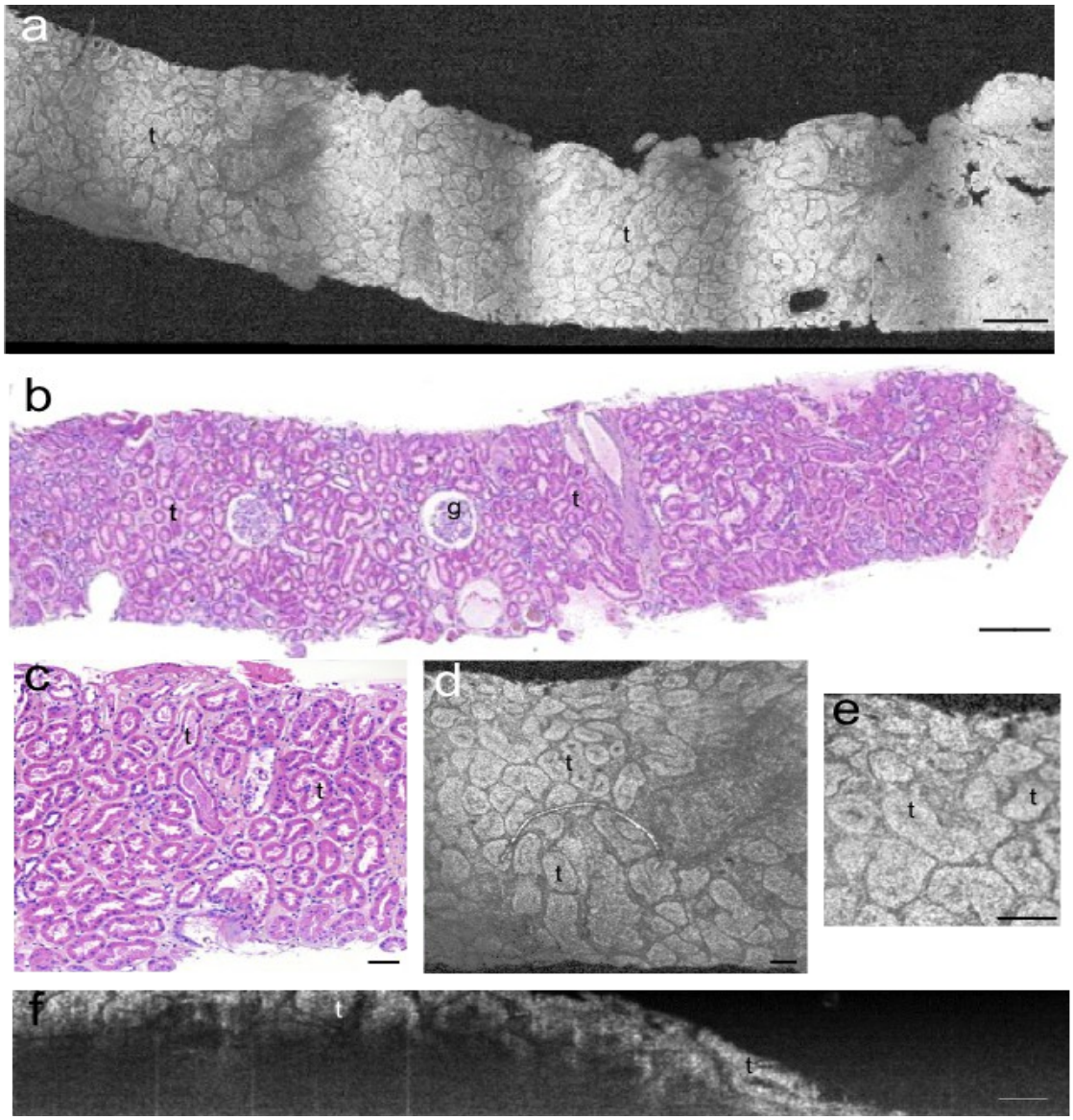

Figure 6: Images OCT plein-champ d'une biopsie d'adénome rénal (a,d,e,f) et images histologiques correspondantes (lésion bénigne). Les structures de formes ovoide (t) sont des sections de tubes proximaux et distaux en section transversale. Seule l'image FFOCT (f) représente une coupe axiale sur une profondeur de 150 µm. Les tubes rénaux sont visibles jusqu'à une profondeur d'environ 80-100 µm. Les glomérules (g) visibles en coupe histologiques ne sont pas présents sur les sections tomographiques. Les bandes noires sont dues à l'algorithme d'assemblage (stiching) des vignettes individuelles. Barres d'échelles: 250 µm (a,b) et 70 µm (c,d,e,f).

Les résultats des deux études ont permis de révéler les zones tumorales selon des critères tels que la forme et l'architecture interne du tissu ou les variations d'intensité de diffusion. De plus,

le dispositif s'est avéré fiable et adapté à une acquisition d'image en moins de 20 minutes (délai total entre le prélèvement et l'affichage final à l'écran). Délais comparables à l'examen en extemporanée (ou « frozen-section»)[11] pratiqué par certains centres dans les cas notamment de lésions opérables du sein.

Toutefois plusieurs limitations subsistent comme par exemple un contraste structurel faible en dépit des inhomogénéités multiples des tissus biologiques, limitant ainsi la distinction précise entre tissu sain, bénin ou malin. Néanmoins, ces travaux ont abouti à la première étude multicentrique en OCT plein champ. Après une phase d'apprentissage, où images OCT et coupes histologiques correspondantes sont passées en série, la phase "en aveugle" a abouti à des taux moyens de sensibilité (lésion maligne véritablement présente) de 93.5% et à une spécificité de 75.5% (lésion maligne véritablement absente).

Pistes d'amélioration du contraste endogène

Le quatrième chapitre explore deux voies possibles d'amélioration du contraste, l'une basée sur le contraste d'atténuation et l'autre à partir des propriétés d'élasticité du tissu. L'hypothèse se fonde sur le principe qu'un tissu tumoral ou fibreux doit plus fortement atténuer le faisceau de photons reçu qu'un tissu sain. En théorie, l'idée semble attrayante et quelques résultats encourageants apparaissent dans la littérature en OCT traditionnel [39–44]. Toutefois, les résultats obtenus dans notre étude, et répliqués par un autre chercheur, tendent à indiquer le contraire en OCT plein-champ.

La méthode employée se base sur la loi de Beer-Lambert de décroissance exponentielle de l'intensité du flux lumineux rétrodiffusé par l'échantillon. Or, la différence de coefficients d'atténuation entre tissus sain, bénin et tumoral s'avère ne pas fournir un critère quantitatif fiable. Par exemple, les écarts types de plusieurs catégories de tissus ou de lésions se recouvrent fréquemment, limitant de ce fait toute tentative de cartographie d'une pathologie spécifique. Un des facteur mis en évidence dans cette étude est la très forte hétérogénéité du tissu à l'échelle de quelque microns de profondeur comme le montre la figure 7.

[11] procédé qui permet une mise en lame en moins de 30 minutes en cours d'opération chirurgical et qui conditionne l'attitude thérapeutique immédiate pendant l'anesthésie du patient.

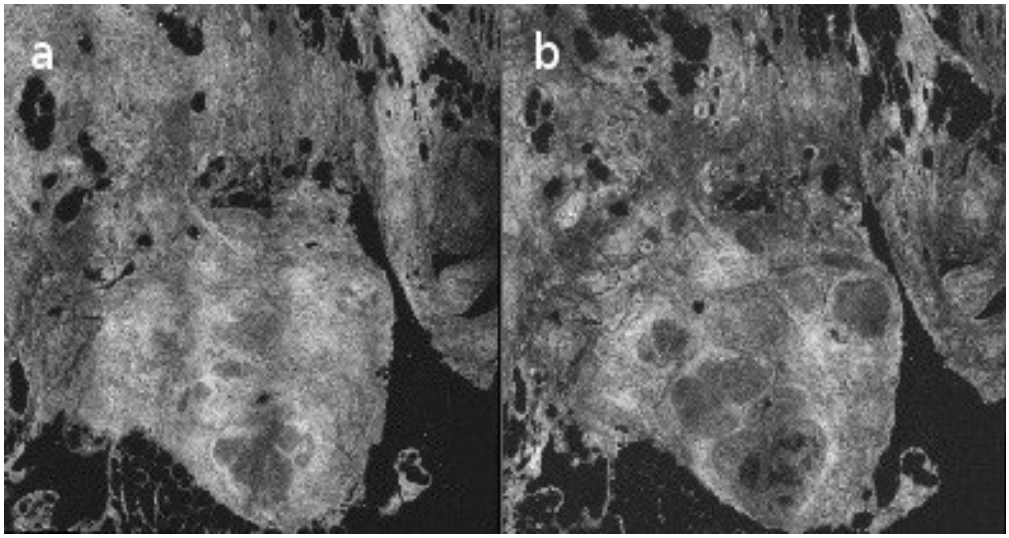

Figure 7: Lésion mammaire à 10 et 25 µm en profondeur images a) and b) respectivement. Plusieurs structures épithéliales et canaux hyperplasiés apparaissent en l'espace de 15 µm.

Des structures différentes en terme de coefficient d'atténuation apparaissent en l'espace de quelques microns. Cette situation pourrait s'assimiler aux cas de "volume partiel" que l'on rencontre pour d'autres techniques d'imagerie telles que l'IRM ou le Scanner X et qui peuvent induire en erreur lors du diagnostic. Pour une obtenir une carte d'atténuation, cela nécessite une automatisation des mesures, or comme le montre la figure 7, les coefficients de diffusions des structures épithéliales sont très différentes du tissu de soutien faussant ainsi la précision des mesures. Une solution qui pourrait être envisagée serait l'application d'algorithmes de segmentation afin de différencier l'interface entre deux tissus au micron près, cette option risque toutefois d'être confrontée aux contraintes de temps d'une utilisation clinique. Cette étude semble ainsi indiquer que la haute résolution axiale fournit par l'OCT plein champ peut apparaître en pratique comme un avantage limitant au détriment de l'OCT classique offrant une plus grande profondeur de pénétration et donc une mesure moins bruitée par des variations de l'ordre du micromètre. Une limite de cette étude reste néanmoins la taille réduite de l'échantillonnage qui peut diminuer la fiabilité statistique des résultats.

Le second contraste intrinsèque examiné apparaît plus prometteur, même s'il s'agit que d'une première étude de faisabilité. La méthodologie se base quant à elle sur l'hypothèse d'une différence de dureté ou d'élasticité entre tissus sains et malins [45–49]. L'objectif est de transposer à l'optique la méthode d'élastographie utilisée avec succès en ultrasons et cela à l'échelle du micron. Une plate-forme spécifique a été conçue afin de pouvoir appliquer différentes déformations aux tissus imagés et ainsi mesurer une élastographie statique après retour à l'état transitoire. Une cartographie des déplacements induits pour chaque structure interne a pu ainsi être obtenue. Les premiers résultats s'avèrent prometteurs et un nouveau projet de recherche doctoral a pris le relais pour approfondir cette piste. L'objectif est notamment d'évoluer vers une méthodologie dynamique

ou élastographie transitoire en appliquant une source vibratoire continue. Plusieurs limites ont toutefois été clairement identifiées lors de ces travaux. Les tissus biologiques présentent une combinaison de composants élastiques et visqueux qui nécessitent une cartographie 3D des déformations et non de simples carte 2D comme dans la présente étude. De même, une meilleure compréhension des propriétés visco-élastiques des cellules cancéreuses individuelles s'avère nécessaire en vue d'une application clinique. A l'échelle du micron, de nombreuses cellules présentent des propriétés biomécaniques inattendues, telles qu'une viscoelasticité considérablement réduite qui pourrait s'expliquer par la nécessité d'infiltrer le tissu de soutien et se répandre vers le système circulatoire [50], [51].

Quant aux méthodes de corrélations employées, ces travaux ont révélé la complexité du choix de la fenêtre d'interrogation pour les mesures de variance. Une fenêtre trop large fausse les corrélations et inversement. Ce critère pourrait être lié au paramètre précédent, à savoir, le type de cellules cancéreuses observées et fonction affine de la déformation appliquée. Comparé aux méthodes d'élastographie par ultrasons ou IRM sur des zones de plusieurs centimètres, à l'échelle cellulaire, nous avons montré que de nouvelles contraintes apparaissent qui nécessitent d'être prises en compte.

Avancées en biologie : imagerie in-vivo du cycle d'une métamorphose

Finalement, nous avons réalisé une application unique à l'OCT plein champ : le suivi de l'organogenèse de la D*rosophila melanogaster* et ceci sur l'ensemble des 100h de métamorphose. Les techniques comparables sont soient limitées par la résolution spatiale (IRM du petit animal à haut champ) ou soit par la complexité de maintenir l'insecte vivant sur une telle durée. L'approche traditionnelle requiert de ce fait la fixation en résine de l'insecte à chaque étape du développement, procédure particulièrement astreignante [52–54].

Afin d'aboutir à une imagerie in-vivo de l'insecte, plusieurs facteurs déterminants ont pu être identifiés, tels que la préparation de l'animal au moyen d'une fine couche d'huile d'olive ou bien encore la pression du porte-échantillon pour maintenir une aération adéquate. De même, un contrôle précis de l'illumination a permis d'éviter toute déshydratation pendant les 4 jours de la métamorphose. Les résultats ont ainsi pu mettre en évidence l'évolution au cours du temps des disques imaginaux de la pupe (fin de stade larvaire) jusqu'à la formation finale de la mouche adulte avant son éclosion. La figure 8 montre cette évolution sur une période de 72h pour trois profondeurs différentes.

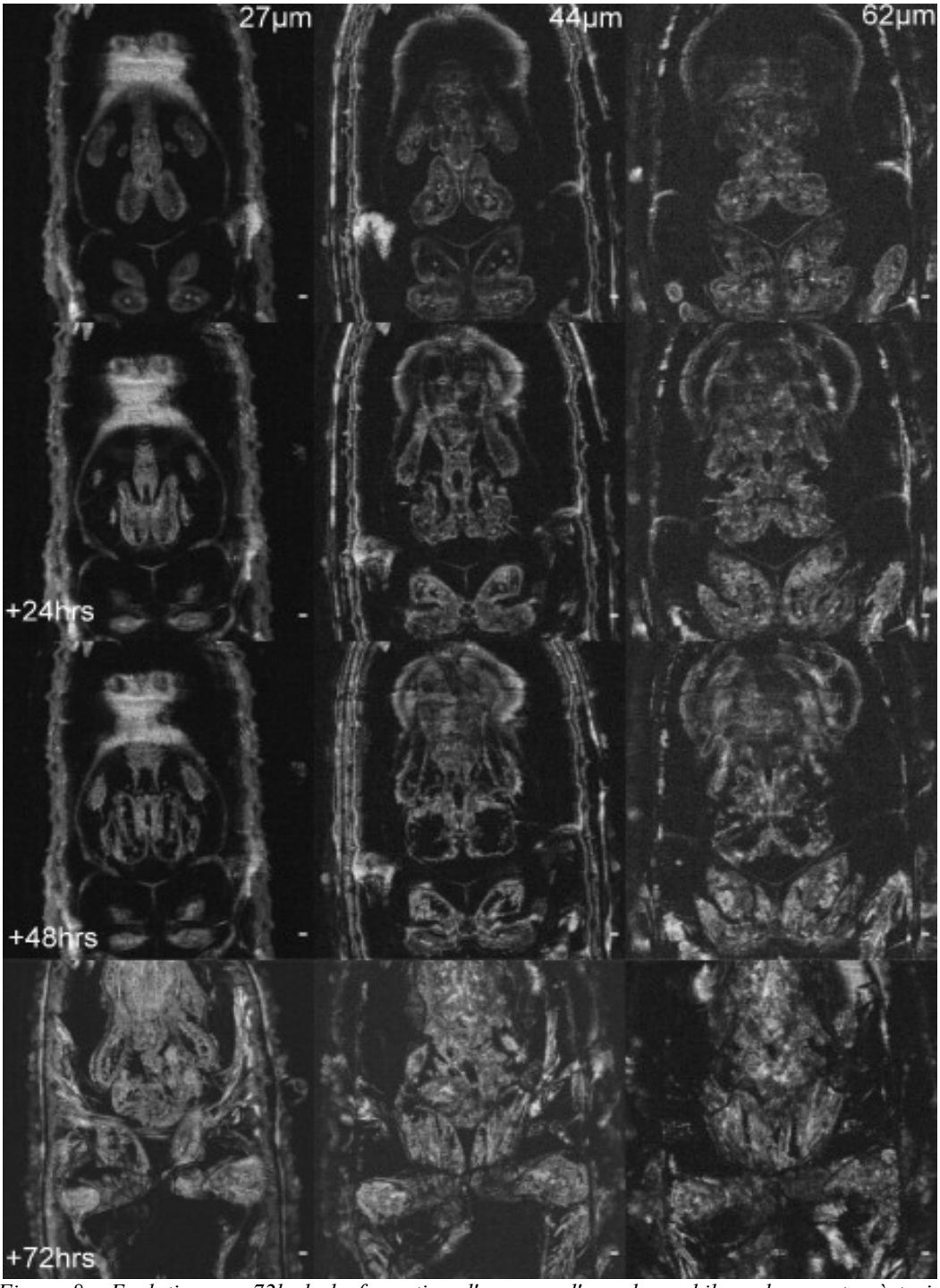

Figure 8: Evolution sur 72h de la formation d'organes d'une drosophile melanogaster à trois profondeurs différentes (en colonne). Jeune pupe en fin de phase larvaire (haut) jusqu'à la pupe quasi adulte avant éclosion (bas). On distingue la différentiation des disques imaginaux en organes complètement développés. La partie supérieure montre l'évolution du disque oeil-antenne (visible à 62µm), et la partie inférieure correspond aux disques imaginaux des membres inférieurs.

Une application potentielle serait le suivi de phénotypes mutants afin d'évaluer, par exemple, l'organogenèse de modèles de dégénérescence musculaire ou de mutations du système

optique chez la *Drosophile* melanogaster. Toutefois, la profondeur de pénétration reste limitée (environ 100-150 µm) et cela sur les deux dispositifs (visible et proche infrarouge) excluant tout imagerie du système nerveux (situé au-dessous du système optique). De plus, un suivi par agents de contraste en fluorescence serait un développement essentiel pour une adoption plus large de la technique en vue d'une application de routine en biologie. A ce titre, un projet de recherche doctoral étudie actuellement la possibilité de combiner imagerie de fluorescence et OCT plein-champ.

Ce manuscrit présente ainsi l'essentiel des projets de recherche menés au cours de cette thèse et visant à améliorer les performances diagnostiques de l'OCT plein champ en vue d'une application clinique. L'apport de ces travaux est d'avoir à la fois fourni de nouveaux champs d'applications mais aussi d'avoir développé et mis en évidence la validité ou non des améliorations proposées.

References

[1] D. Huang et al., “Optical coherence tomography,” *Science*, vol. 254, no. 5035, pp. 1178-1181, Nov. 1991.

[2] J. A. Izatt, M. D. Kulkarni, S. Yazdanfar, J. K. Barton, and A. J. Welch, “In vivo bidirectional color Doppler flow imaging of picoliter blood volumes using optical coherence tomography,” *Optics Letters*, vol. 22, no. 18, pp. 1439-1441, 1997.

[3] S. Yazdanfar, M. Kulkarni, and J. Izatt, “High resolution imaging of in vivo cardiac dynamics using color Doppler optical coherence tomography,” *Optics Express*, vol. 1, no. 13, pp. 424-431, Dec. 1997.

[4] Paul J. Tadrous, “Methods for imaging the structure and function of living tissues and cells: 1. Optical coherence tomography,” *The Journal of Pathology*, vol. 191, no. 2, pp. 115-119, 2000.

[5] I.-K. Jang et al., “Visualization of coronary atherosclerotic plaques in patients using optical coherence tomography: comparison with intravascular ultrasound,” *Journal of the American College of Cardiology*, vol. 39, no. 4, pp. 604-609, Feb. 2002.

[6] R. Leitgeb, C. Hitzenberger, and A. Fercher, “Performance of fourier domain vs time domain optical coherence tomography,” *Optics Express*, vol. 11, no. 8, p. 889, Apr. 2003.

[7] M. Choma, M. Sarunic, C. Yang, and J. Izatt, “Sensitivity advantage of swept source and Fourier domain optical coherence tomography,” *Optics Express*, vol. 11, no. 18, pp. 2183-2189, 2003.

[8] B. E. Bouma, S.-H. Yun, B. J. Vakoc, M. J. Suter, and G. J. Tearney, “Fourier-domain optical coherence tomography: recent advances toward clinical utility.,” *Current opinion in biotechnology*, vol. 20, no. 1, pp. 111-8, Feb. 2009.

[9] C. Zhou et al., “Ex vivo imaging of human thyroid pathology using integrated optical coherence tomography and optical coherence microscopy.,” *Journal of biomedical optics*, vol. 15, no. 1, p. 016001, 2010.

[10] H.-C. Lee et al., “Integrated Optical Coherence Tomography and Optical Coherence Microscopy Imaging of Ex Vivo Human Renal Tissues.,” *The Journal of urology*, Dec. 2011.

[11] R. Lee, “Cellular resolution optical coherence microscopy with high acquisition speed for in-vivo human skin volumetric imaging,” *Optics Letters*, no. May, 2011.

[12] P. Onlinefirst, “Title: Integrated Optical Coherence Tomography and Microscopy for,” *Cancer Research*, 2010.

[13] D. Sacchet, J. Moreau, P. Georges, and A. Dubois, “Simultaneous dual-band ultra-high resolution full-field optical coherence tomography,” *Optics Express*, vol. 16, no. 24, p. 19434, Nov. 2008.

[14] B. J. F. Wong et al., “In vivo optical coherence tomography of the human larynx: Normative and benign pathology in 82 patients,” *Laryngoscope*, vol. 115, no. 11, pp. 1904-1911, 2005.

[15] B. C. Quirk, R. A. McLaughlin, A. Curatolo, R. W. Kirk, P. B. Noble, and D. D. Sampson, “In situ imaging of lung alveoli with an optical coherence tomography needle probe,” *Journal of Biomedical Optics*, vol. 16, no. 3, p. 036009, Mar. 2011.

[16] J. M. Ridgway et al., “In Vivo Optical Coherence Tomography of the Human Oral Cavity and Oropharynx,” *Arch Otolaryngol Head Neck Surg*, vol. 132, no. 10, pp. 1074-1081, Oct. 2006.

[17] J. M. Ridgway et al., “Imaging of the pediatric airway using optical coherence tomography,” *Laryngoscope*, vol. 117, no. 12, pp. 2206-2212, 2007.

[18] J. M. Ridgway et al., “Optical coherence tomography of the newborn airway,” *Annals of Otology, Rhinology and Laryngology*, vol. 117, no. 5, pp. 327-334, 2008.

[19] Y. Chen et al., “Effects of axial resolution improvement on optical coherence tomography (OCT) imaging of gastrointestinal tissues,” *Optics Express*, vol. 16, no. 4, pp. 2469-2485, 2008.

[20] A. Latrive and A. C. Boccara, “In vivo and in situ cellular imaging full-field optical coherence tomography with a rigid endoscopic probe.,” *Biomedical optics express*, vol. 2, no. 10, pp. 2897-904, Oct. 2011.

[21] J. A. Evans et al., “Identifying intestinal metaplasia at the squamocolumnar junction by using optical coherence tomography,” *Gastrointestinal Endoscopy*, vol. 65, no. 1, pp. 50-56, Jan. 2007.

[22] B. J. Vakoc et al., “Comprehensive esophageal microscopy by using optical frequency-domain imaging (with video),” *Gastrointestinal Endoscopy*, vol. 65, no. 6, pp. 898-905, May 2007.

[23] A. M. Zysk et al., “Clinical feasibility of microscopically-guided breast needle biopsy using a fiber-optic probe with computer-aided detection,” *Technology in Cancer Research & Treatment*, vol. 8, no. 5, pp. 315-321, Oct. 2009.

[24] C. Zhou et al., “Ex vivo imaging of human thyroid pathology using integrated optical coherence tomography and optical coherence microscopy,” *Journal of Biomedical Optics*, vol. 15, no. 1, p. 016001, Feb. 2010.

[25] E. Koch, J. Walther, and M. Cuevas, “Limits of Fourier domain Doppler-OCT at high velocities,” *Sensors and Actuators A: Physical*, vol. In Press, .

[26] A. H. Bachmann, M. L. Villiger, C. Blatter, T. Lasser, and R. A. Leitgeb, “Resonant Doppler flow imaging and optical vivisection of retinal blood vessels,” *Optics Express*, vol. 15, no. 2, pp. 408-422, Jan. 2007.

[27] V. Westphal, S. Yazdanfar, A. M. Rollins, and J. A. Izatt, “Real-time, high velocity-resolution color Doppler optical coherence tomography,” *Optics Letters*, vol. 27, no. 1, pp. 34-36, Jan. 2002.

[28] S. Farahi, G. Montemezzani, A. a Grabar, J.-P. Huignard, and F. Ramaz, “Photorefractive acousto-optic imaging in thick scattering media at 790 nm with a Sn(2)P(2)S(6):Te crystal.,” *Optics letters*, vol. 35, no. 11, pp. 1798-800, Jun. 2010.

[29] S. G. Resink, W. Steenbergen, and A. C. Boccara, “State-of-the art of acoust-optic sensing and imaging of turbid media,” *Journal of Biomedical Optics*, vol. 17, no. 4, p. 040901, Apr. 2012.

[30] R. John et al., “In vivo magnetomotive optical molecular imaging using targeted magnetic nanoprobes.,” *Proceedings of the National Academy of Sciences of the United States of America*, vol. 107, no. 18, pp. 8085-90, May 2010.

[31] X. Liang, M. Orescanin, K. S. Toohey, M. F. Insana, and S. A. Boppart, “Acoustomotive optical coherence elastography for measuring material mechanical properties,” *Optics Letters*, vol. 34, no. 19, pp. 2894-2896, Oct. 2009.

[32] A. L. Oldenburg, V. Crecea, S. A. Rinne, and S. A. Boppart, “Phase-resolved magnetomotive OCT for imaging nanomolar concentrations of magnetic nanoparticles in tissues,” *Optics Express*, vol. 16, no. 15, pp. 11525-11539, 2008.

[33] A. L. Oldenburg, S. A. Boppart, V. Crecea, and X. Liang, “MAGNETOMOTIVE OPTICAL COHERENCE TOMOGRAPHY.” 2009.

[34] W. A. Berg et al., “Shear-wave elastography improves the specificity of breast US: the BE1 multinational study of 939 masses.,” *Radiology*, vol. 262, no. 2, pp. 435-49, Feb. 2012.

[35] Y. Zhao et al., “Integrated multimodal optical microscopy for structural and functional imaging of engineered and natural skin.,” *Journal of biophotonics*, Feb. 2012.

[36] B. F. Kennedy et al., “In vivo three-dimensional optical coherence elastography,” *Optics Express*, vol. 19, no. 7, p. 6623, Mar. 2011.

[37] C. Sun, “Optical coherence elastography: current status and future applications,” *Journal of Biomedical Optics*, 2011.

[38] S. G. Adie, B. F. Kennedy, J. J. Armstrong, S. A. Alexandrov, and D. D. Sampson, “Audio frequency in vivo optical coherence elastography.,” *Physics in medicine and biology*, vol. 54, no. 10, pp. 3129-39, May 2009.

[39] L. Scolaro et al., “Parametric imaging of the local attenuation coefficient in human axillary lymph nodes assessed using optical coherence tomography.,” *Biomedical optics express*, vol. 3, no. 2, pp. 366-79, Feb. 2012.

[40] E. Cauberg and D. de Bruin, “Quantitative measurement of attenuation coefficients of bladder biopsies using optical coherence tomography for grading urothelial carcinoma of the bladder,” *Journal of Biomedical …*, 2010.

[41] P. H. Tomlins, O. Adegun, E. Hagi-Pavli, K. Piper, D. Bader, and F. Fortune, “Scattering attenuation microscopy of oral epithelial dysplasia.,” *Journal of biomedical optics*, vol. 15, no. 6, p. 066003, Jan. 2010.

[42] R. a McLaughlin, L. Scolaro, P. Robbins, C. Saunders, S. L. Jacques, and D. D. Sampson, “Mapping tissue optical attenuation to identify cancer using optical coherence tomography.,” *Medical image computing and computer-assisted intervention : MICCAI ... International Conference on Medical Image Computing and Computer-Assisted Intervention*, vol. 12, no. Pt 2, pp. 657-64, Jan. 2009.

[43] A. M. Zysk and S. A. Boppart, “Computational methods for analysis of human breast tumor tissue in optical coherence tomography images.,” *Journal of biomedical optics*, vol. 11, no. 5, p. 054015.

[44] A. L. Clark, A. Gillenwater, R. Alizadeh-Naderi, A. K. El-Naggar, and R. Richards-Kortum, “Detection and diagnosis of oral neoplasia with an optical coherence microscope,” *Journal of Biomedical Optics*, vol. 9, no. 6, pp. 1271-1280, Nov. 2004.

[45] X. Liang, S. G. Adie, R. John, and S. A. Boppart, “Dynamic spectral-domain optical coherence elastography for tissue characterization,” *Optics Express*, vol. 18, no. 13, pp. 14183-14190, 2010.

[46] B. F. Kennedy*, T. R. Hillman, R. A. McLaughlin, B. C. Quirk, and D. D. Sampson, “In vivo dynamic optical coherence elastography using a ring actuator,” *Optics Express*, vol. 17, no. 24, p. 21762, Nov. 2009.

[47] X. Liang, A. L. Oldenburg, V. Crecea, E. J. Chaney, and S. A. Boppart, “Optical micro-scale mapping of dynamic biomechanical tissue properties,” *Optics Express*, vol. 16, no. 15, p. 11052, Jul. 2008.

[48] X. Liang, S. G. Adie, R. John, and S. A. Boppart, “Dynamic spectral-domain optical coherence elastography for tissue characterization,” *Optics Express*, vol. 18, no. 13, p. 14183, Jun. 2010.

[49] C. Sun, B. Standish, and V. X. D. Yang, “Optical coherence elastography: current status and future applications.,” *Journal of biomedical optics*, vol. 16, no. 4, p. 043001, Apr. 2011.

[50] S. Suresh, “Biomechanics and biophysics of cancer cells☆,” *Acta Materialia*, vol. 55, no. 12, pp. 3989-4014, Jul. 2007.

[51] J. Guck et al., “Optical deformability as an inherent cell marker for testing malignant transformation and metastatic competence.,” *Biophysical journal*, vol. 88, no. 5, pp. 3689-98, May 2005.

[52] C. Vinegoni, C. Pitsouli, D. Razansky, N. Perrimon, and V. Ntziachristos, “In vivo imaging of Drosophila melanogaster pupae with mesoscopic fluorescence tomography.,” *Nature methods*, vol. 5, no. 1, pp. 45-7, Jan. 2008.

[53] B. Null, C. W. Liu, M. Hedehus, S. Conolly, and R. W. Davis, “High-resolution, in vivo magnetic resonance imaging of Drosophila at 18.8 Tesla.,” *PloS one*, vol. 3, no. 7, p. e2817, Jan. 2008.

[54] C. Vinegoni, D. Razansky, C. Pitsouli, N. Perrimon, V. Ntziachristos, and R. Weissleder, “Mesoscopic fluorescence tomography for in-vivo imaging of developing Drosophila.,” *Journal of visualized experiments : JoVE*, no. 30, Jan. 2009.

[55] L. Thrane, “Optical Coherence Tomography : Modeling and Applications,” 2001.